

2



US Army Corps  
of Engineers

Construction Engineering  
Research Laboratory

USACERL Technical Manuscript M-89/11  
September 1989

AD-A213 062

# Electromagnetic Wave Propagation Through Circular Waveguides Containing Radially Inhomogeneous Lossy Media

by  
Keith W. Whites

Propagation characteristics of an electromagnetic (EM) wave inside a waveguide are greatly modified by the introduction of dielectrics into the guide. Frequency of cutoff, attenuation, and power flow distribution are all properties of the EM wave that are highly dependent on the physical structure and composition within the guide. Shielding applications take advantage of the large amount of attenuation provided by a waveguide when the incident EM wave has a frequency lower than the cutoff frequency of the waveguide. In practice, small sections of waveguides are inserted through the metal walls of a shielded enclosure to construct an air passage that does not compromise the shielding effectiveness of the shelter. Typically, however, other fluids and materials besides air must be transferred inside the enclosure. Therefore, hoses are sometimes inserted through these waveguides, which can reduce the shielding provided by the waveguide above and below cutoff.

This work has investigated the EM propagation through these loaded waveguides structures, placing special emphasis on wave attenuation. The study was divided into two problems: the modal coupling and excitation of a finite inhomogeneous guide.

Solutions to the radially inhomogeneous infinite circular waveguides have been obtained numerically from an exact theoretical development beginning with first principles. These inhomogeneous waveguides are layered with circular, concentric annuli, possibly having complex constitutive parameters. The modes that were found to exist in these waveguides are hybrid, meaning that they have both axial E- and H-fields. The foundations and numerical solutions developed were verified experimentally.

13 SEP 1989  
D

Approved for public release; distribution is unlimited.

89 9 28 083

The contents of this report are not to be used for advertising, publication, or promotional purposes. Citation of trade names does not constitute an official indorsement or approval of the use of such commercial products. The findings of this report are not to be construed as an official Department of the Army position, unless so designated by other authorized documents.

*DESTROY THIS REPORT WHEN IT IS NO LONGER NEEDED  
DO NOT RETURN IT TO THE ORIGINATOR*

UNCLASSIFIED

SECURITY CLASSIFICATION OF THIS PAGE

REPORT DOCUMENTATION PAGE				Form Approved OMB No 0704 0188 Exp Date Jun 30 1986	
1a REPORT SECURITY CLASSIFICATION UNCLASSIFIED			1b RESTRICTIVE MARKINGS		
2a SECURITY CLASSIFICATION AUTHORITY			3 DISTRIBUTION AVAILABILITY OF REPORT Approved for public release; distribution is unlimited.		
2b DECLASSIFICATION/DOWNGRADING SCHEDULE					
4 PERFORMING ORGANIZATION REPORT NUMBER(S) USACERL TM M-89/11			5 MONITORING ORGANIZATION REPORT NUMBER(S)		
6a NAME OF PERFORMING ORGANIZATION U.S. Army Construction Engr Research Laboratory		6b OFFICE SYMBOL (If applicable) CECER-EM	7a NAME OF MONITORING ORGANIZATION		
6c ADDRESS (City, State, and ZIP Code) P.O. Box 4005 Champaign, IL 61824-4005			7b ADDRESS (City, State, and ZIP Code)		
8a NAME OF FUNDING SPONSORING ORGANIZATION HQUSACE		8b OFFICE SYMBOL (If applicable) CEEC-EE	9 PROCUREMENT INSTRUMENT IDENTIFICATION NUMBER		
8c ADDRESS (City, State, and ZIP Code) 20 Massachusetts Ave, NW WASH DC 20314-1000			10 SOURCE OF FUNDING NUMBERS		
			PROGRAM ELEMENT NO 4A16234	PROJECT NO AT41	TASK NO MA
					WORK UNIT ACCESSION NO C59
11 TITLE (Include Security Classification) Electromagnetic Wave Propagation Through Circular Waveguides Containing Radially Inhomogeneous Lossy Media					
12 PERSONAL AUTHOR(S) Keith Wayne Whites					
13a TYPE OF REPORT Final		13b TIME COVERED FROM _____ TO _____		14 DATE OF REPORT (Year, Month, Day) 1989, August	
15 PAGE COUNT 168					
16 SUPPLEMENTARY NOTATION Copies are available from the National Technical Information Service Springfield, VA 22161					
17 COSATI CODES			18 SUBJECT TERMS (Continue on reverse if necessary and identify by block number)		
FIELD	GROUP	SUB-GROUP			
20	14		electromagnetic wave propagation waveguides inhomogeneous lossy media		
19 ABSTRACT (Continue on reverse if necessary and identify by block number)					
<p>Propagation characteristics of an electromagnetic (EM) wave inside a waveguide are greatly modified by the introduction of dielectrics into the guide. Frequency of cutoff, attenuation, and power flow distribution are all properties of the EM wave that are highly dependent on the physical structure and composition within the guide. Shielding applications take advantage of the large amount of attenuation provided by a waveguide when the incident EM wave has a frequency lower than the cutoff frequency of the waveguide. In practice, small sections of waveguides are inserted through the metal walls of a shielded enclosure to construct an air passage that does not compromise the shielding effectiveness of the shelter. Typically, however, other fluids and materials besides air must be transferred inside the enclosure. Therefore, hoses are sometimes inserted through these waveguides, which can reduce the shielding provided by the waveguide above and below cutoff.</p> <p style="text-align: right;">(Cont'd)</p>					
20 DISTRIBUTION AVAILABILITY OF ABSTRACT <input type="checkbox"/> UNANNOUNCED <input checked="" type="checkbox"/> AVAILABLE AS RPT <input type="checkbox"/> DTIC USERS			21 ABSTRACTS AND INDEXES Unclassified		
22a NAME OF RESPONSIBLE INDIVIDUAL Diane P. Mann			22b TELEPHONE (Include Area Code) (217) 373-7223		22c OFFICE SYMBOL CECER-IMO

## FOREWORD

This work was performed for the Directorate of Engineering and Construction, Headquarters, U.S. Army Corps of Engineers (HQUSACE), under Project 4A16234AT41, "Military Facilities Engineering Technology"; Work Unit MA-C59, "Electromagnetic Pulse (EMP) Validation and Design Recommendations for Command, Control, Communications and Intelligence Facilities." The HQUSACE Technical Monitor was Mr. L. Horvath, CEEC-EE.

This project was conducted by the Engineering and Materials Division, U.S. Army Construction Engineering Research Laboratory (USACERL-EM) in the EMP team. Mr. Ray McCormack is the EMP team leader and the Principal Investigator for the Work Unit. The research was done in partial fulfillment of the requirements for the degree of Master of Science in Electrical Engineering at the Graduate College of the University of Illinois at Urbana-Champaign, 1988. The author thanks Professor Raj Mittra of the University of Illinois for guidance and useful suggestions in the research. Support from USACERL in both funding and facilities also is appreciated. Gratitude is expressed to Dr. W. Croisant, Dr. C. Feickert, and Mr. M. McInerney, USACERL, for many stimulating conversations, practical suggestions, and help in preparing the thesis.

Dr. Robert Quattrone is Chief of USACERL-EM. COL Carl O. Magnell is Commander and Director of USACERL, and Dr. L.R. Shaffer is Technical Director.

Approved For	
Project	<input checked="" type="checkbox"/>
Development	<input type="checkbox"/>
Use	<input type="checkbox"/>
Classification	
By _____	
Distribution/_____	
Availability Codes	
Dist	Special
A-1	



# TABLE OF CONTENTS

CHAPTER	PAGE
1. INTRODUCTION .....	1
2. THEORETICAL FORMULATION .....	6
2.1 Scalar-Wave Function Method .....	7
2.2 Multiple Concentric Dielectrics .....	11
2.3 Two-Dielectric Matrix Construction .....	17
2.4 Hybrid Modes .....	18
2.5 Modal Nomenclature and Designation .....	23
2.6 Nonzero Wall Losses .....	24
3. NUMERICAL IMPLEMENTATION .....	29
3.1 Root Finding by Muller's Method .....	30
3.2 MDCW Computer Program .....	32
3.3 Results for Two Dielectrics .....	34
3.4 Other Axial Wavenumber Plots .....	38
3.5 Power Flow .....	39
4. INHOMOGENEOUS THREE-LAYERED DIELECTRICALLY-LOADED WAVEGUIDES .....	65
4.1 Lossless Three-Dielectric Waveguides .....	66
4.2 Complex and Backward-Wave Modes .....	69
4.3 Attenuation in Lossy Three-Dielectric Waveguides .....	75
4.4 Power Flow in Lossy Three-Dielectric Waveguides .....	78
5. EXPERIMENTAL INVESTIGATIONS .....	111
5.1 Resonant Cavity Method Justification .....	112
5.2 Resonant Cavity Measurements .....	113
5.3 Theoretically Predicted Resonances .....	116
5.4 Finite Open-Ended Waveguide Measurements .....	117

6. CONCLUSIONS AND SUGGESTIONS FOR FURTHER STUDY .....	135
APPENDIX. MDCW COMPUTER PROGRAM LISTING .....	139
REFERENCES .....	156

## CHAPTER 1

### INTRODUCTION

The propagation characteristics of an electromagnetic (EM) wave inside a waveguide are greatly modified by the introduction of dielectrics into the guide. The frequency of cutoff (where the wave begins propagation), the attenuation and the distribution of power flow are all properties of the EM wave that are highly dependent on the physical structure and composition within the guide. Shielding applications take advantage of the large amount of attenuation provided by a waveguide when the incident EM wave has a frequency lower than the cutoff frequency of the waveguide. In practice, small sections of waveguides are inserted through the metal walls of a shielded enclosure to construct an air passage which does not compromise the shielding effectiveness of the shelter. Typically, however, other fluids and materials besides air must be transferred inside the enclosure. To accomplish this, hoses are occasionally inserted through these waveguides; hence, the shielding provided by the waveguide above and below cutoff can be reduced. It is the aim of this work to investigate the EM propagation through these loaded waveguide structures placing special emphasis on the attenuation of the wave.

This loaded waveguide problem may be separated into two main subproblems, (i) the modal coupling and excitation of a *finite* inhomogeneous guide, and (ii) the modal solutions and wave properties for an *infinite* inhomogeneous guide. These two parts are related by the fact that once the excited modes are identified in the finite guide, the attenuation and other attributes of the wave can be calculated using the infinite guide solutions. Identifying the excited modes is a difficult task theoretically and is not considered in this work. Experimentally, however, a large number of measurements were performed on such an arrangement. Instead, this work emphasizes the wave properties not directly dependent on the source excitation, but concentrates more on the inhomogeneous

waveguide penetration itself and the characteristic properties of the geometry and loading materials.

As a first approximation to the theoretical analysis of this problem, the waveguide structure is modelled as an infinite waveguide containing layered concentric dielectrics forming homogeneous annuli. In this vein, there has been much work done for the two concentric dielectric problem in which a dielectric rod is inserted inside the guide. Pincherle [1] was one of the first to consider this two-dielectric guide and found solutions for both the rectangular and circular guides. For the latter, only azimuthally symmetric modes were considered. The two papers by Clarricoats [2] provide a more complete, authoritative exposition on the two-dielectric guide and they also build the stage from which many papers over the next decade (1960's) on the topic of the rod-insert waveguide were set. Recently, a number of papers concerning the two-dielectric insert waveguide and resonators have appeared by Zaki and Atia [3] and Zaki and Chen [4], [5]. In these papers, more emphasis is placed on the nonazimuthally symmetric modes and their corresponding field patterns and resonant frequencies for rod-loaded cavities of similar cross sections. Until recently, very little if anything has been published for the cases in which more than two dielectrics fill the waveguide. Bruno and Bridges [6] consider a variant of the three-dielectric problem— that of a two-dielectric lossless rod guide. Chou and Lee [7] analyze the case of a perfect electrically conducting (pec) waveguide with multiple coatings having perhaps complex permeabilities. This is related to the problem at hand, but here, however, lossy dielectric fillings rather than lossy magnetic coatings are relevant. In this work, the theoretical formulation and subsequent numerical solutions for the waveguide filled with any number of concentric, perhaps lossy, dielectrics will be presented. Both electric and magnetic losses are allowed or any combination of  $\mu_r$ 's and  $\epsilon_r$ 's; however, only electrical losses will be considered here.

Solutions to this loaded waveguide problem hinge on finding roots of a characteristic equation which is derived from first principles. The roots of this equation are



the axial wavenumbers,  $k_z$ , for a given azimuthal variation. There are an infinite number of these roots for each azimuthal variation and developing a method by which a root can be assigned to a mode is a large part of the total solution process. One method of identifying roots in the inhomogeneous case, and one which is used extensively in this work, is to "trace" the root in the complex plane as some parameter is continuously varied. The starting point for this tracing process is chosen where the mode type and root are known, usually the homogeneous guide case, and then the  $k_z$  value is continuously computed while some physical parameter is incremented, such as the radius of the dielectrics, the constitutive parameters of the dielectrics, the frequency, or perhaps the amount of loss. This tracing process becomes especially important, and also difficult, when there is much loss, since the roots are then located somewhere in the total complex plane. In this work, many examples will be given when very high dielectric losses are present, from which the attenuation and axial power flow, among other things, will be examined. In particular, as discussed at the beginning of this chapter, the three-layered, dielectrically-loaded waveguide is very important in this study. An in-depth investigation into the attenuation for this inhomogeneous guide will be performed in Chapter 4.

During this  $k_z$  tracing process, for reasons to be discussed throughout this thesis beginning in Section 3.3, backward-wave regions may develop for these dielectrically-loaded waveguides. A backward-wave region is one in which the wavefronts are traveling in the opposite direction to the net power flow. ("Net" power flow is a necessary statement since it will also be shown that the power flow can have differing signs in different dielectric annuli.) Clarricoats and Waldron [8] were the first to predict the existence of such a phenomenon in the two-dielectric circular guide. This topic was extensively studied after that with Clarricoats publishing two excellent papers on the topic [9], [10]. Experimental verification for the existence of these backward waves, in addition to the theoretical development, was carried out by Clarricoats and Birtles [11] with a resonant cavity technique and by Clarricoats and Slinn [12] using a slot in a loaded waveguide.

Both techniques showed very good agreement with the theoretically expected values. An extensive list of applications for the rod-loaded waveguide backward-wave structure was discussed by Waldron [13]. In this thesis, the existence of these backward waves will be verified for the two-dielectric case and also intensively studied in the three-dielectric guide.

A new modal designation scheme for backward-wave modes will be introduced, beginning in Section 3.5, that is more consistent with other properties of the wave, in addition to the  $k_z$ , such as net power flow, boundedness of the wave and continuity in the  $k_z$  trace. This new scheme relies on the introduction of a small amount of loss into the dielectrics in order that the proper  $k_z$  root can be chosen. Until the recent advent of sophisticated Bessel function computer subroutines which can compute values for complex arguments, this could not be done very easily. Along with this new modal designation scheme comes a slightly revised look at the cutoff frequency for a mode. The issue at hand concerning this topic is whether  $k_z$  equals zero for cutoff, the phase and group velocities are infinite and zero, respectively at cutoff, none of these, or maybe some combination. The results of this study suggest that the frequency for which the group velocity is zero is a more fundamental concept for cutoff than  $k_z=0$  and, correspondingly, the phase velocity becoming infinite.

In addition to backward waves forming during the  $k_z$  tracing process, regions having complex  $k_z$  in the form of  $\beta - j\alpha$  can also exist, even in lossless media! Normally, this would not be expected since wave attenuation in lossless media with finite power flow would seem to violate conservation of energy principles. Clarricoats and Taylor [14] predicted the existence of these complex modes in the two-dielectric waveguide. It is pointed out there, and by Chorney [15], that these complex modes always exist in pairs having complex conjugate axial wavenumbers so that zero net power flow is preserved across any transverse plane of the waveguide. Therefore, conservation of energy is enforced since no net axial power flow is present. This does not imply, however, that locally there is no axial power flow. It will be seen later in this thesis that the axial power

flow is mostly nonzero in the cross section of the guide and only the *net* power flow goes to zero. Chorney also states that not only is the real power flow zero, but the complex modes also carry no net reactive power. Laxpati and Mittra [16] also note the zero axial power flow condition for the complex modes in lossless media and further claim this to be a condition for these modes to physically exist in the waveguide and not merely as "spurious," nonphysical modes. Recently, Kalmyk, Rayevskiy and Ygryumov [17] have presented experimental evidence showing the existence of these complex modes in a circular waveguide.

Although no net power flow is carried by the complex modes in lossless media, once losses are introduced into the dielectrics, the relative phase difference between the two coupled, complex modes will make net power flow possible. From a shielding application standpoint, the amount of attenuation in these complex modes becomes an important issue.

The final topic considered in this thesis is the experimental measurements for the inhomogeneous circular waveguide. There were two types of measurement arrangements used here which applied either to loading dielectrics which were nearly lossless or to those with significant loss. For nearly lossless dielectrics, a resonant cavity of like transverse geometry as the three-dielectric waveguide was used to investigate the physical phenomenon and verify the numerical computations. For dielectrics with significant losses, a finite waveguide arrangement through a shielded enclosure was employed. The results of both measurement techniques compared very well with the theoretical predictions even though a number of rough approximations had to be made to recover from a lack of proper equipment. The agreement between the calculated values (the resonant frequencies of the cavity and the attenuation in the finite-guide arrangement) and the laboratory measurements gives credence to the theoretical and numerical work in this thesis. Coupling this with additional verification provided by other published work for the two-dielectric waveguide attests to the accuracy of the theoretical development, presented next, and the subsequent numerical solutions to this inhomogeneous waveguide arrangement.

## CHAPTER 2

### THEORETICAL FORMULATION

The primary concern of this chapter is the theoretical development of the infinite inhomogeneous waveguide. The particular class of inhomogeneity considered here is a radial variation in the constitutive parameters forming homogeneous, lossy annuli with invariance in the  $\phi$  direction. The resulting set of equations is too complicated to solve analytically since the expansion functions for the radial variation are Bessel functions; therefore, numerical techniques are employed. The principal objective of this numerical analysis is to find the axial wavenumber,  $k_z$ . Once this has been determined, all other quantities such as the field components, attenuation, and power flow can be calculated. This determination of  $k_z$  is based on an eigensolution concept which will indicate situations that *can* exist and not necessarily those that *do* exist in a physical arrangement. Further analysis of the source coupling would be needed for this. However, since a sum of solutions is also a solution in a linear treatment, this eigensolution method is very useful in explaining results from measurements by using either one solution or perhaps adding a number of solutions.

The existence of hybrid modes in this type of inhomogeneous guide is one big factor distinguishing it from the homogeneous case. A hybrid mode is one that has both nonzero axial electric and magnetic components. This is in contrast to the homogeneous case for which modes of vanishing axial electric or magnetic fields can be constructed. The method of mode nomenclature for these hybrid modes is still a fuzzy issue. Many authors have put forth their suggestions but no method has won sweeping acceptance. The method chosen here is somewhat of a "hybrid" in that Snitzer's method [18], discussed later, is used in conjunction with a mode-tracing concept outlined by Waldron [19]. The latter topic is discussed fully in the next chapter. It is stated without proof by Waldron that all of the modes in any waveguide have a 1:1 correspondence with those of a homogeneous, pec

guide of appropriate cross section. This allows a method of nomenclature based on the homogeneous guide as a limiting case. In any event, each mode can be established by its axial wavenumber. Computation of this wavenumber is possible as a solution to a set of equations constructed from first principles. This formulation, shown next, is an exact one and no approximations are needed.

## 2.1 Scalar-Wave Function Method

The cross section of the infinite waveguide having multiple concentric circular dielectrics is shown in Figure 2.1. (All figures and tables appear at the end of each chapter.) It is assumed that all dielectrics are concentric about the sheath center and that the constitutive parameters for each dielectric are constant. Maxwell's equations for a time-harmonic field in a homogeneous space are given by

$$\begin{aligned}\nabla \times \mathbf{E} &= -j\omega\mu\mathbf{H} & \nabla \cdot \mathbf{D} &= 0 \\ \nabla \times \mathbf{H} &= j\omega\epsilon\mathbf{E} & \nabla \cdot \mathbf{B} &= 0\end{aligned}\tag{2.1}$$

The time dependence  $e^{j\omega t}$  is assumed throughout this work and subsequently suppressed. In (2.1),  $\mu$  is the permeability of the medium and  $\epsilon$  is the permittivity. There are a number of ways in which these equations may be combined and the fields solved to obtain the characteristic response in a bounded environment. One general approach is to stay with the six field components and write solutions in terms of  $E_z$  and  $H_z$  [20]. Another approach is to use the vector potential method and generate solutions to a two-dimensional scalar problem for the transverse geometry assuming invariance in a third Cartesian direction [21]. This second method is chosen here for two major reasons. One, it is elegant in principle since all the field components for a mode can be written in terms of one scalar

function of position. Two, some interesting properties of mode designations can be more clearly delineated when scalar wave functions are used. Whichever method is chosen, identical results will be obtained. The only differences will occur in the intermediate steps.

What follows is a brief review of the vector potential method to solve for the characteristic field response of a circular cylindrical waveguide. This formulation is needed to introduce the methods and nomenclature for extending the normal, homogeneous waveguide methods to the more complicated situation with  $q$  concentric annuli.

Using the vector potential method then, these equations can be combined and the field quantities solved yielding

$$\begin{aligned} \mathbf{E} &= -\nabla \times \mathbf{F} - j\omega\mu\mathbf{A} + \frac{1}{j\omega\epsilon}\nabla(\nabla \cdot \mathbf{A}) \\ \mathbf{H} &= \nabla \times \mathbf{A} - j\omega\epsilon\mathbf{F} + \frac{1}{j\omega\mu}\nabla(\nabla \cdot \mathbf{F}) \end{aligned} \quad (2.2)$$

with  $\mathbf{A}$  and  $\mathbf{F}$  being the vector magnetic and vector electric potentials, respectively. The vector potentials satisfy the vector Helmholtz equation

$$\nabla^2 \mathbf{T} + k^2 \mathbf{T} = 0 \quad (2.3)$$

where  $\mathbf{T} = \mathbf{A}$  or  $\mathbf{F}$  and  $k^2 = \omega^2 \mu \epsilon$ . Two characteristic field responses, namely, Transverse Electric (TE) and Transverse Magnetic (TM) to the  $z$  direction, can be constructed with appropriate choices of these vector potentials. Then from these two mode types, all field patterns in the guide can be expressed as a linear superposition of them. In particular, in the  $i^{\text{th}}$  dielectric let

$$\mathbf{F}_i = 0 \quad \mathbf{A}_i = z\psi_i^m \quad (2.4)$$

where  $\psi_i^m$  is the magnetic scalar wave potential, and (2.2) reduces to

$$\begin{aligned}
 E_{\rho_i} &= \frac{1}{j\omega\epsilon_i} \frac{\partial^2 \psi_i^m}{\partial \rho \partial z} & H_{\rho_i} &= \frac{1}{\rho} \frac{\partial \psi_i^m}{\partial \phi} \\
 E_{\phi_i} &= \frac{1}{j\omega\epsilon_i \rho} \frac{\partial^2 \psi_i^m}{\partial \phi \partial z} & H_{\phi_i} &= \frac{-\partial \psi_i^m}{\partial \rho} \\
 E_{z_i} &= \frac{1}{j\omega\epsilon_i} \left( \frac{\partial^2}{\partial z^2} + k_i^2 \right) \psi_i^m & H_{z_i} &= 0
 \end{aligned} \tag{2.5}$$

with  $k_i$  being the intrinsic wavenumber of the medium. Since  $H_{z_i}=0$ , the field is TM to  $z$ . Likewise, in the  $i^{\text{th}}$  dielectric let

$$F_i = z\psi_i^e \quad A_i = 0$$

where  $\psi_i^e$  is the electric scalar wave potential. Then (2.2) reduces to

$$\begin{aligned}
 H_{\rho_i} &= \frac{1}{j\omega\mu_i} \frac{\partial^2 \psi_i^e}{\partial \rho \partial z} & E_{\rho_i} &= \frac{-1}{\rho} \frac{\partial \psi_i^e}{\partial \phi} \\
 H_{\phi_i} &= \frac{1}{j\omega\mu_i \rho} \frac{\partial^2 \psi_i^e}{\partial \phi \partial z} & E_{\phi_i} &= \frac{\partial \psi_i^e}{\partial \rho} \\
 H_{z_i} &= \frac{1}{j\omega\mu_i} \left( \frac{\partial^2}{\partial z^2} + k_i^2 \right) \psi_i^e & E_{z_i} &= 0
 \end{aligned} \tag{2.6}$$

Since  $E_{z_i}=0$  in this case, the field is TE to  $z$ . The field in any annulus within the guide can be considered as a linear superposition of these two field types.

Also, since the  $\psi_i$ 's are chosen as Cartesian components of the vector potentials, the  $\psi_i$ 's necessarily satisfy the scalar Helmholtz equation

$$\nabla^2 \psi_i + k_i^2 \psi_i = 0 . \quad (2.7)$$

In addition, the geometry inside the guide remains separable with the inclusion of these concentric dielectrics. Therefore, it is quite easy to construct solutions to the scalar Helmholtz equation in each dielectric. Solutions to this homogeneous partial differential equation can be found using the separation of variables method. Accordingly then,

$$\psi_i = P(\rho)\Phi(\phi)Z(z) . \quad (2.8)$$

By substituting this equation into (2.7) and expressing the Laplacian in cylindrical coordinates, (2.7) can be separated into three equations, each a scalar homogeneous ordinary differential equation in one cylindrical coordinate only. For the circular cylindrical geometry here, the general form of  $\psi_i$  will be

$$\psi_i = B_n(k_{\rho}, \rho)h(n\phi)h(k_z z) \quad (2.9)$$

where  $B_n$  is some linear combination of solutions to Bessel's equation,  $h(n\phi)$  is some linear combination of the trigonometric functions  $\sin(n\phi)$  and  $\cos(n\phi)$ , and  $h(k_z z)$  represents the longitudinal variation of the propagating wave. For a wave propagating in this axially invariant environment

$$h(k_z z) = e^{-jk_z z} \quad (2.10)$$



is a correct choice. Here,  $k_z$  represents the longitudinal wavenumber. In a transversely bounded environment, the  $B_n$  function will be a linear combination of two independent solutions to Bessel's equation of the form

$$B_n(k_{\rho_i}\rho) = [a_i J_n(k_{\rho_i}\rho) + b_i N_n(k_{\rho_i}\rho)] \quad (2.11)$$

with  $J_n$  and  $N_n$  the Bessel functions of the first and second kinds, respectively, and  $a_i$  and  $b_i$  being constants. For any source-free region containing the origin,  $b$  will be zero. For a physical system, one would expect the fields to be single valued. This implies that  $n$  should be chosen as an integer. Finally, for the  $\psi_i$  to be a valid solution to (2.7) the separation relation

$$k_i^2 = \omega^2 \mu_i \epsilon_i = k_{\rho_i}^2 + k_z^2 \quad (2.12)$$

must be satisfied. By phase matching considerations of the tangential fields,  $k_z$  will be the same throughout the cross section of the guide.

## 2.2 Multiple Concentric Dielectrics

To formulate the problem of  $q$  concentric dielectrics, the  $\psi_i$ 's are constructed in view of (2.9) and the ensuing discussion. In each dielectric then,

$$\psi_1^m = C_{11} J_n(k_{\rho_1}\rho) \cos(n\phi) e^{-jk_z z}$$

$$\psi_1^e = C_{13} J_n(k_{\rho_1}\rho) \sin(n\phi) e^{-jk_z z}$$

$$\begin{aligned}
\psi_2^m &= [C_{21}J_n(k_{p_2}\rho) + C_{22}N_n(k_{p_2}\rho)]\cos(n\phi)e^{-jk_z z} \\
\psi_2^e &= [C_{23}J_n(k_{p_2}\rho) + C_{24}N_n(k_{p_2}\rho)]\sin(n\phi)e^{-jk_z z} \\
&\vdots \\
\psi_t^m &= [C_{t1}J_n(k_{p_t}\rho) + C_{t2}N_n(k_{p_t}\rho)]\cos(n\phi)e^{-jk_z z} \\
\psi_t^e &= [C_{t3}J_n(k_{p_t}\rho) + C_{t4}N_n(k_{p_t}\rho)]\sin(n\phi)e^{-jk_z z} \\
&\vdots \\
\psi_q^m &= [C_{q1}J_n(k_{p_q}\rho) + C_{q2}N_n(k_{p_q}\rho)]\cos(n\phi)e^{-jk_z z} \\
\psi_q^e &= [C_{q3}J_n(k_{p_q}\rho) + C_{q4}N_n(k_{p_q}\rho)]\sin(n\phi)e^{-jk_z z} .
\end{aligned} \tag{2.13}$$

The coefficients  $C_{rs}$  are unknowns at this stage and will be solved for in the next chapter. The index  $r$  refers to the layer and  $s$  to the coefficient of the specific radial variation in the expansion (an integer from 1 to 4).  $C_{12}$  and  $C_{14}$  are both chosen equal to zero since the Neumann function,  $N_n$ , is infinite at the origin and there is no reason to expect singularities in the field there. By the azimuthal symmetry of this waveguide arrangement, there is a degeneracy in the  $\phi$  variation except for the modes having  $n=0$  [7]. For simplicity, only one of these is shown here.

The boundary conditions for this problem (that the tangential fields are continuous across each dielectric boundary) must be applied in order to evaluate the coefficients. At each dielectric interface there will be four equations of continuity—one equation for each of  $E_\phi$ ,  $E_z$ ,  $H_\phi$  and  $H_z$ . This gives a total of  $(4q-4)$  equations. The total number of unknowns is  $(4q-2)$  due to the fact that  $C_{12}$  and  $C_{14}$  have been evaluated on physical grounds. Two more equations are needed. These, of course, are provided by the guiding structure which determines the major propagating characteristics of the system. Assuming in this case a pec, then  $E_\phi=0$  and  $E_z=0$  at  $\rho=b$ . Therefore, the total number of equations and unknowns is equal at  $(4q-2)$ .

As mentioned previously, the total field in each annulus will be a linear superposition of TE and TM fields to  $z$ . To apply the boundary conditions then, the fields must be computed according to Equations (2.5) and (2.6). Proceeding, let

$$\psi_i^m = \hat{\psi}_i^m h^m(n\phi) = \{[C_{i1}J_n(k_{\rho_i}\rho) + C_{i2}N_n(k_{\rho_i}\rho)]e^{-jk_z z}\}\cos(n\phi)$$

and

$$\psi_i^e = \hat{\psi}_i^e h^e(n\phi) = \{[C_{i3}J_n(k_{\rho_i}\rho) + C_{i4}N_n(k_{\rho_i}\rho)]e^{-jk_z z}\}\sin(n\phi) .$$

(2.14)

Using this notation,

$$E_z = \frac{k_{\rho_i}^2}{j\omega\epsilon_i} \psi_i^m \quad (2.15)$$

$$H_z = \frac{k_{\rho_i}^2}{j\omega\mu_i} \psi_i^e \quad (2.16)$$

and

$$E_{\phi_i} = \frac{-jk_z}{j\omega\epsilon_i\rho} \frac{\partial\psi_i^m}{\partial\phi} + \frac{\partial\psi_i^e}{\partial\rho} \quad (2.17)$$

$$E_{\phi_i} = \frac{nk_z}{\omega\epsilon_i\rho} \hat{\psi}_i^m h^e(n\phi) + k_{\rho_i} \hat{\psi}_i^e h^e(n\phi) .$$

Also,

$$H_{\phi_i} = \frac{-jk_z}{j\omega\mu_i\rho} \frac{\partial\psi_i^e}{\partial\phi} - \frac{\partial\psi_i^m}{\partial\rho} \quad (2.18)$$

$$H_{\phi_i} = \frac{-nk_z}{\omega\mu_i\rho} \hat{\psi}_i^e h^m(n\phi) - k_{\rho_i} \hat{\psi}_i^m h^m(n\phi) .$$

The above primed quantities denote differentiation with respect to  $\rho$  as

$$\begin{aligned}\hat{\psi}_i^m &= [C_{i1}J_n'(k_{\rho_i}\rho) + C_{i2}N_n'(k_{\rho_i}\rho)]e^{-jk_z z} \\ \hat{\psi}_i^e &= [C_{i3}J_n'(k_{\rho_i}\rho) + C_{i4}N_n'(k_{\rho_i}\rho)]e^{-jk_z z}.\end{aligned}\quad (2.19)$$

Equating tangential components of  $E$  and  $H$  at  $\rho=a$  gives

(i) for  $E_z$  —

$$E_{z(t-1)} = E_{z_t} \quad \text{at } \rho = a$$

then,

$$\frac{k_{\rho(t-1)}^2}{j\omega\epsilon_{(t-1)}}\hat{\psi}_{(t-1)}^m = \frac{k_{\rho_t}^2}{j\omega\epsilon_t}\hat{\psi}_t^m$$

or,

$$\begin{aligned}k_{\rho(t-1)}^2\epsilon_t[C_{(t-1)1}J_n(k_{\rho(t-1)}a) + C_{(t-1)2}N_n(k_{\rho(t-1)}a)] \\ - k_{\rho_t}^2\epsilon_{(t-1)}[C_{t1}J_n(k_{\rho_t}a) + C_{t2}N_n(k_{\rho_t}a)] = 0\end{aligned}\quad (2.20)$$

(ii) for  $H_z$  —

$$H_{z(t-1)} = H_{z_t} \quad \text{at } \rho = a$$

then,

$$\frac{k_{\rho(t-1)}^2}{j\omega\mu_{(t-1)}}\hat{\psi}_{(t-1)}^e = \frac{k_{\rho_t}^2}{j\omega\mu_t}\hat{\psi}_t^e$$

or,

$$\begin{aligned}k_{\rho(t-1)}^2\mu_t[C_{(t-1)3}J_n(k_{\rho(t-1)}a) + C_{(t-1)4}N_n(k_{\rho(t-1)}a)] \\ - k_{\rho_t}^2\mu_{(t-1)}[C_{t3}J_n(k_{\rho_t}a) + C_{t4}N_n(k_{\rho_t}a)] = 0\end{aligned}\quad (2.21)$$

(iii) for  $E_\phi$  —

$$E_{\phi_{(t-1)}} = E_{\phi_t} \quad \text{at } \rho = a$$

then,

$$\begin{aligned} & \frac{nk_z}{\omega\epsilon_{(t-1)}a} \psi_{(t-1)}^m h^e(n\phi) + k_{\rho_{(t-1)}} \psi_{(t-1)}^{e'} h^e(n\phi) \\ & - \left[ \frac{nk_z}{\omega\epsilon_t a} \psi_t^m h^e(n\phi) + k_{\rho_t} \psi_t^{e'} h^e(n\phi) \right] = 0 \end{aligned}$$

or,

$$\begin{aligned} & \frac{nk_z}{\omega\epsilon_{(t-1)}a} [C_{(t-1)1} J_n(k_{\rho_{(t-1)}} a) + C_{(t-1)2} N_n(k_{\rho_{(t-1)}} a)] \\ & + k_{\rho_{(t-1)}} [C_{(t-1)3} J_n'(k_{\rho_{(t-1)}} a) + C_{(t-1)4} N_n'(k_{\rho_{(t-1)}} a)] \\ & - \frac{nk_z}{\omega\epsilon_t a} [C_{t1} J_n(k_{\rho_t} a) + C_{t2} N_n(k_{\rho_t} a)] \\ & - k_{\rho_t} [C_{t3} J_n'(k_{\rho_t} a) + C_{t4} N_n'(k_{\rho_t} a)] = 0 \end{aligned} \quad (2.22)$$

(iv) for  $H_\phi$  —

$$H_{\phi_{(t-1)}} = H_{\phi_t} \quad \text{at } \rho = a$$

then,

$$\begin{aligned} & \frac{nk_z}{\omega\mu_{(t-1)}a} \psi_{(t-1)}^e h^m(n\phi) + k_{\rho_{(t-1)}} \psi_{(t-1)}^{m'} h^m(n\phi) \\ & - \left[ \frac{nk_z}{\omega\mu_t a} \psi_t^e h^m(n\phi) + k_{\rho_t} \psi_t^{m'} h^m(n\phi) \right] = 0 \end{aligned}$$

or,

$$\begin{aligned} & k_{\rho_{(t-1)}} [C_{(t-1)1} J_n'(k_{\rho_{(t-1)}} a) + C_{(t-1)2} N_n'(k_{\rho_{(t-1)}} a)] \\ & + \frac{nk_z}{\omega\mu_{(t-1)}a} [C_{(t-1)3} J_n(k_{\rho_{(t-1)}} a) + C_{(t-1)4} N_n(k_{\rho_{(t-1)}} a)] \end{aligned} \quad (2.23)$$

$$\begin{aligned}
& -k_{\rho_i} [C_{i1} J_n'(k_{\rho_i} a) + C_{i2} N_n'(k_{\rho_i} a)] \\
& - \frac{nk_z}{\omega \mu_i a} [C_{i3} J_n(k_{\rho_i} a) + C_{i4} N_n(k_{\rho_i} a)] = 0 .
\end{aligned}$$

The remaining boundary condition to apply is that for the guiding structure itself. For a pec, the tangential electric fields  $E_\phi$  and  $E_z$  must equal zero at  $\rho=b$ . This implies from considering Equations (2.13), (2.15) and (2.17)

$$C_{q1} J_n(k_{\rho_q} b) + C_{q2} N_n(k_{\rho_q} b) = 0$$

and

(2.24)

$$C_{q3} J_n'(k_{\rho_q} b) + C_{q4} N_n'(k_{\rho_q} b) = 0 .$$

Equations (2.20) through (2.24) form the primary means by which this inhomogeneous waveguide problem will be solved. Collectively, these equations may be considered to form a  $(4q-2)$  matrix on the "variables"  $C_{rs}$ . Since there are no forcing terms, these equations can be written in the matrix form

$$[A][C] = 0 \quad (2.25)$$

where  $[A]$  is a  $(4q-2)$  square matrix and  $[C]$  is a  $(4q-2)$  column matrix. For the nontrivial cases, (2.25) is valid only for

$$\det[A] = 0 . \quad (2.26)$$

The variable that will be solved for in order to enforce (2.26) will, of course, be  $k_z$ . Once  $k_z$  is known, all other variables and fields can be computed as will be shown later.

### 2.3 Two-Dielectric Matrix Construction

It may be instructive at this point to actually construct the matrix  $[A]$  for the case having two dielectrics. This matrix will then be compared to other work as a verification. Let the inner dielectric have constitutive parameters  $\mu_1, \epsilon_1$  with radius  $a$ , and the outer  $\mu_2, \epsilon_2$  with radius  $b$ . The guiding structure will be assumed a pec. The matrix  $[A]$  is then constructed using Equations (2.20) through (2.24) giving

$$[\bar{A}] = \begin{bmatrix} k_{p_1}^2 \epsilon_2 E_1 & 0 & k_{p_2}^2 \epsilon_1 E_2 & k_{p_2}^2 \epsilon_1 E_4 & 0 & 0 \\ 0 & k_{p_1}^2 \mu_2 E_1 & 0 & 0 & k_{p_2}^2 \mu_1 E_2 & k_{p_2}^2 \mu_1 E_4 \\ \frac{nk_z}{\omega \epsilon_1 a} E_1 & k_{p_1} E_1' & \frac{nk_z}{\omega \epsilon_2 a} E_2 & \frac{nk_z}{\omega \epsilon_2 a} E_4 & k_{p_2} E_2' & k_{p_2} E_4' \\ k_{p_1} E_1' & \frac{nk_z}{\omega \mu_1 a} E_1 & k_{p_2} E_2' & k_{p_2} E_4' & \frac{nk_z}{\omega \mu_2 a} E_2 & \frac{nk_z}{\omega \mu_2 a} E_4 \\ 0 & 0 & E_2 & E_4 & 0 & 0 \\ 0 & 0 & 0 & 0 & E_2' & E_4' \end{bmatrix} \quad (2.27)$$

where

$$E_1 = J_n(k_{p_1} a)$$

$$E_3 = N_n(k_{p_1} a)$$

$$E_2 = J_n(k_{p_2} a)$$

$$E_4 = N_n(k_{p_2} a)$$

and

$$[\bar{C}] = \begin{bmatrix} C_{11} \\ C_{13} \\ C_{21} \\ C_{22} \\ C_{23} \\ C_{24} \end{bmatrix}$$

with

$$[\bar{A}][\bar{C}] = 0 .$$

This matrix is in agreement with Harrington [21]. Here, the matrix could be made smaller in size, from  $(4q-2)$  down to  $(4q-4)$  through elimination of the last two rows by combining the third and fourth columns and the fifth and sixth columns. However, to be more general and allow for easier computer programming with the inclusion of other guiding structure boundary conditions, this form is preferred.

## 2.4 Hybrid Modes

Examining matrix  $[\bar{A}]$ , when  $n=0$ , coefficients  $C_{11}$ ,  $C_{21}$  and  $C_{22}$  are not related to coefficients  $C_{13}$ ,  $C_{23}$  and  $C_{24}$  and the field separates into modes TE and TM to  $z$  [21]. From (2.14) then, the  $\psi_i^e$  's are not related, or coupled, to the  $\psi_i^m$  's. This is precisely what is meant by TE or TM "modes." That is, there exists a relationship between five of the field components describing an allowed field pattern with the sixth field component, either  $E_z$  or  $H_z$ , equal to zero. But there is no relationship between the coefficients and hence the fields of the two mode types. In all other cases, where  $n \neq 0$  and  $k_z \neq 0$ , the fields are neither TE nor TM, but are hybrid modes. This means that each mode in the guide will have, in general, both nonzero  $E_z$  and  $H_z$ .

The main emphasis here is that the field pattern in each dielectric is considered to be a superposition of two "basis fields": the TE and TM modes. This is done in each dielectric and the  $\psi_i$  's are constructed as per separation of variables of the scalar Helmholtz equation. The boundary conditions are enforced on the system and the expansion coefficients are solved for. If the expansion coefficients of one mode type are not related to, or not coupled to, the expansion coefficients of the other mode type, then TE and TM fields, or modes, can exist in the guide. Herein lies the main point. This means that the field can have its pattern described by *just* the TE field relationships or *just* the TM field



relationships. However, if the guide is inhomogeneous, the coefficients of the TE and TM modes become interdependent. Then the field must be written as a superposition of TE and TM field patterns and cannot be separated. The expansion coefficients of the two mode types become coupled in this case.

Another way to look at this situation and investigate this coupling of coefficients concept is to go back and consider Maxwell's equations in (2.1). Not every solution to (2.3) (with  $\mathbf{T} = \mathbf{E}$  or  $\mathbf{H}$ ) will satisfy Maxwell's equations. One also needs to enforce the divergence relations in (2.1). Expanding these out in cylindrical coordinates and substituting the linear superposition of (2.5) and (2.6) for the field components in a source-free homogeneous medium give in the  $i^{\text{th}}$  dielectric

$$\nabla \cdot \epsilon_i \mathbf{E}_i = 0 \quad \Rightarrow$$

$$\begin{aligned} \frac{1}{\rho} \frac{\partial}{\partial \rho} \left[ \frac{\rho}{j\omega} \left( \frac{\partial^2 \psi_i^m}{\partial \rho \partial z} \right) - \epsilon_i \frac{\partial \psi_i^e}{\partial \phi} \right] + \frac{1}{\rho} \frac{\partial}{\partial \phi} \left[ \frac{1}{j\omega \rho} \left( \frac{\partial^2 \psi_i^m}{\partial \phi \partial z} \right) + \epsilon_i \frac{\partial \psi_i^e}{\partial \rho} \right] \\ + \frac{\partial}{\partial z} \left( \frac{k_{\rho_i}^2}{j\omega} \psi_i^m \right) = 0 \end{aligned} \quad (2.28)$$

$$\frac{1}{\rho} \frac{\partial}{\partial \rho} \left[ \frac{\rho}{j\omega} \left( \frac{\partial^2 \psi_i^m}{\partial \rho \partial z} \right) \right] + \frac{1}{\rho} \frac{\partial}{\partial \phi} \left[ \frac{1}{j\omega \rho} \left( \frac{\partial^2 \psi_i^m}{\partial \phi \partial z} \right) \right] + \frac{\partial}{\partial z} \left( \frac{k_{\rho_i}^2}{j\omega} \psi_i^m \right) = 0 \quad (2.29)$$

which is only a function of  $\psi_i^m$ . Likewise,

$$\nabla \cdot \mu_i \mathbf{H}_i = 0 \quad \Rightarrow$$

$$\begin{aligned} \frac{1}{\rho} \frac{\partial}{\partial \rho} \left[ \frac{\rho}{j\omega} \left( \frac{\partial^2 \psi_i^e}{\partial \rho \partial z} \right) + \mu_i \frac{\partial \psi_i^m}{\partial \phi} \right] + \frac{1}{\rho} \frac{\partial}{\partial \phi} \left[ \frac{1}{j\omega \rho} \left( \frac{\partial^2 \psi_i^e}{\partial \phi \partial z} \right) - \mu_i \frac{\partial \psi_i^m}{\partial \rho} \right] \\ + \frac{\partial}{\partial z} \left( \frac{k_{\rho_i}^2}{j\omega} \psi_i^e \right) = 0 \end{aligned} \quad (2.30)$$

$$\frac{1}{\rho} \frac{\partial}{\partial \rho} \left[ \frac{\rho}{j\omega} \left( \frac{\partial^2 \psi_i^e}{\partial \rho \partial z} \right) \right] + \frac{1}{\rho} \frac{\partial}{\partial \phi} \left[ \frac{1}{j\omega \rho} \left( \frac{\partial^2 \psi_i^e}{\partial \phi \partial z} \right) \right] + \frac{\partial}{\partial z} \left( \frac{k_{\rho_i}^2}{j\omega} \psi_i^e \right) = 0 \quad (2.31)$$

which is only a function of  $\psi_i^e$ . What has tacitly been assumed here is that

$$\frac{1}{\rho} \frac{\partial}{\partial \rho} \epsilon_i \frac{\partial \psi_i^e}{\partial \phi} = \frac{\epsilon_i}{\rho} \frac{\partial^2 \psi_i^e}{\partial \phi \partial \rho} \quad \text{or} \quad \frac{1}{\rho} \frac{\partial}{\partial \rho} \mu_i \frac{\partial \psi_i^m}{\partial \phi} = \frac{\mu_i}{\rho} \frac{\partial^2 \psi_i^m}{\partial \phi \partial \rho} \quad (2.32)$$

This is true only if these partial derivatives are continuous and the medium homogeneous. All of the functions in (2.32) are discontinuous at  $\rho=0$ . Otherwise, they are continuous in a homogeneous space so that Equations (2.29) and (2.31) are valid, and the coefficient sets  $(C_{i1}, C_{i2})$  can be determined independently of the sets  $(C_{i3}, C_{i4})$ . Hence, TE/TM modes are possible.

However, in an inhomogeneous guide this is no longer the case. Consider from (2.28) and (2.30)

$$\frac{1}{\rho} \frac{\partial}{\partial \rho} \epsilon_i \frac{\partial \psi_i^e}{\partial \phi} \neq \frac{\epsilon_i}{\rho} \frac{\partial^2 \psi_i^e}{\partial \phi \partial \rho} \quad \text{and} \quad \frac{1}{\rho} \frac{\partial}{\partial \rho} \mu_i \frac{\partial \psi_i^m}{\partial \phi} \neq \frac{\mu_i}{\rho} \frac{\partial^2 \psi_i^m}{\partial \phi \partial \rho} \quad (2.33)$$

since in general,  $\epsilon_i=f(\rho)$  and  $\mu_i=g(\rho)$ . (No variation of  $\epsilon_i$  and  $\mu_i$  in  $\phi$  is assumed in this study. If this is not the case, modal separation of fields TE and TM to  $z$  would not be possible and only hybrid modes would exist.) In order for the interchanging of the partials with respect to  $\rho$  and  $\phi$  to be a valid mathematical operation, the mixed partials of  $\psi_i$  must be continuous. In an inhomogeneous guide this will generally not be true. The  $\psi_i$ 's will be discontinuous. Consider Figures 2.2 and 2.3 which are graphs of the  $\psi_i$ 's for a 2.005 in radius pec waveguide having a 0.1908 in thick Teflon tube ( $\epsilon_r=2.1$  F/m) of inner radius 0.5008 in filled with lossy methanol ( $\epsilon_r=23.9 - j15.296$  F/m) at 3 GHz. (The permittivity

values are from von Hippel [22], and the  $\psi_i$ 's and their derivatives will be solved for in Chapters 3 and 4.) In both cases, the  $\psi_i$ 's and their derivatives are discontinuous, within the discretization of the plot, across each material boundary but continuous within each annulus. This is in accordance with the previous discussion. These  $\psi_i$ 's are discontinuous functions in  $\rho$  and interchanging partial derivatives is not a valid mathematical operation. Therefore, the two coefficient sets are related as in (2.28) and (2.30). The manner in which the coefficients of the two mode types are coupled is not as important as the fact that they are just related. From this information alone it is sufficient to deduce that TE and TM fields cannot exist in the guide, but field modes having all six components each must exist, i.e., hybrid modes. Also evident in these graphs is at  $\rho=b$

$$\frac{\partial \psi_3^e}{\partial \rho} = \psi_3^m = 0 .$$

This is consistent with the boundary conditions imposed on the system for  $E_{\phi 3}$  and  $E_{z3}$ . Evidenced in this example is perhaps the biggest difference between the scalar wave potential and field approaches to solving these EM problems. In large, the  $\psi$ 's will be discontinuous functions, whereas the fields will be continuous except for bounded-charge induced discontinuities.

Another interesting case is that of  $k_z=0$ . For all  $n$ , the hybrid mode separation into modes TE and TM also form identically to the cases when  $n=0$ . As an example, the matrix (2.27) constructed for two dielectrics is informative. Here,  $n$  and  $k_z$  occur in pairs. When  $k_z=0$  the same behavior as for  $n=0$  will occur, that is, hybrid modal separation into TE and TM modes. However, this separation is for all modes at cutoff and not just the  $n=0$  modes. This gives rise to another modal designation scheme, namely, as the mode tends to cutoff, the correspondence between the homogeneous cases can be correlated. Although it has been reported that this method of classification agrees with the limiting case as the

guide becomes homogeneous [23], this is not always true. If no backward-wave region (Section 3.3) is present in the dispersion graph, the above statement is correct. As will be seen in Sections (3.5) and (4.2), with a backward-wave region present, a small amount of loss must be introduced into the dielectrics to choose the appropriate eigenvalue and corresponding mode designation. It was found from the results after applying this technique that these two schemes do not always agree if cutoff is defined by the frequency where  $k_z$  is zero. Clarricoats and Taylor [14] note something similar to this but place more restrictions on the rod insert  $\epsilon_r$  value which yields this effect than is really necessary.

For more than two dielectrics, when either  $n$  or  $k_z$  is zero, the modes become TE and TM in the same fashion as with two dielectrics. As each new dielectric is added, the original coefficient sets of the two-dielectric matrix remain uncoupled and four new columns are added in which the new coefficient sets themselves are uncoupled. These columns are added in virtue of Equations (2.20) through (2.23). From (2.20) and (2.21) it is seen that the  $z$  components of the fields do not provide this coupling. It is only the  $\phi$  components which contribute. With an eye on (2.22) and (2.23), when  $n$  or  $k_z = 0$  the  $(C_{t1}, C_{t2})$  become uncoupled from all other coefficients, as do  $(C_{t3}, C_{t4})$ . The  $C_t$  coefficients have the same form as the  $C_{(t-1)}$  's so the two sets of coefficients in the previous four columns remain uncoupled with the addition of four new columns. Similarly, when  $n$  and  $k_z$  are not zero, the addition of four new columns for each new dielectric interface will not have any decoupling effect or leave any other marked impression on the matrix  $[A]$  other than increasing the size. The work on modal designations that has been applied to two dielectrics here and in the literature can be extended to three or more dielectrics without modification.

## 2.5 Modal Nomenclature and Designation

Quite surprisingly, there is no universal scheme of nomenclature for modes in dielectrically-loaded waveguides. There have been many attempts and Bruno and Bridges [6] give an excellent history of the major ones including a new suggestion of their own. Beam had one of the earliest methods, which was based on the relative contributions of  $E_z$  and  $H_z$  to a transverse field component [24]. If  $H_z$  made a larger contribution, the mode was designated HE, and if  $E_z$  larger, EH. The fundamental was assigned  $EH_{11}$ . This scheme was reported to be arbitrary since it depends on which transverse component was observed and how far the mode is from cutoff. Snitzer devised a new scheme by which most modern day methods are based [18]. Although Snitzer's work was with a dielectric-rod waveguide, the extension to the bounded guide is trivial. This method considers the  $HE_{11}$  mode fundamental by both definition and common usage at the time (1961). All modes that have the same sign as the fundamental for the ratio of the coefficients of  $E_{z1}$  and  $H_{z1}$ , namely,  $C_{11}/C_{13}$ , are designated HE. All other modes with different signs are designated EH. Note that the use of HE and EH here is just opposite to that of Beam's. From numerical work in Section 4.2, this scheme works well for modes above cutoff but apparently does not apply to evanescent modes since no consistent relationship among the coefficients could be found.

An efficient and unambiguous method of classification, which can be used in conjunction with Snitzer's scheme, is to start with the homogeneous case, either a TE or TM mode, and gradually increase (or decrease) the radii of the dielectrics within the guide and trace  $k_z$ . Thereby, the modes HE and EH can be associated with TE and TM modes, respectively, of the homogeneous waveguide. This is the Correspondence Idea of Waldron [19] from which a 1:1 correspondence of all modes in the dielectric-filled guide is maintained with those of the homogeneous pec guide as all nonideal characteristics of the

former approach those of the latter. For example, the dielectric annuli radii approach zero, the  $\epsilon_{r_i}$  approach one, or the losses in the dielectrics or waveguide walls approach zero.

## 2.6 Nonzero Wall Losses

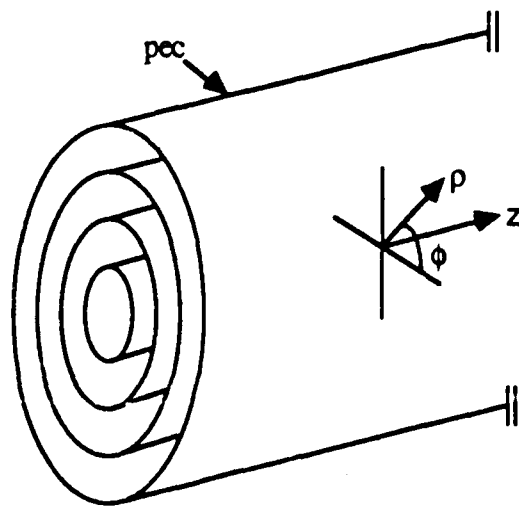
If in a practical situation, the metal losses were significant compared to the dielectric losses, the formulation for this situation can be accurately approximated by considering the metal to be infinite in extent [25]. If the skin depth is small with respect to the guide wall thickness, this is a good approximation. Then instead of  $J_n$  and  $N_n$  functions,  $I_n$  and  $K_n$  can be used where  $I_n$  is the modified Bessel function of the first kind and  $K_n$  is the modified Bessel function of the second kind. Since  $K_n$  exhibits  $e^{-k\rho}$  asymptotic behavior while  $I_n$  has  $e^{k\rho}$  behavior, the coefficients multiplying the  $I_n$  functions must be set equal to zero. That is

$$\begin{aligned}\hat{\psi}_q^m &= [C_{q1}I_n(k_{p_q}\rho) + C_{q2}K_n(k_{p_q}\rho)]e^{-jk_z z} \\ \hat{\psi}_q^e &= [C_{q3}I_n(k_{p_q}\rho) + C_{q4}K_n(k_{p_q}\rho)]e^{-jk_z z}\end{aligned}\tag{2.34}$$

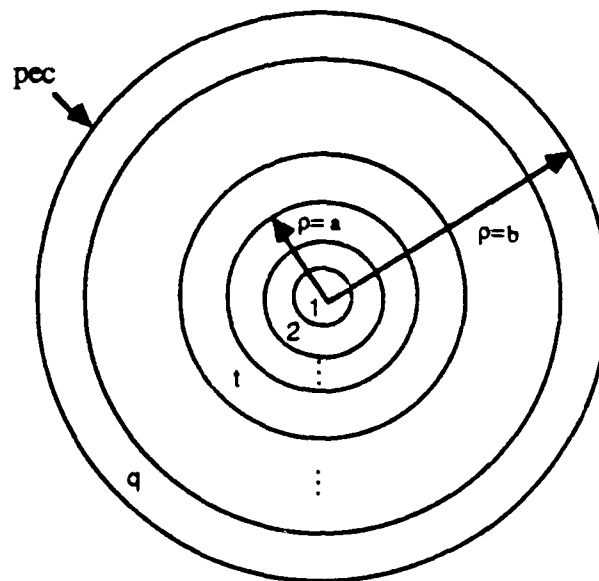
where  $C_{q1}=C_{q3}=0$  and there are  $(q-1)$  dielectrics in the waveguide. No other boundary conditions need be applied to this system and the size of the  $[A]$  matrix is reduced to  $(4q-4)$ . This example shows that the analysis used in this chapter is general enough that it is relatively easy to modify the equations and corresponding matrices to account for other waveguiding boundaries, not just pec waveguide structures.

To actually find solutions to these radially inhomogeneous waveguide problems, the characteristic equation (2.26) is solved yielding the eigenvalues  $k_z$ . This matrix  $[A]$ , as noted earlier, is composed of higher transcendental functions and in general cannot be solved analytically. Instead, numerical techniques are employed, which is the subject of

the next chapter. It should be noted in passing that certain special cases may be solved analytically (for example,  $n = 0$  or  $1$  and two dielectrics) and using tables of Bessel functions to obtain numerical results. However, if lossy materials are considered or higher modes are needed, solutions are not possible using only analytical techniques and tables of Bessel functions, even for these special cases.



(a) Oblique view



(b) End view

Figure 2.1. Geometry and physical arrangement of the infinite inhomogeneous circular waveguide with concentric layered homogeneous annuli.



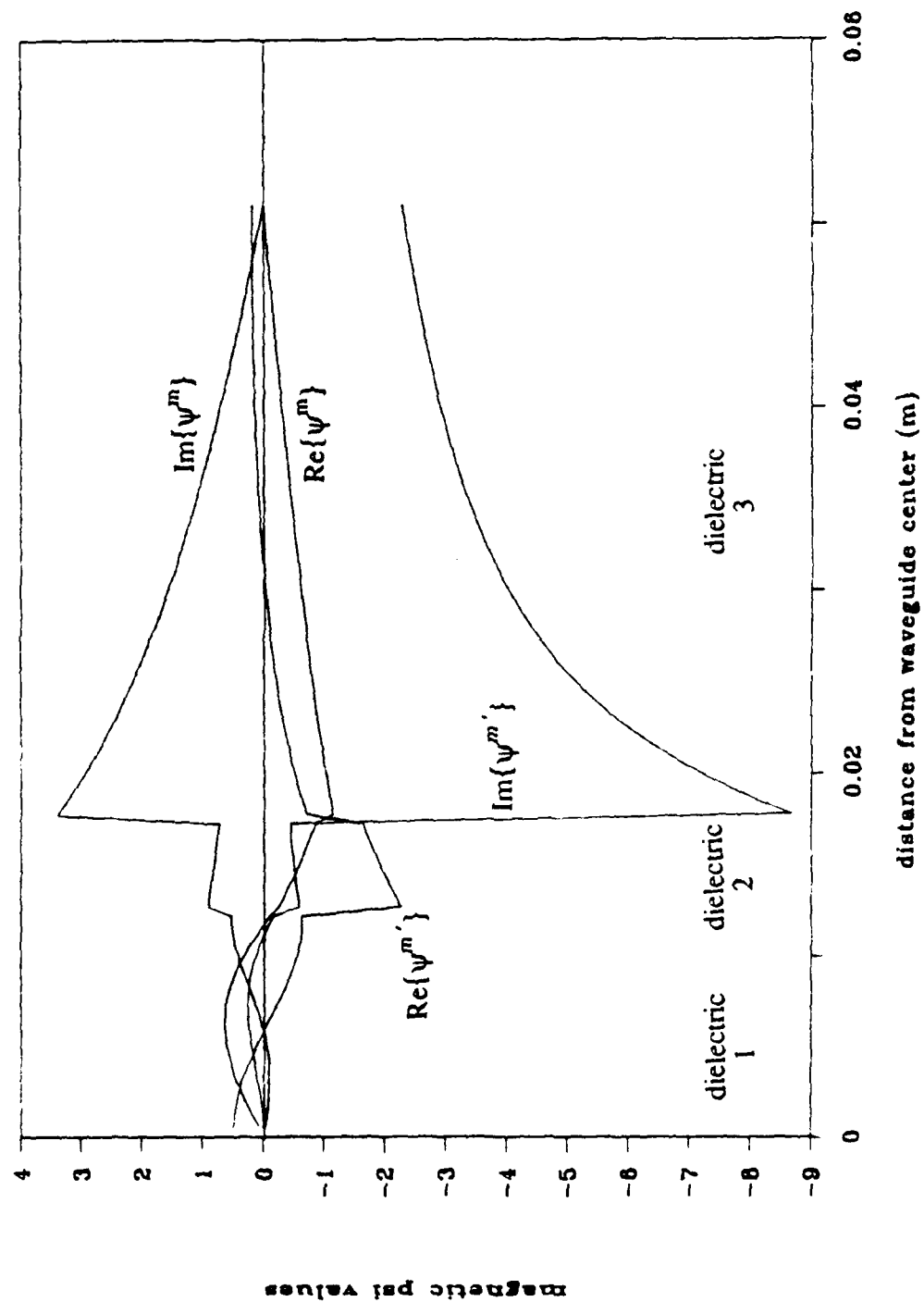


Figure 2.2. Magnetic scalar potential,  $\psi^m$ , and its derivative for the 1 in Teflon pipe filled with methanol at 3 GHz.

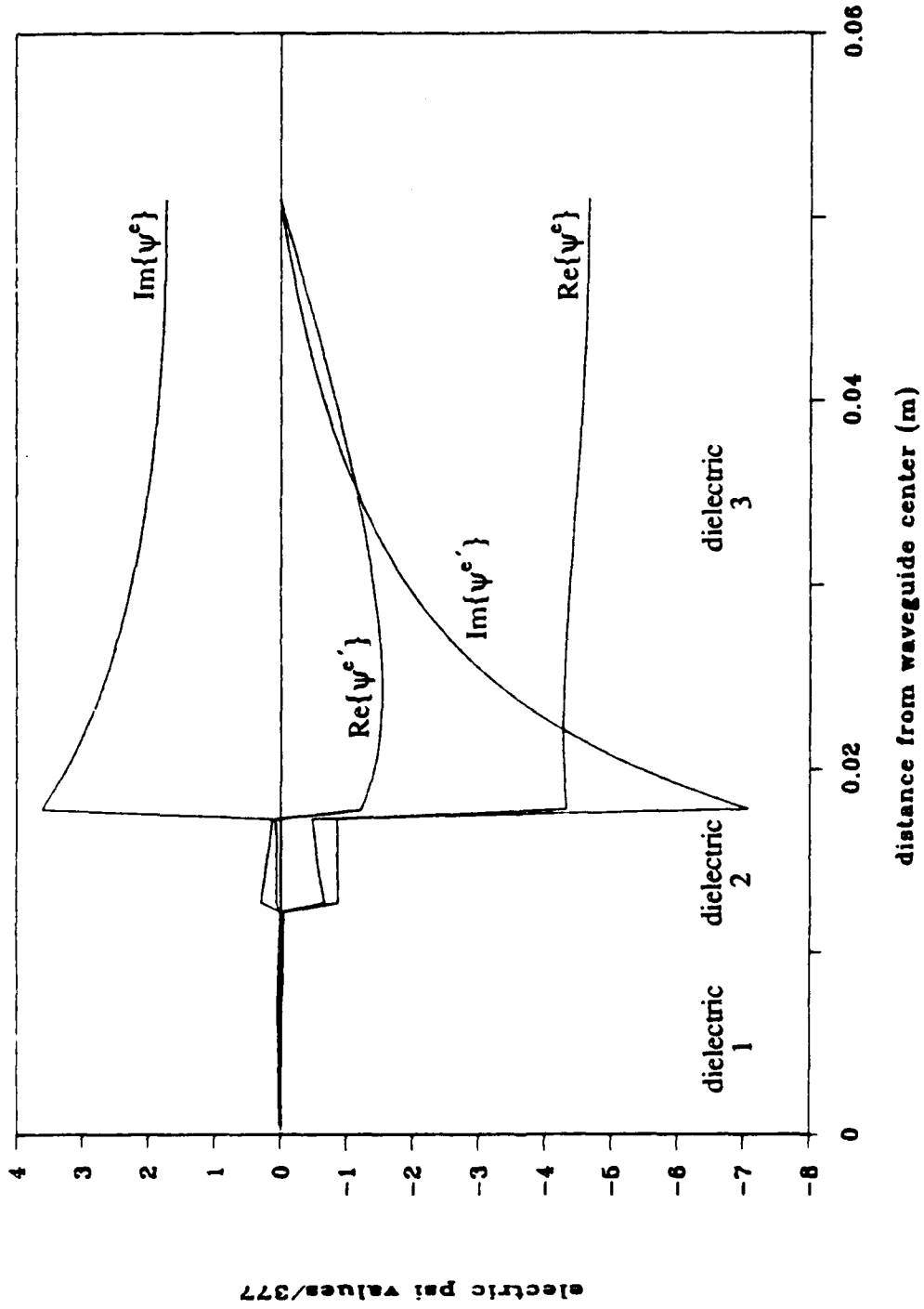


Figure 2.3. Electric scalar potential,  $\psi^e$ , and its derivative for the 1 in Teflon pipe filled with methanol at 3 GHz.

## CHAPTER 3

### NUMERICAL IMPLEMENTATION

The characteristic equations constructed in Chapter 2 are too complicated to solve analytically, and require a numerical treatment instead. This chapter is concerned with computation of these solutions through implementation of a root-finding routine to search for the roots of these characteristic equations. A group of five Fortran computer programs was written to accomplish this task plus many others, including the calculation of  $k_z$  versus  $\omega$  plots,  $k_z$  versus relative radius plots, transverse power flow and more. With space limitations present, only one code, MDCW, is listed here. The other codes are basically derivatives of this main one.

The use of these programs and interpretation of the ensuing data will be demonstrated first for the two-dielectric case. This dielectric-rod insert guide case has been thoroughly investigated in the past as was noted in Chapter 1. Comparison of the results here with those in earlier published work will lend some validity to the theoretical development and confirm the accuracy of the computer programs. In addition to this, some extensions of this earlier work will be presented. Most notable of these is in the area of power flow, where it will be shown that the idea of a backward wave becomes more sharply defined for dielectrically-loaded waveguides.

Much emphasis in this chapter is placed on the two hybrid modes  $HE_{11}$  and  $EH_{11}$ . The reasons for this are that the  $HE_{11}$  mode is always the fundamental mode (has the lowest cutoff frequency) and that the  $EH_{11}$  mode was found to exist in some finite waveguide experiments conducted in the laboratory. Some astonishing modal conversions between these two modes were observed in these experiments. Hence, for a comparison of the theoretical predictions and the experimentally measured results, these modes are emphasized.

### 3.1 Root Finding by Muller's Method

Solutions to (2.26) must, in general, be obtained numerically. This equation can be thought of as a one-dimensional function in the argument  $k_z$

$$f(k_z) = 0 . \quad (3.1)$$

However, if losses are present or in some fashion  $k_z$  becomes complex such as

$$k_z = \beta - j\alpha , \quad (3.2)$$

then the one dimensionality of the function is lost and solutions to (2.26) must be found in the complex plane. Probably the most popular numerical method for solving a generic problem such as (3.1) is the Newton-Raphson method. The difficulty in applying this method, however, is that the derivative of the function must be computed. Since the derivative is unknown analytically and numerical differentiation is not a stable operation, the Newton-Raphson method will not be used. Instead, the roots of (3.1) will be found using Muller's method. This method is a generalization of the widely known secant method, but an inverse quadratic interpolation is used instead of a two-point linear interpolation [26]. Muller's method can be derived by considering the quadratic function [27]

$$f(x) = a(x-x_2)^2 + b(x-x_2) + c . \quad (3.3)$$

The coefficients  $a$ ,  $b$ , and  $c$  can be evaluated with the specification of three initial guesses,  $x_0$ ,  $x_1$ , and  $x_2$ , for the root. The computed root of this quadratic function is

$$x_3 = x_2 - (x_2 - x_1) \left[ \frac{2c}{b \pm \sqrt{b^2 - 4ac}} \right] \quad (3.4)$$

with

$$\begin{aligned} q &\equiv \frac{x_2 - x_1}{x_1 - x_0} \\ a &\equiv qf(x_2) - q(1+q)f(x_1) + q^2f(x_0) \\ b &\equiv (2q+1)f(x_2) - (1+q)^2f(x_1) + q^2f(x_0) \\ c &\equiv (1+q)f(x_2) \end{aligned}$$

A visual image of this quadratic fit and the implementation of this method are shown in Figure 3.1. The zeros of this unique quadratic are calculated and the next point for another quadratic fit is located using  $x_1$ ,  $x_2$ , and now,  $x_3$ . This process is repeated until the zero of the exact function is found within a specified tolerance. The sign in (3.4) is chosen to make the magnitude of the denominator the largest. The two main advantages of this method are that, one, complex roots may be found due to the quadratic nature of the interpolation and, two, the root does not necessarily have to be bracketed with the initial guesses in order to converge. In fact, just as with the secant method, the root may not remain bracketed after the searching process begins even if it initially was. This advantage may also be a disadvantage, since for certain functions, Muller's method may actually diverge from the root depending upon the behavior of the exact function near the root. All-in-all, Muller's method is very useful and accurate for most applications of this type. It has its own shortcomings in certain instances, most of which can be rectified by simply restarting the search routine and changing the initial guesses.

### 3.2 MDCW Computer Program

Muller's method forms the basis of the computer program "MDCW" (Multiple Dielectric Circular Waveguide) which is used, among other things, to solve the characteristic equation (2.26). (A listing of the Fortran source code is given in the Appendix along with a brief description of the program. This program is the basic computer code used in the study of this waveguide problem. Most of the other programs written and used in this work are derivatives in whole or in part of the philosophy and methods employed here.) In order to search for the roots of (2.26), the determinant of the matrix must be computed repeatedly. That is, in each iteration of this root-finding scheme, the function,  $f(k_z)$ , being evaluated is the determinant of  $[A]$ . An efficient method for finding the determinant of a matrix is by LU decomposition [26]. This is a tridiagonalizing method whereby the determinant is computed as the product of the diagonal elements in either an upper or lower triangular matrix. The LU decomposition can also be used to solve a set of linear equations by back substitution which will be of value later on when computing the coefficients  $C_m$ . This method then is efficient in that it can perform double duty so to speak.

The iteration process searching for the root  $k_z$  that satisfies the characteristic equation is terminated upon satisfaction of some predetermined convergence criterion. The criterion chosen here is for two  $k_z$  values to differ by less than some user specified accuracy. Typically  $10^{-8}$  or  $10^{-9}$  is used. Although these are quite small numbers, Muller's method converges extremely fast for the functions encountered here. In addition, specifying small tolerances such as these can actually speed up convergence in some instances as when this program is automated for  $k_z$  versus  $\omega$  plots. Calling these "tolerances" an "accuracy" can be somewhat misleading since convergence to incorrect answers is also possible. Once a certain root has been located, other factors must be taken into account to verify that this is a valid root and the one being sought. These factors

include the value of the determinant, the values of the coefficients and  $k\rho_i$ 's, and the resulting field patterns which can be computed once the coefficients have been solved.

After the  $k_z$  value has been found, the corresponding  $[C]$  vector (cf. (2.25)) can be calculated. Since  $\det[A]=0$  is the root-finding criterion, the rows and columns of  $[A]$  are not all linearly independent. In general, with  $n=(4q-2)$ , the rank of  $[A]$  is  $(n-1)$ . Since there are  $n$  unknowns and now  $(n-1)$  linearly independent equations, one component of the  $[C]$  vector can be chosen arbitrarily. In this case,  $C_{11}$  will be chosen equal to one. (The reason  $C_{11}$  is chosen and not another component is important and will become evident when power flow is discussed.) An inhomogeneous set of equations results of the form

$$\begin{bmatrix} a_{22} & \cdots & a_{2n} \\ \vdots & & \vdots \\ a_{n2} & \cdots & a_{nn} \end{bmatrix} \begin{bmatrix} C_{13} \\ \vdots \\ C_{q4} \end{bmatrix} = - \begin{bmatrix} a_{21} \\ \vdots \\ a_{n1} \end{bmatrix} \quad (3.5)$$

where the  $a$ 's are elements of the  $[A]$  matrix. This system of equations is solved giving the  $C_{rs}$ 's using LU decomposition plus back substitution [26].

The final step in computing the fields from (2.5) and (2.6) is to substitute the  $C_{rs}$ 's into (2.13). This then will give all of the fields throughout the guide. As has been mentioned in Section 2.4, the fields within the guide will be a linear superposition of fields TE and TM to  $z$ .

One principal requirement for this program was that it be able to run on a personal computer (PC). Using Microsoft's Fortran v4.01 and double precision real and complex numbers (64 bits of precision for each of the real and imaginary parts), one total iteration for three dielectrics takes approximately 2 sec on a 12 MHz clocked 286 AT compatible PC with an 8 MHz 80287 math coprocessor. On a 386 Compaq running at 16 MHz with a 16 MHz 80387 math coprocessor, the iteration time is reduced to approximately 1 sec.

Typically, for initial guesses within 5 to 10% of the final answer, 4 to 8 iterations are usually needed to converge. The total times needed to find a solution using a PC, as illustrated here, are certainly reasonable.

The process of calculating  $k_z$  for particular dielectric radii can be automated, enabling  $k_z$  to be plotted as a function of a continuously increasing (decreasing) radius—something similar to a function generator. This is quite useful, among other things, in mode identification. As a standard, the subscripts on  $HE_{nm}$  and  $EH_{nm}$  refer to the  $n^{\text{th}}$  order and the  $m^{\text{th}}$  rank [18]. In a homogeneous guide, the rank is determined by the successive ordering of zeros for  $J_n$ . In the inhomogeneous case this no longer holds. The method of identification used here, as discussed in Section 2.5, is to use the homogeneous guide as a limiting case. Thereby, the dielectric radii within the guide are gradually made larger and the  $k_z$  versus radius plot is made. The starting point for this plot is chosen as the desired TE or TM mode in the homogeneous guide, usually air filled. This method of tracing out the  $k_z$  has a number of advantages over successive applications of MDCW including speed and accuracy. A speed increase is quite obvious since all of the parameters do not need to be entered for each increment in radius. Less obvious is the greater speed realized by using the previous last two calculations for  $k_z$  along with a new calculated guess. This generally halves the number of iterations needed for the calculation of the new root. Accuracy is also increased since it is much easier to stay with the same mode when tracing than with MDCW. One can accidentally jump to other modes with the same order but different rank if the initial guesses are too far from the desired mode.

### 3.3 Results for Two Dielectrics

At this point it may be instructive to consider a few examples and compare the results with published data. Two modes of particular interest are the  $TE_{11}$  and  $TM_{11}$  in addition to their hybrid counterparts the  $HE_{11}$  and  $EH_{11}$  modes. In the homogeneous case,



the  $TE_{11}$  mode is fundamental and the  $HE_{11}$  remains so for the inhomogeneous case, hence, its importance. The importance of the  $EH_{11}$  mode will become more evident later in this chapter and in Chapter 5 when the experimental measurements on the finite guide are discussed. Consider a 0.24 m diameter pec waveguide with a dielectric filling having  $\epsilon_{r1}=10$  and  $\epsilon_{r2}=1$  F/m as in Figure 3.2. For the  $TE_{11}$  mode in an air-filled homogeneous guide,  $k_z=14.3$  rad/m at 1 GHz. There are two ways in which a  $k_z$  versus relative radius plot can be constructed as the insert dielectric rod becomes larger (or smaller) in diameter. One way is with successive applications of MDCW while gradually increasing (decreasing) the radii. The best way is through automation of this process and allowing the computer program to perform these calculations. (As has already been mentioned, due to space limitations, this program is not listed in this thesis.)

Starting the tracing process for an exceedingly small radius, the plot in Figure 3.3 is constructed. The  $HE_{11}$  mode is christened in the limit, as  $a/b \rightarrow 0$  or 1 the  $TE_{11}$  mode is obtained for the homogeneous guide. One way this graph can be interpreted is as a transition diagram from one homogeneous case to another. The  $k_z$  is a function of the inset radius and is known analytically only for the homogeneous cases, i.e., at the endpoints. This graph indicates how the axial wavenumber varies between the two homogeneous situations. This plot compares well with one given by Harrington [21] and is, in fact, an exact match. The transverse electric fields for the four cases labeled A, B, C and D are shown in Figure 3.4. In each case,  $E_\rho$  is discontinuous at the boundary by the accumulation of bound charge at this interface. The  $E_\phi$  field is particularly interesting in that the field maximum begins outside the dielectric rod and gradually moves inside as the rod radius is increased. Related to this is the transformation of  $k_{\rho 2}$  from a purely real to a purely imaginary quantity at  $k_z/k_0=1$ . The wavenumbers are listed in Table 3.1 for these four cases. The region much below this point is characterized by electric fields primarily concentrated in the outer dielectric, whereas the region much above  $k_z/k_0=1$  has its electric fields concentrated in the inner dielectric. The magnetic fields retain most of their shape as

$a/b$  is increased with the maximum fields located in the center dielectric. The transverse electric fields also display an increasingly exponential behavior in region 2 as  $a/b$  increases. This is a further manifestation of the imaginary behavior of  $k_{\rho 2}$  which gives rise to "trapped" waves in the inner dielectric. Imaginary arguments for the Bessel functions in (2.14) give linear combinations of modified Bessel functions which vary smoothly as opposed to the oscillatory behavior of the normal Bessel functions. Behavior of this sort is reminiscent of surface waves and demonstrates itself here for  $k_{\rho 2}$  sufficiently large and imaginary. If there were a coating instead of an insert (meaning  $\epsilon_{r1}=1$  and  $\epsilon_{r2}>1$ ), then the situation would be reversed. Discussions of this arrangement are given by Chou and Lee [7] and Lee *et al.* [28].

Another interesting example is an air-filled waveguide of 1 in diameter having a dielectric insert of  $\epsilon_{r1}=37.6$  F/m. For the  $TE_{11}$  mode in an air-filled guide,  $k_z=-j118.3$  rad/m at 4 GHz serves as a starting point for the  $k_z$  versus relative radius plot, with the results of this given in Figure 3.5. This graph has a peculiar shape in that the  $HE_{11}$  and  $EH_{11}$  modes tend to form a continuous curve. This is in stark contrast to these similar plots for the homogeneous case. Also, a backward-wave region (where the phase and group velocities have differing signs) has formed in the  $k_z$  versus  $a/b$  plot where the slope is negative. This backward-wave assignment can be arrived at here by rewriting  $a/b$  as  $\frac{a\omega}{\alpha c}$  with  $c$ =speed of light and  $\alpha$  is a constant. The x axis can now be thought of as an increment in  $\omega$  instead of  $a/b$ . Although this graph was generated as a  $\beta$  versus relative radius plot, the x axis can be regarded as proportional to frequency from which backward-wave assignments can be made by observing the slope so long as the constitutive parameters are not frequency dependent.

Another interesting feature of this graph is the region from  $a/b=0.302$  to  $0.358$  where no purely real or purely imaginary solutions for  $k_z$  exist. Instead, complex solutions are found in the form of (3.2). These solutions are the complex or "leaky" modes

discussed in Chapter 1 and have been investigated in some detail in the literature [14], [29], [30]. For conservation of energy reasons, these modes exist in pairs having negative complex conjugate propagation coefficients  $k_z$  and  $-k_z^*$ . In this trace, the backward-wave and complex mode regions exist simultaneously. Clarricoats and Taylor [14] show that this is always the case for the two-dielectric inhomogeneity but the converse does not apply. That is, complex modes can exist without propagating backward-wave regions. Later in Section 4.2 this same occurrence will be shown to exist in the three-dielectric inhomogeneity. Since there is no fundamental difference between three dielectrics and four or more, it can be safely stated that for any number of dielectric layers, the existence of propagating backward waves in a  $k_z$  trace is always accompanied by a complex mode region, but not necessarily *vice versa*.

Once this plot has been constructed, the transverse fields can be computed using the  $k_z$  value for the desired relative radius. Choosing  $a/b=0.788$ , then from Figure 3.5,  $k_z=461.7$  rad/m for the  $HE_{11}$  mode and  $k_z=265.1$  rad/m for the  $EH_{11}$  mode. The fields for these two cases as computed by MDCW are shown in Figures 3.6 and 3.7. They are all normalized so that the maximum field component, either E or H, has a magnitude of one. Figures 3.6 (a) and (b) show the transverse electric and magnetic fields, respectively, for the  $HE_{11}$  mode. All of the fields are continuous except for the  $E_\rho$  component which is discontinuous by the accumulation of bound charges. Similar plots for the  $EH_{11}$  mode are shown in Figure 3.7. These graphs compare exactly to those of Zaki [4] except for a different normalization of the H fields. Zaki also subscribes to some nonstandard nomenclature for the modal designations [3]. Graphs of these mode patterns are shown in Figure 3.8. Figure 3.6 agrees with Figure 3.8(a) and Figure 3.7 with 3.8(b). The excellent correspondence shown here serves as a good source of verification for the accuracy and validity of the results from the programs for two dielectrics. For more than two, verification will be provided by experimentation. It is not surprising that such good agreement has been reached. The analysis used here and that of Zaki are founded on the

same approach, namely, expression of the eigenmodes as a product of the expansion functions as in Chapter 2. Figure 3.8 also contains the field patterns for the transverse E and H fields across the waveguide cross section.

Up to this point, fairly typical topics have been discussed concerning the multielectric waveguide. Now, some additional discussions will be given for the two-dielectric case. These examples, which include  $k_z$  versus  $\omega$ ,  $k_z$  versus  $\epsilon_{r1}$ , and 3-D power flow plots, will lend further insight into the rod-insert guide and also bridge the way for three and more dielectrics.

### 3.4 Other Axial Wavenumber Plots

The first of these plots to be demonstrated is the  $k_z$ - $\omega$  plot for the frequencies 1 to 10 GHz. Construction of this begins by determining the starting point for the frequency and mode of interest. This is done by tracing out the  $k_z$  versus relative radius plot at 1 GHz. The results of this are shown in Figure 3.9 for  $b=0.5$  in,  $\epsilon_{r1}=37.6$  and  $\epsilon_{r2}=1$  F/m. The two modes shown are  $HE_{11}$  and  $EH_{11}$ . Again, a region of complex mode solutions exists as for the 4 GHz case except that here it connects two evanescent hybrid mode regions. It is interesting to observe that in this complex-mode region the distinction between  $HE_{11}$  and  $EH_{11}$  disappears and both modes seem to exist simultaneously. It is in this complex-mode region where the starting point for the  $k_z$ - $\omega$  plot is obtained at  $a/b=0.788$ . Since  $HE_{11}$  and  $EH_{11}$  appear to exist simultaneously at this point, it suffices as a starting point for both  $k_z$ - $\omega$  plots. The resulting  $k_z$ - $\omega$  curves are shown in Figure 3.10. At a frequency slightly greater than 2 GHz, the modes revert from complex to hybrid with the  $EH_{11}$  experiencing a small backward-wave region from approximately 2 to 2.4 GHz.

Also in Figure 3.10 are the  $\beta$ - $\omega$  plots above cutoff for the  $TE_{11}$  and  $TM_{11}$  modes in the homogeneously filled guide of 1 in diameter with  $\epsilon_r=37.6$  F/m. At lower frequencies, one can see a large discrepancy between the transverse and hybrid modes as

expected. At higher frequencies, however, it is quite surprising that the plots all have basically the same shape and trends. This indicates that the inhomogeneous guide could be modelled as homogeneous at frequencies much beyond cutoff, at least for these two cases, by selecting an effective  $\epsilon_r$ .

In addition to the variation of  $k_z$  as a function of  $\omega$ , is the important case in which  $k_z$  varies as a function of the dielectric  $\epsilon_{r_i}$ . This is useful from a number of standpoints. One, as different loading materials are used, the cutoff frequency of the composite structure can be observed. Two, the variation in attenuation afforded by each mode can be scrutinized as the imaginary part of  $\epsilon_{r_i}$  (representing conduction losses) is varied. An example of the former is shown in Figure 3.11 for the two-dielectric problem having  $a/b=0.788$ ,  $b=0.5$  in and  $\epsilon_{r_2}=1$  F/m at 4 GHz. The inner dielectric's real permittivity is varied from 1 to 38 F/m for both the  $HE_{11}$  and  $EH_{11}$  modes. For  $\epsilon_{r_1}=1$  F/m, both modes revert to the homogeneous case which serves as a convenient starting point for mode classification reasons. As the dielectric constant is increased,  $k_z$  increases monotonically in these two situations. Cutoff occurs at  $\epsilon_{r_1}=5.3$  and  $\epsilon_{r_1}=13.9$  F/m for the  $HE_{11}$  and  $EH_{11}$  modes, respectively.

### 3.5 Power Flow

Power flow is an important topic in waveguide considerations and will be discussed here for the multielectric case. In the most general sense, the total power across some transverse plane along the guide is given by

$$P = \int_S \mathbf{E} \times \mathbf{H}^* \cdot d\mathbf{s} \quad (3.6)$$

where the \* refers to complex conjugation. In general, all six components of both E and H will exist, but since only the z directed power flow is of importance here

$$S = E \times H^*$$

and

$$S_z = E_{\rho_i} \cdot H_{\phi_i}^* - E_{\phi_i} \cdot H_{\rho_i}^* \quad i = 1, \dots, q \quad (3.7)$$

Considering Equations (2.5) and (2.6) for the  $\rho$  components gives

$$E_{\rho_i} = - \left[ \frac{k_z k_{\rho_i}}{\omega \epsilon_i} \hat{\psi}_i^m{}' h^m(n\phi) + \frac{n}{\rho} \hat{\psi}_i^e h^m(n\phi) \right] \quad (3.8)$$

$$H_{\rho_i} = - \left[ \frac{k_z k_{\rho_i}}{\omega \mu_i} \hat{\psi}_i^e{}' h^e(n\phi) + \frac{n}{\rho} \hat{\psi}_i^m h^e(n\phi) \right] \quad (3.9)$$

where the primes denote differentiation in accordance with (2.19). Substituting these two equations plus (2.17) and (2.18) into (3.7) gives in part

$$\begin{aligned} E_{\rho_i} \cdot H_{\phi_i}^* = & \left[ \frac{k_z}{\omega \epsilon_i} |k_{\rho_i} \hat{\psi}_i^m{}'|^2 + \frac{n^2 k_z^*}{\omega \mu_i^* \rho^2} |\hat{\psi}_i^e|^2 \right. \\ & \left. + \frac{n k_{\rho_i} |k_z|^2}{\omega^2 \epsilon_i \mu_i^* \rho} \hat{\psi}_i^m{}' \hat{\psi}_i^e{}^* + \frac{n k_{\rho_i}^*}{\rho} \hat{\psi}_i^e \hat{\psi}_i^m{}'{}^* \right] [h^m(n\phi)]^2 \end{aligned} \quad (3.10)$$

$$E_{\phi_i} \cdot H_{\rho_i}^* = - \left[ \frac{k_z^*}{\omega \mu_i^*} |k_{\rho_i} \hat{\psi}_i^e{}'|^2 + \frac{n^2 k_z}{\omega \epsilon_i \rho^2} |\hat{\psi}_i^m|^2 \right. \quad (3.11)$$

$$+ \frac{nk_{p_i}^* |k_z|^2}{\omega^2 \epsilon_i \mu_i^* \rho} \hat{\psi}_i^m \hat{\psi}_i^{e'} + \frac{nk_{p_i}}{\rho} \hat{\psi}_i^e \hat{\psi}_i^{m*} [h^e(n\phi)]^2.$$

Equation (3.7) can be used to calculate the power flow in the z direction by Equations (3.10) and (3.11). In particular, the real part of  $S_{z_i}$  is of primary importance in this study since it represents the time-averaged power flow in the axial direction.

An important special case is the azimuthally symmetric modes for which  $n=0$ . Equation (3.7) then reduces to

$$\begin{aligned} S_{z_i} &= \frac{k_z}{\omega \epsilon_i} |k_{p_i} \hat{\psi}_i^{m'}|^2 \\ &= \frac{k_z}{\omega \epsilon_i} |k_{p_i} [C_{11} J_n'(k_{p_i} \rho) + C_{12} N_n'(k_{p_i} \rho)]|^2. \end{aligned} \quad (3.12)$$

If the guide is homogeneous, only one coefficient will be left, namely,  $C_{11}$ . To ensure nonzero power flow, this coefficient is chosen equal to one when solving for the coefficients  $[C]$ . This is important since it was found that in the limit as the guide becomes homogeneous, choosing other coefficients equal to one may force the  $C_{11}$  coefficient to zero in the case where  $n=0$ . Since nonzero  $S_{z_i}$  is to be expected, a boundary condition of sorts is implied by this seemingly nonphysical result.

An example of the power flow through a cross section of a waveguide is shown in Figures 3.12 and 3.13. These figures contain graphs of the three-dimensional (3-D) power flow along with a slice through the middle of the 3-D plot in the  $\phi=0$  plane. Figure 3.12 corresponds to the point labeled A in Figure 3.3 and Figure 3.13 corresponds to point D. These two graphs show a tremendous redistribution of the power flow from largely in the outer dielectric to mostly in the inner dielectric. For  $a/b=0.1$ , 99.5% of the power is in the outer dielectric while for  $a/b=0.4$ , 95% of the power concentrates in the inner. Although the radius of the inner dielectric increases fourfold, at  $a/b=0.4$ , the inner dielectric still only

comprises 16% of the cross-sectional area. A question arises as to why the power shifts in concentration. This redistribution of power is marked by the magnitude and phase of  $k_{\rho 2}$ . As  $k_{\rho 2}$  becomes increasingly imaginary, the power tends to concentrate in the inner dielectric as noted by these two figures and the values in Table 3.1. Although the  $k_{\rho 2}=0$  point at  $a/b=0.244$  does not mark a 50/50 power distribution between inner and outer dielectrics (this actually occurs at  $a/b=0.267$ ), a large imaginary radial wavenumber does signal a small real axial power flow in that dielectric.

Another example is shown in Figure 3.14. This plot is for the point labeled C in Figure 3.5 having  $k_z=165$  rad/m in the  $HE_{11}$  mode. Here  $a/b=0.36$  and  $b=0.5$  in. One interesting feature of this power plot is the existence of regions, in the vicinity of the  $\phi=0$  plane, where power is actually flowing backwards towards the source. In this particular example, the total net power flow is positive with 69% of the power concentrated in the inner dielectric and 31% in the outer dielectric and negative. However, the inner dielectric covers only 13% of the cross-sectional area of the waveguide. This is another good example of how the axial power flow concentrates in the dielectric with a higher real radial wavenumber. This is a rule, in general, but the actual percentages are also a function of the mode type and the relative dielectric radii.

The negative power flow phenomenon seen above appears to be a remnant, so to speak, from the backward-wave region. That is, from taking a number of cases along the  $\beta$  versus relative radius plot, it was determined that the power flow in the center and outer dielectrics is oppositely directed for all values of  $a/b$  in these two modes. The results of this are shown in Table 3.2. Although the last entry has a positive value in the outer region, there still is some negative flow; however, it is less than the positive flow in that annulus. The values listed in Table 3.2 are ordered as one would trace out an ascending path along the outside edge of the plot in Figure 3.5 beginning at point A. Examining these percentages, a picture begins to emerge of the power flow slowly diminishing in the backward direction within the inner dielectric and a greater percentage going forward.



Further insight into this is gained through consideration of Figure 3.15 which is the power flow plot for point A in Figure 3.5 and the first entry in Table 3.2. Here the positive power flow is in the outer dielectric and the negative within the inner. Owing to the backward-wave nature of the wave here, the phase fronts are toward the source and the energy propagation is away. In the backward-wave region, the power flow is positive in the outer dielectric, negative in the inner. The converse of this applies to the forward-wave region of the  $EH_{11}$  mode at  $a/b=0.5815$  depicted in Figure 3.16.

This concept of a "backward wave" seems to be somewhat muddled for the multiple dielectric cases considered here since power is actually traveling in both directions in both the forward- and backward-wave regions! One needs to keep in mind that in the backward-wave region, the phase and group velocities have opposite signs. To choose the correct sign for  $k_z$ , as in Table 3.2, an introduction of a small amount of loss to the inner dielectric will make the right choice apparent. Letting  $\epsilon_{r1}=37.6-j0.01$  F/m for the case with  $a/b=0.3646$  in Figure 3.15, two roots to the characteristic equation were found using MDCW. These are  $k_z=68.22+j0.179$  and  $k_z=-68.22-j0.179$  rad/m. The first represents an augmented, forward traveling wave while the second an augmented backward one. The second is the correct one since the augmentation is bounded by the source and hence a physical result. In this backward-wave region, the correct result for  $k_z$  is with both  $\beta$  and  $\alpha$  negative. This is the reason for plotting  $\text{abs}(\beta)$  in Figures 3.5 and 3.10, for example.

It is also interesting to inquire as to which mode, either  $HE_{11}$  or  $EH_{11}$ , to name the backward-wave region. By Snitzer's scheme for the sign of  $C_{11}/C_{13}$ , the mode is correctly called  $EH_{11}$  since the sign is negative. However, if  $\beta$  were mistakenly chosen as positive, the  $HE_{11}$  mode would result since the sign of the ratio then becomes positive. In the past, the backward-wave region would indeed be labelled  $HE_{11}$ . In the next chapter, it will be shown in considerable detail that this region is actually part of the  $EH_{11}$  mode trace.

Table 3.1.

Wavenumbers of the four cases labelled in Figure 3.3 for the  $HE_{11}$  mode in the rod-insert guide having  $b=0.4\lambda$ ,  $f=1$  GHz,  $\epsilon_{r1}=10$  and  $\epsilon_{r2}=1$ .

Case	$k_z$ (rad/m)	$\frac{a}{b}$	$k_{p1}$ (rad/m)	$k_{p2}$ (rad/m)
A	14.85	0.1	64.59	14.79
B	17.39	0.2	63.95	11.70
C	34.37	0.3	56.66	-j27.25
D	49.36	0.4	44.22	-j44.69

Table 3.2.

Axial wavenumber and percent total axial real power flow for the five cases labelled in Figure 3.5 for both the  $HE_{11}$  and  $EH_{11}$  modes in the rod-insert guide having  $b=0.5$  in,  $f=4$  GHz,  $\epsilon_{r1}=37.6$  and  $\epsilon_{r2}=1$ .

Case	$k_z$ (rad/m)	$\frac{a}{b}$	% of total real power flow	
			inner	outer
A	-68	0.3646	-22.77	77.23
B	-89	0.3600	-31.61	68.39
C	165	0.3600	68.76	-31.24
D	262	0.3900	94.42	-5.58
E	462	0.7880	99.78	0.22

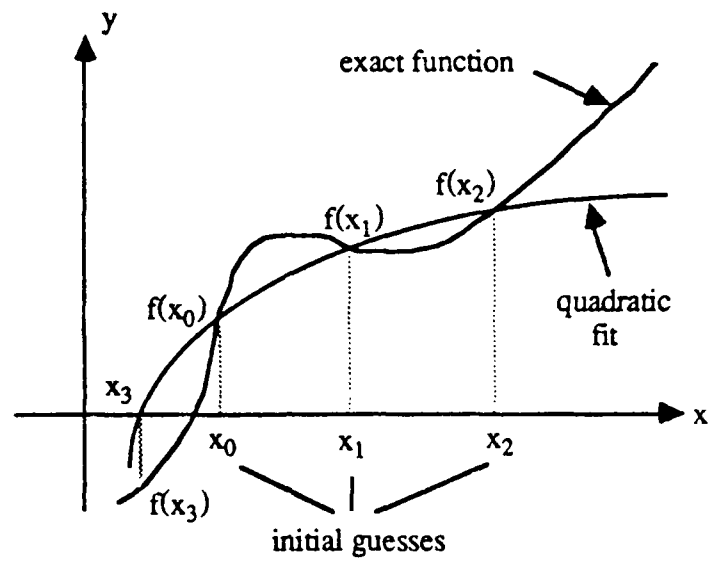


Figure 3.1. Example of the quadratic fit procedure to locate the zero of a function by Muller's method.

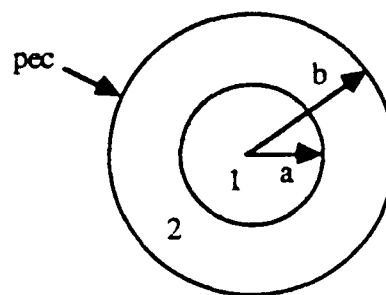


Figure 3.2. Rod-insert waveguide arrangement.

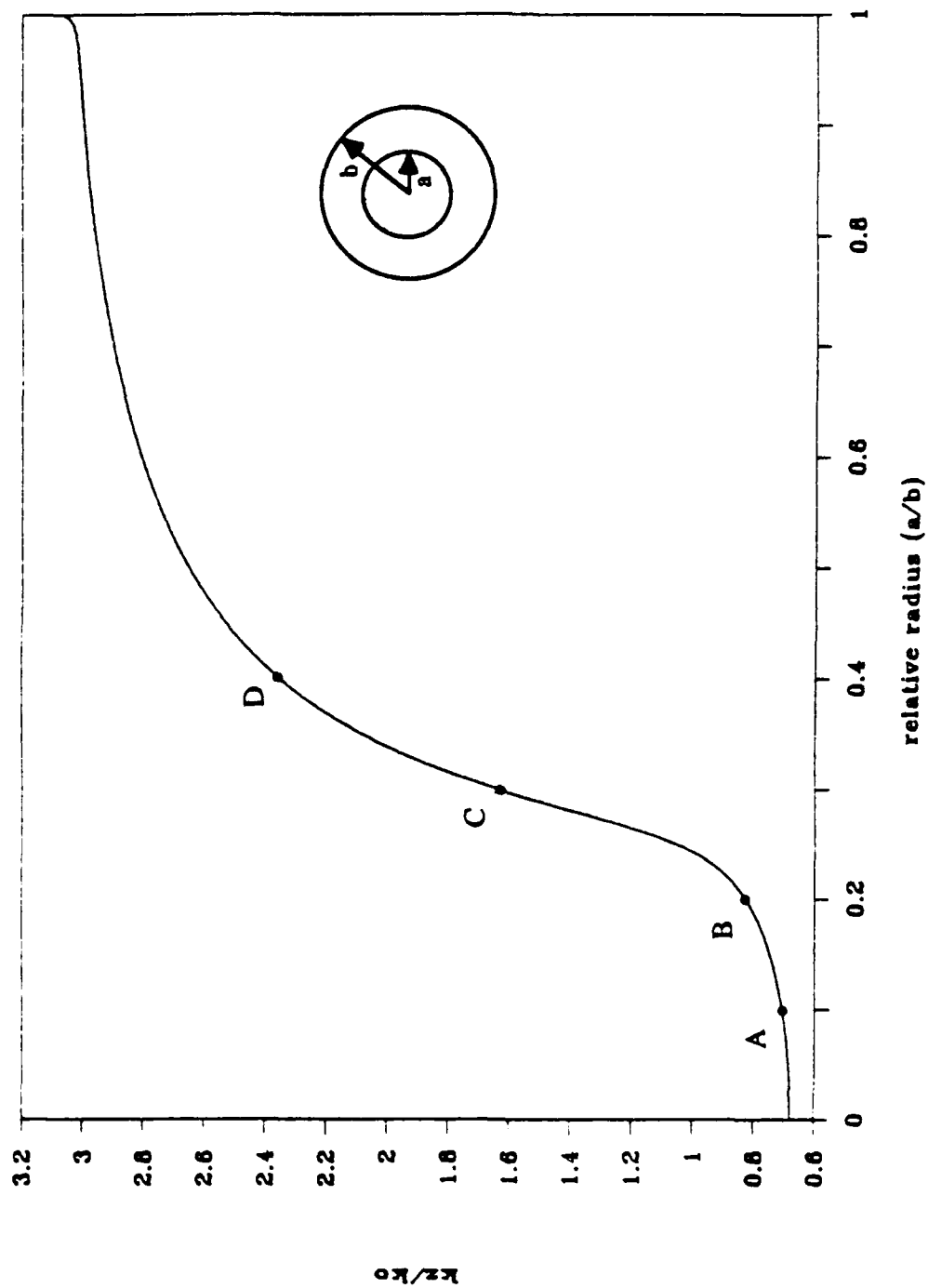
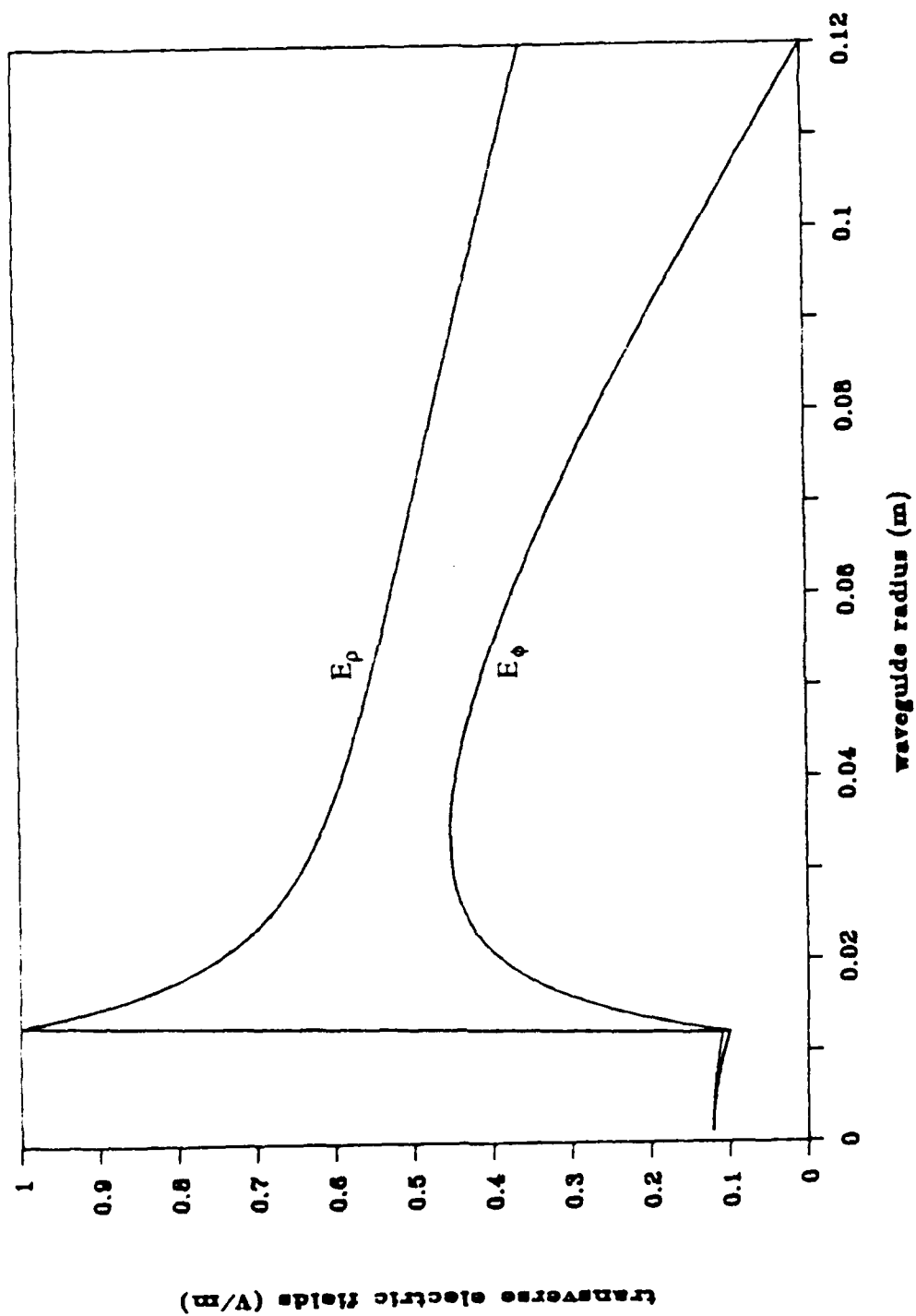


Figure 3.3. Normalized  $k_z$  versus relative radius plot for the  $HE_{11}$  mode in the rod-insert guide having  $b=0.4\lambda$ ,  $f=1$  GHz,  $\epsilon_{r1}=10$  and  $\epsilon_{r2}=1$ .



(a) Electric fields corresponding to the  $k_z$  of point A in Figure 3.3.

Figure 3.4. Transverse electric field magnitudes for the four cases, A, B, C and D, in Figure 3.3 of the  $HE_{11}$  mode, corresponding to parts (a), (b), (c) and (d), respectively.

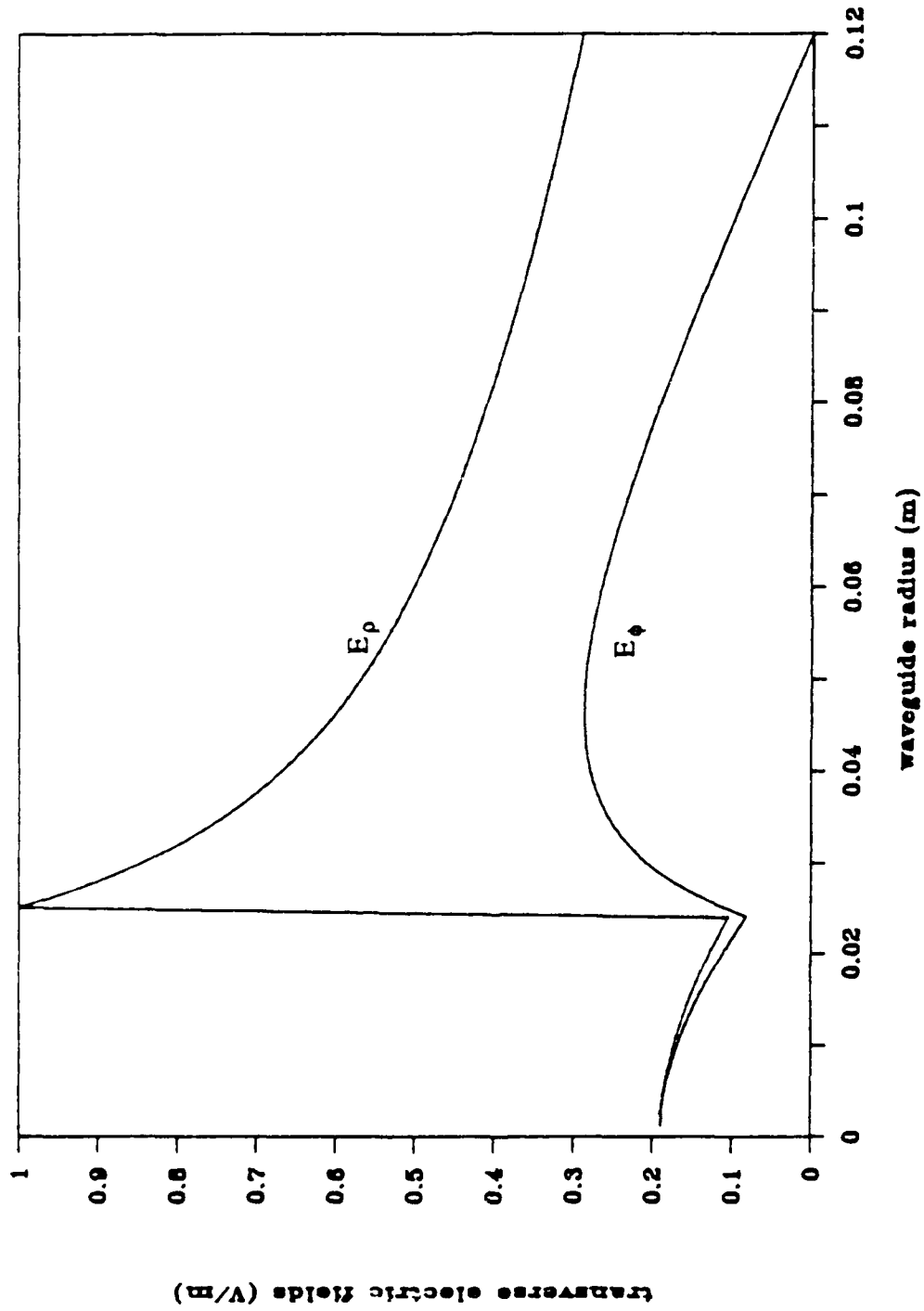


Figure 3.4. (b) Electric fields corresponding to the  $k_z$  of point B in Figure 3.3.

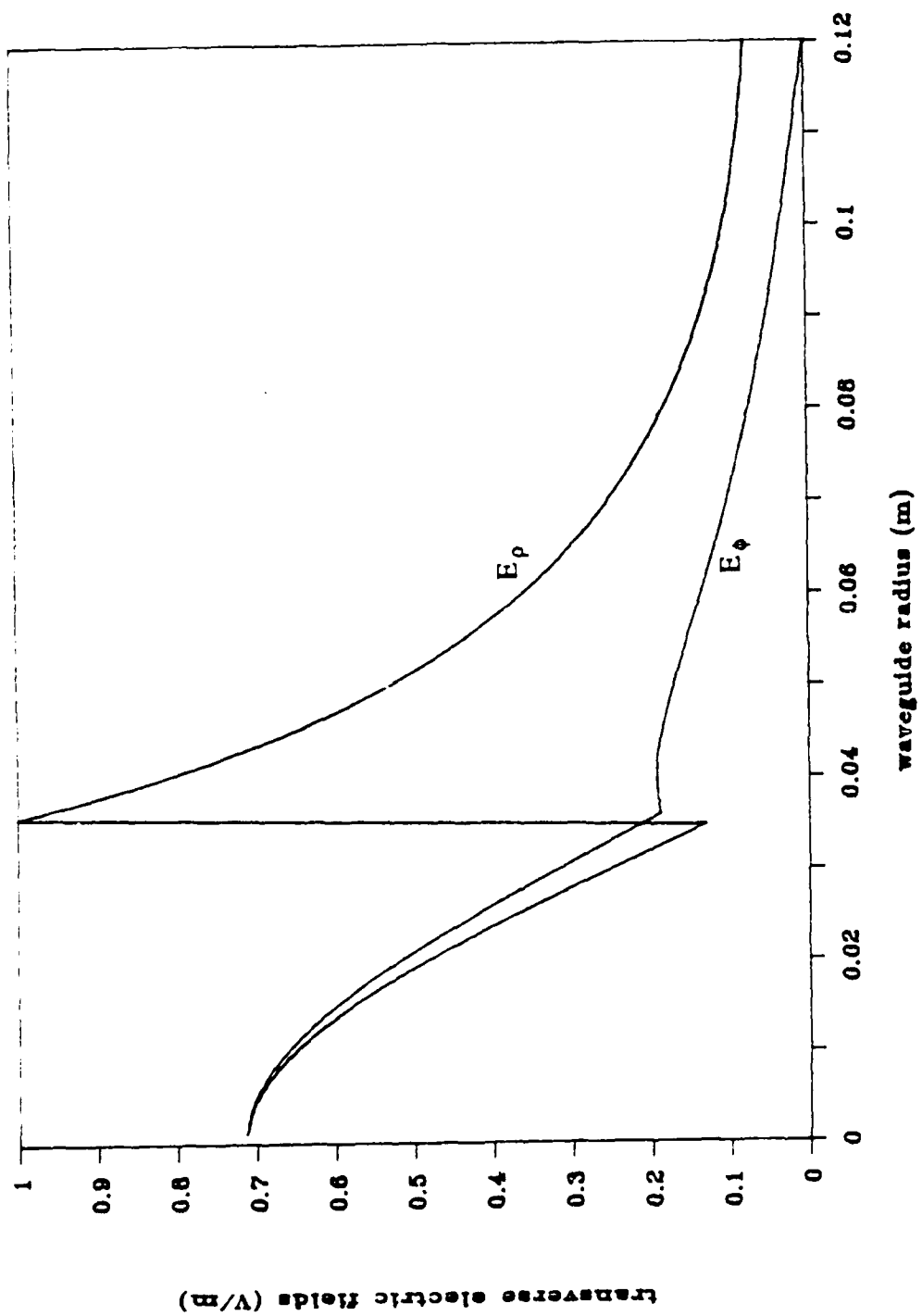


Figure 3.4. (c) Electric fields corresponding to the  $k_z$  of point C in Figure 3.3.

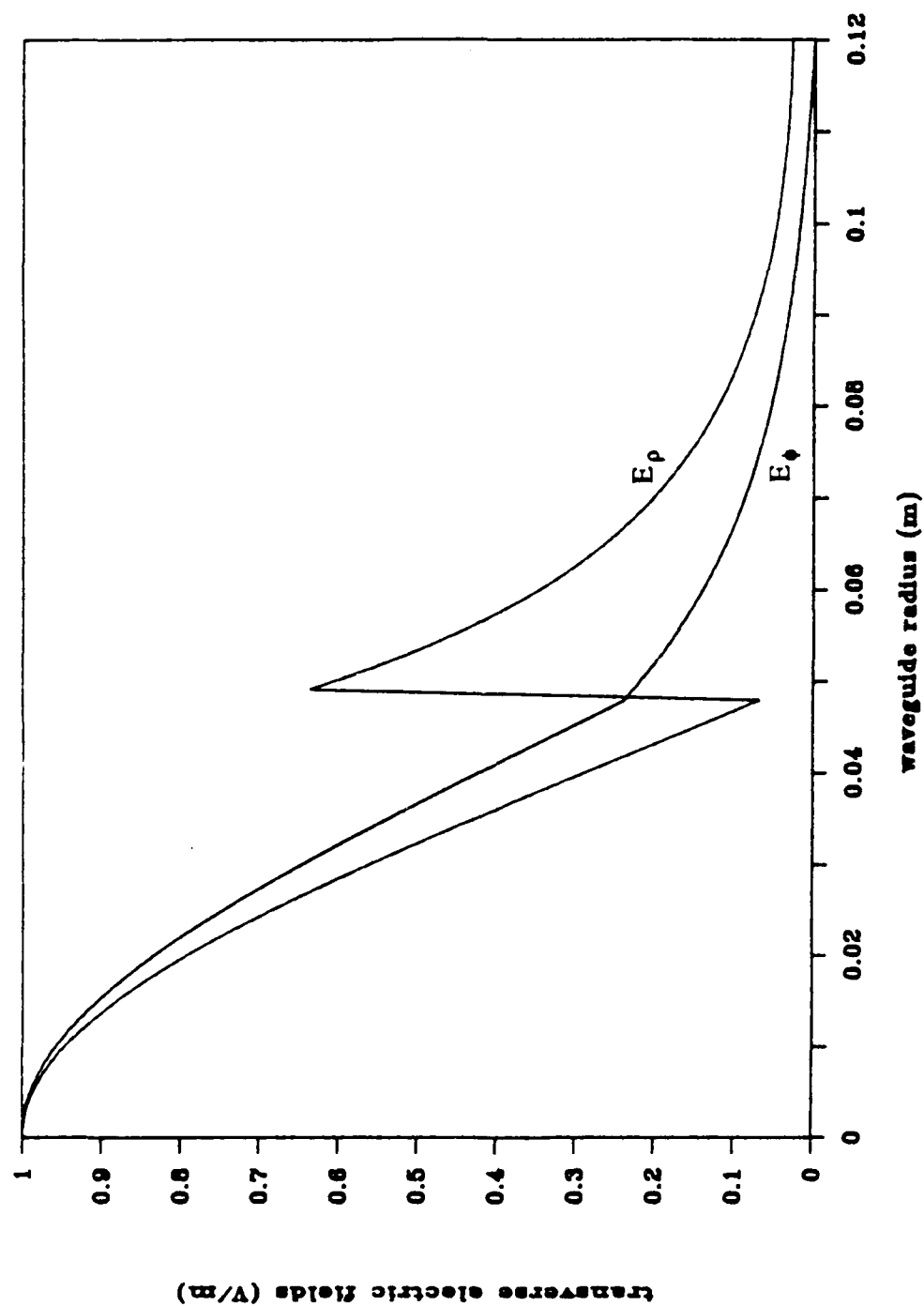


Figure 3.4. (d) Electric fields corresponding to the  $k_z$  of point D in Figure 3.3.



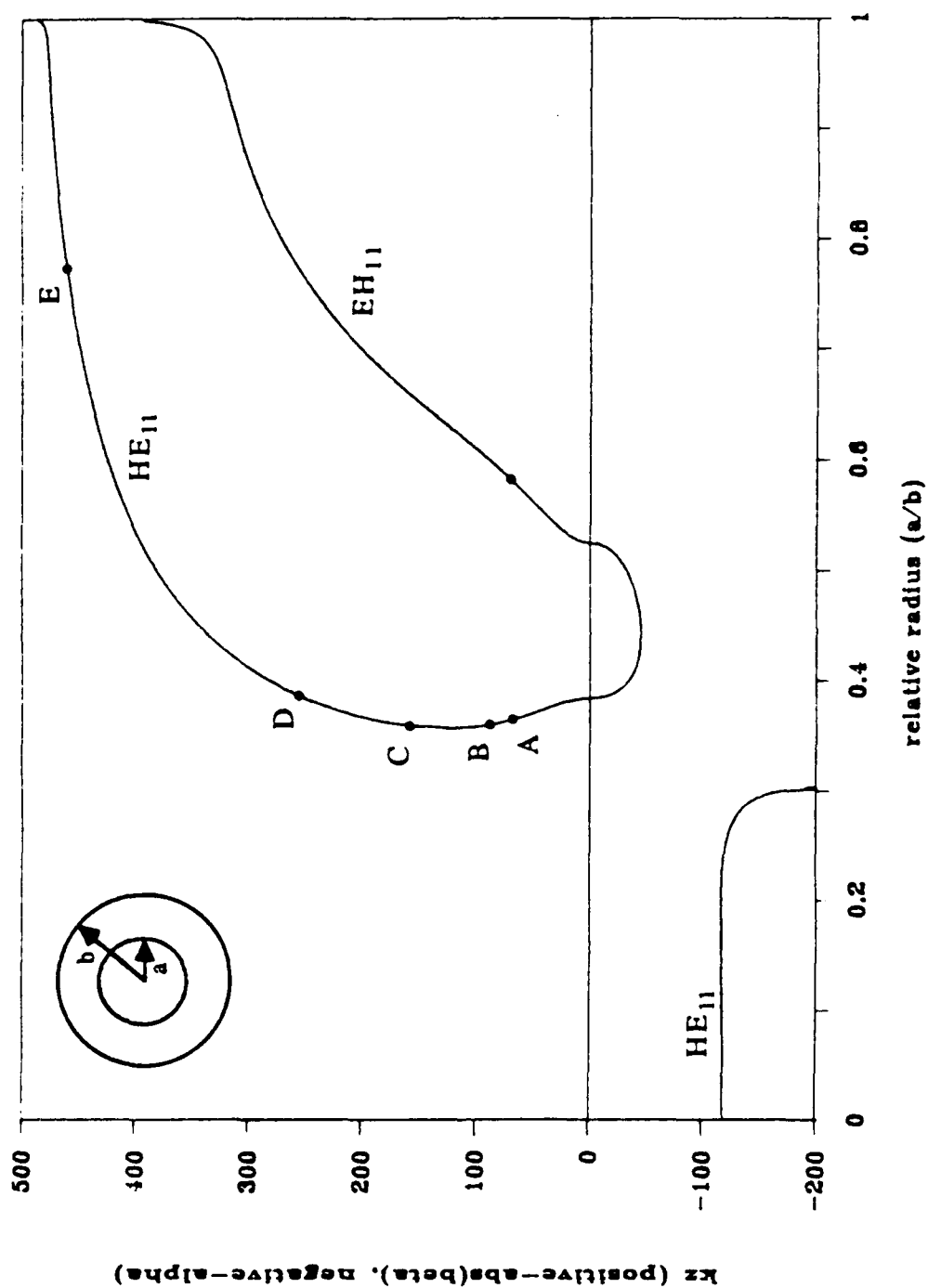
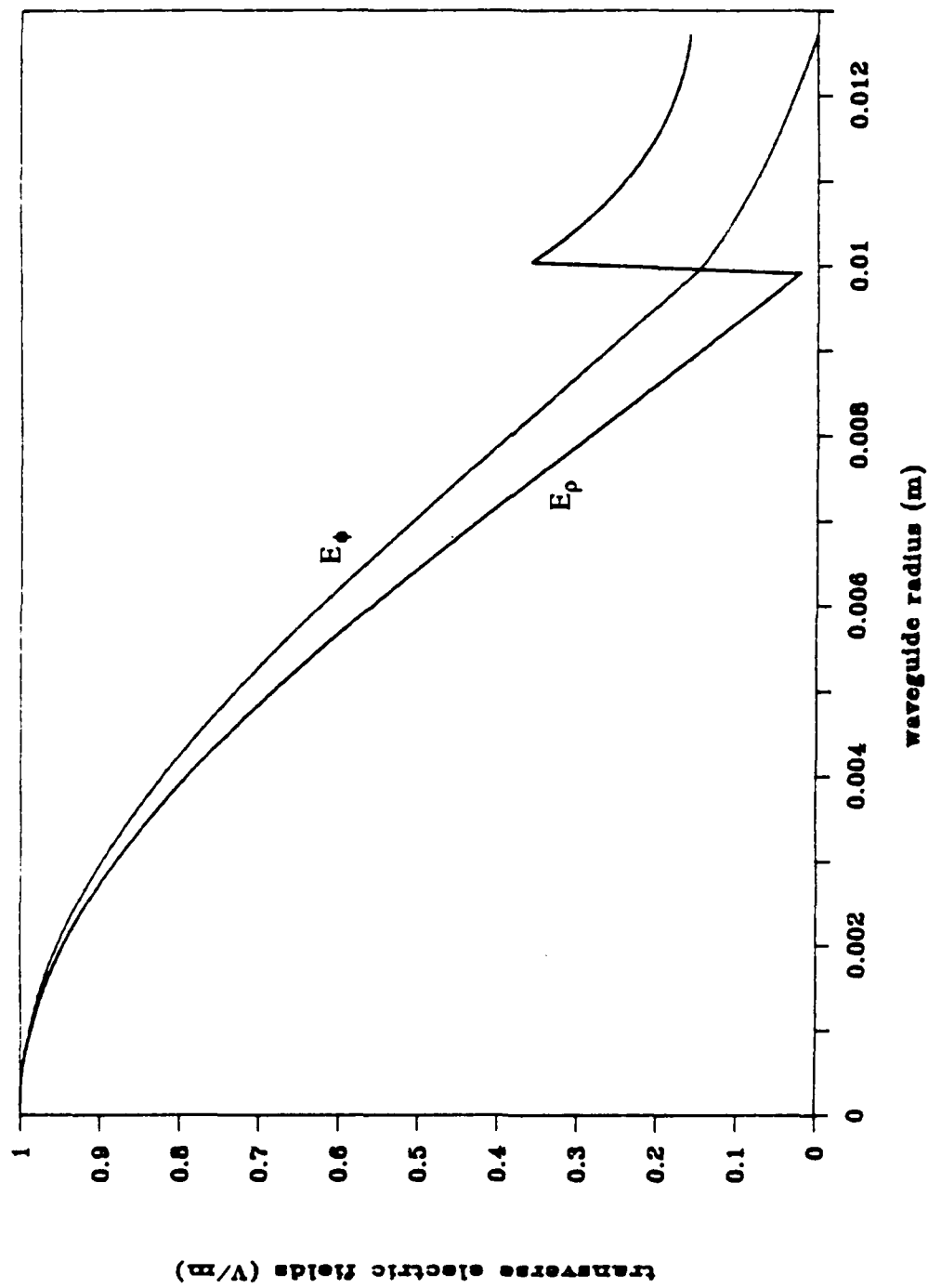


Figure 3.5. Trace of  $k_z$  versus relative rod radius for the  $HE_{11}$  and  $EH_{11}$  modes in the rod-insert waveguide having  $b=0.5$  in,  $f=4$  GHz,  $\epsilon_{r1} \approx 37.6$  and  $\epsilon_{r2}=1$ .



(a) Transverse E field magnitudes

Figure 3.6. Transverse (a) E and, (b) H field magnitudes, for the  $HE_{11}$  mode of the rod-insert waveguide having  $a/b=0.788$ ,  $b=0.5$  in,  $f=4$  GHz,  $\epsilon_{r1}=37.6$  and  $\epsilon_{r2}=1$ .

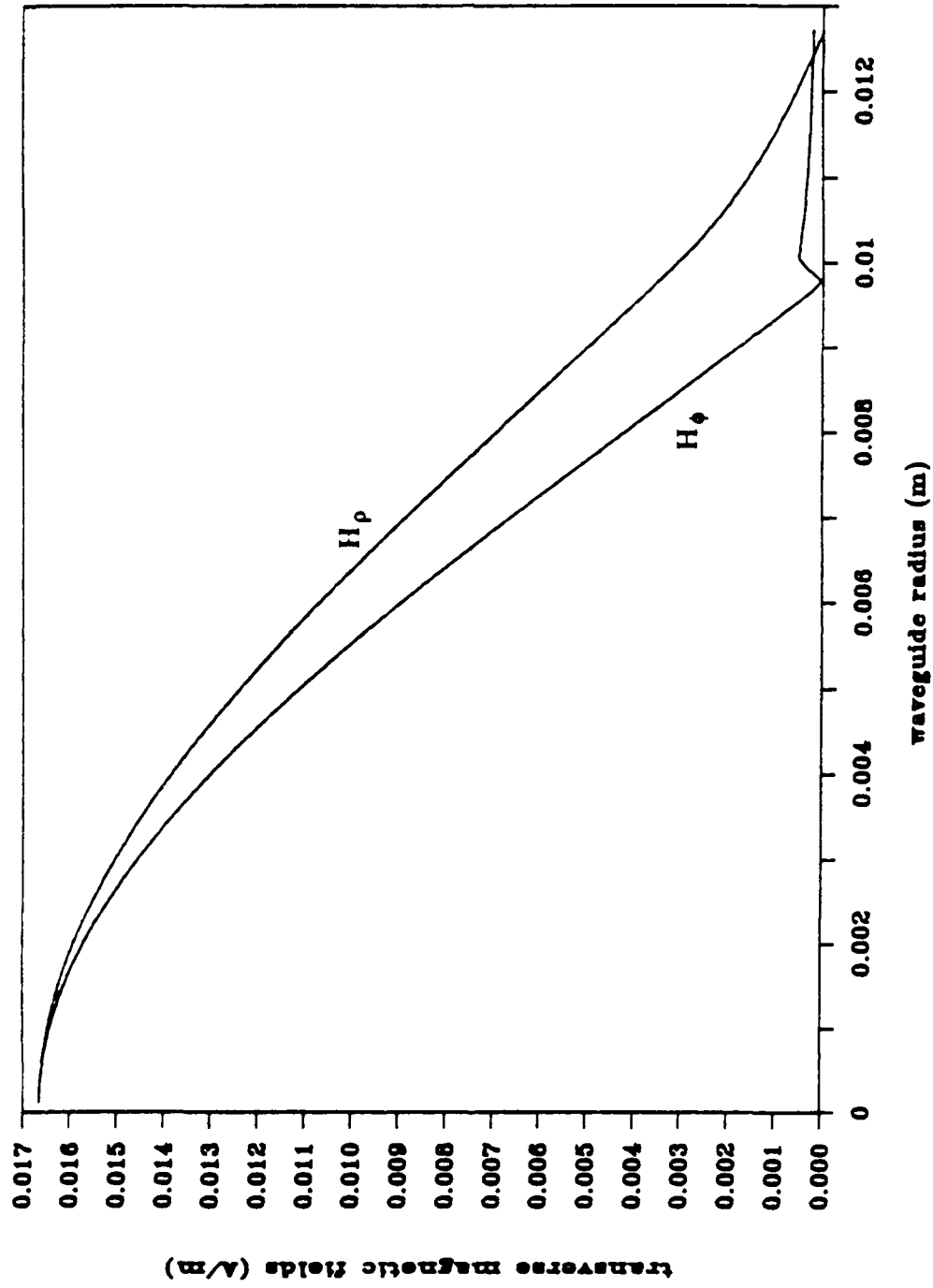


Figure 3.6. (b) Transverse H field magnitudes.

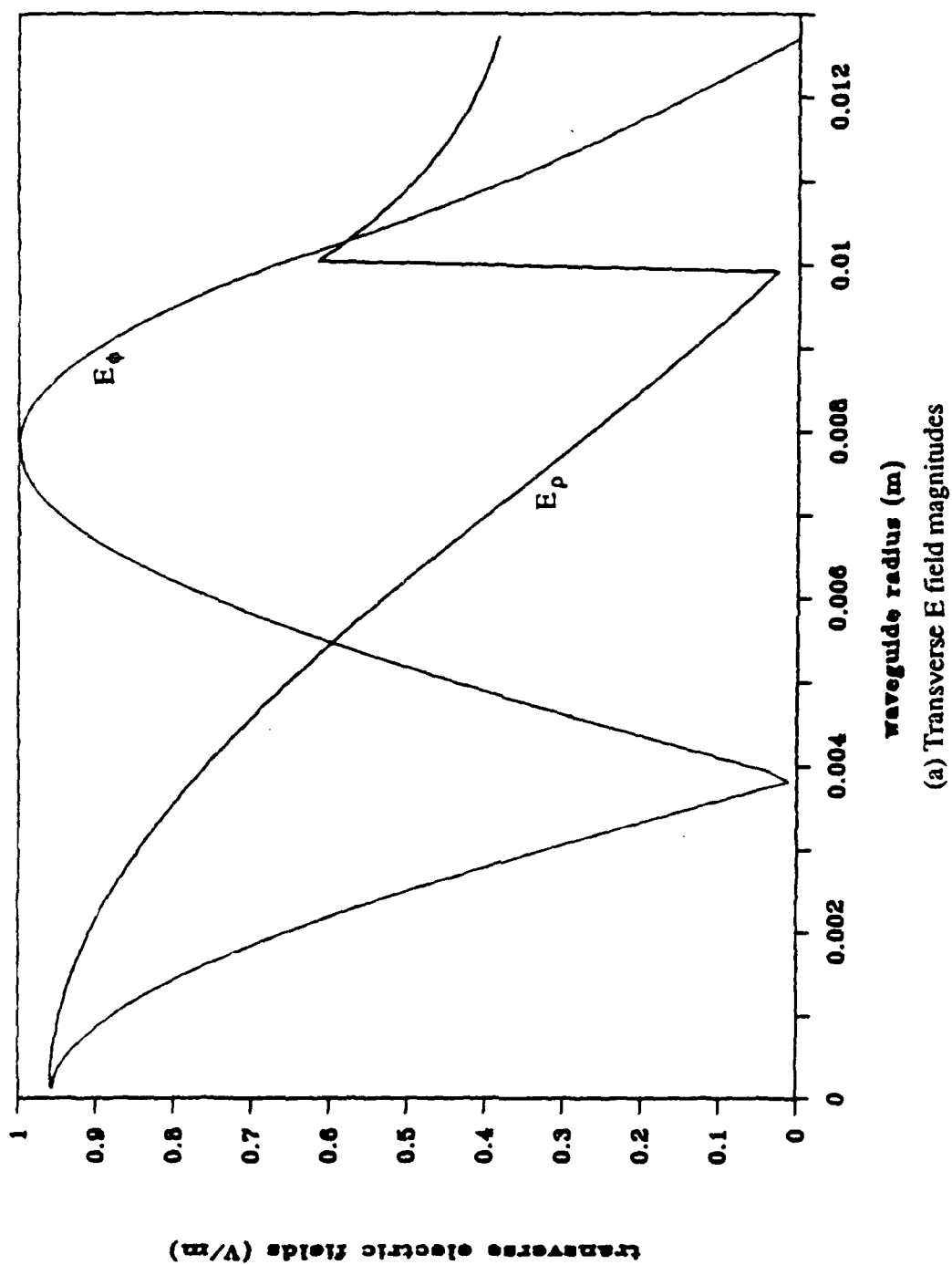


Figure 3.7. Transverse (a) E and, (b) H field magnitudes, for the  $EH_{11}$  mode of the rod-insert waveguide having  $a/b=0.788$ ,  $b=0.5$  in,  $f=4$  GHz,  $\epsilon_{r1} \approx 37.6$  and  $\epsilon_{r2} \approx 1$ .

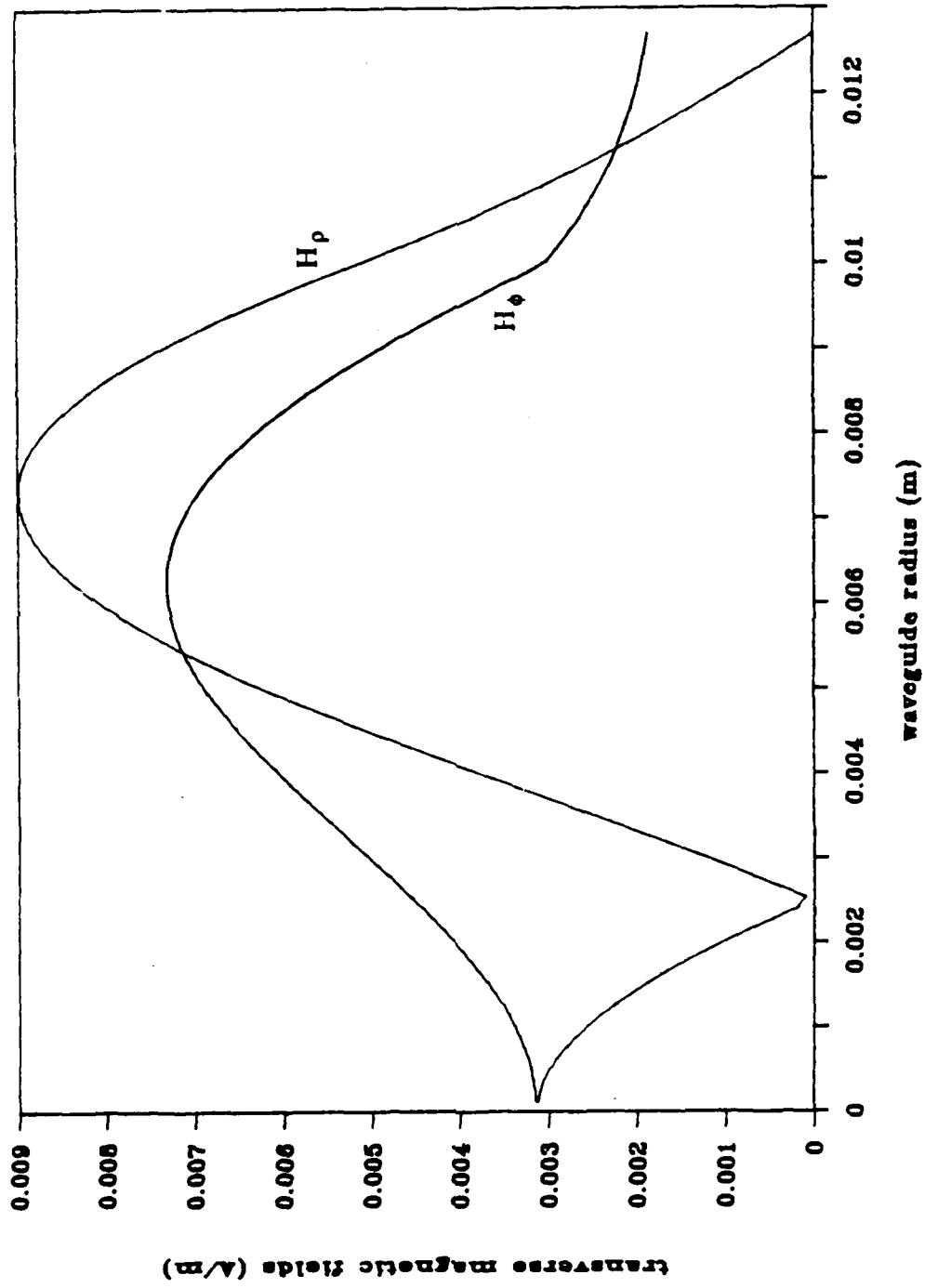


Figure 3.7. (b) Transverse H field magnitudes.

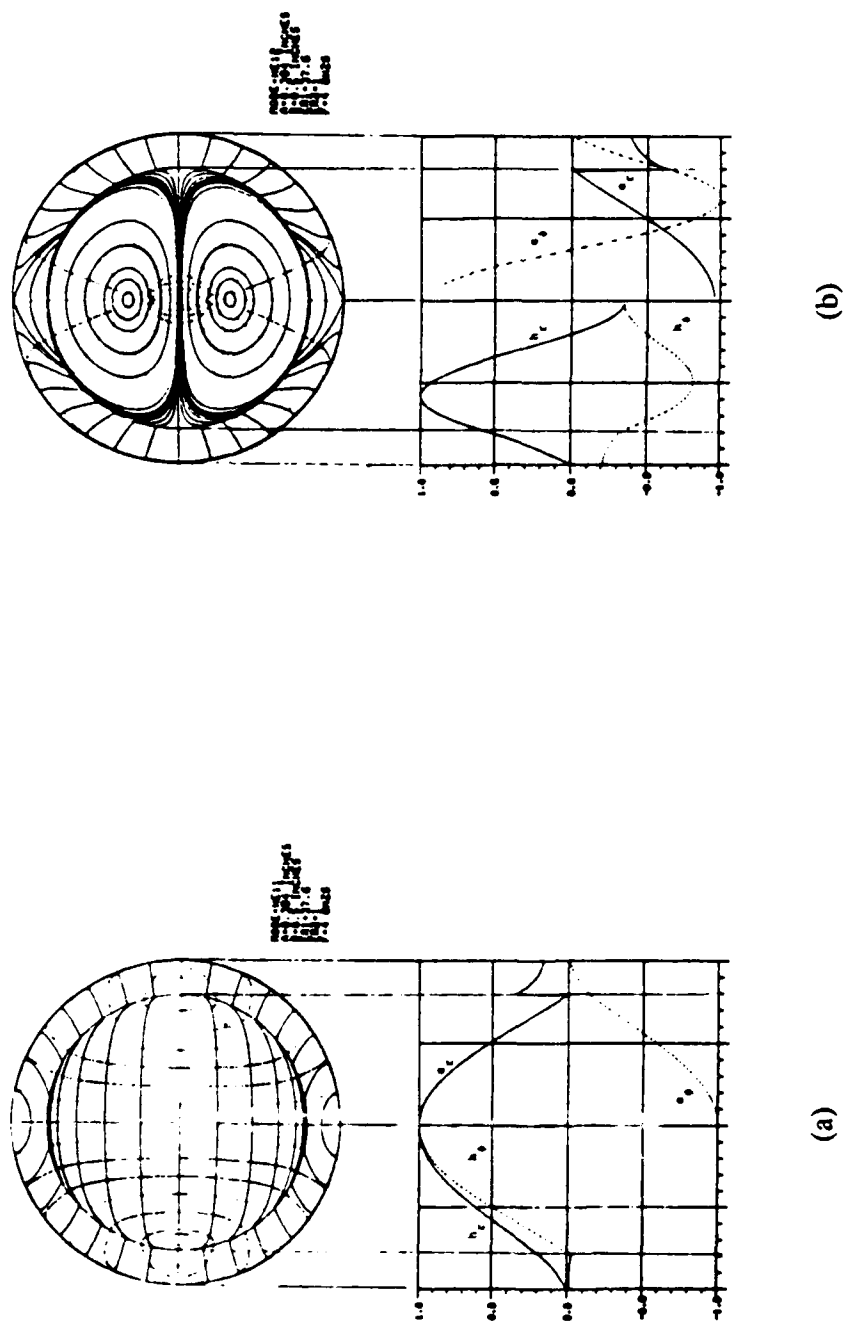


Figure 3.8. Transverse E and H field magnitudes in the rod-insert waveguide for the (a)  $HE_{11}$  mode and, (b)  $EH_{11}$  mode, having  $b=0.5$  in,  $f=4$  GHz,  $\epsilon_r=37.6$  and  $\epsilon_r=1$  [4]. (© 1985 IEEE)

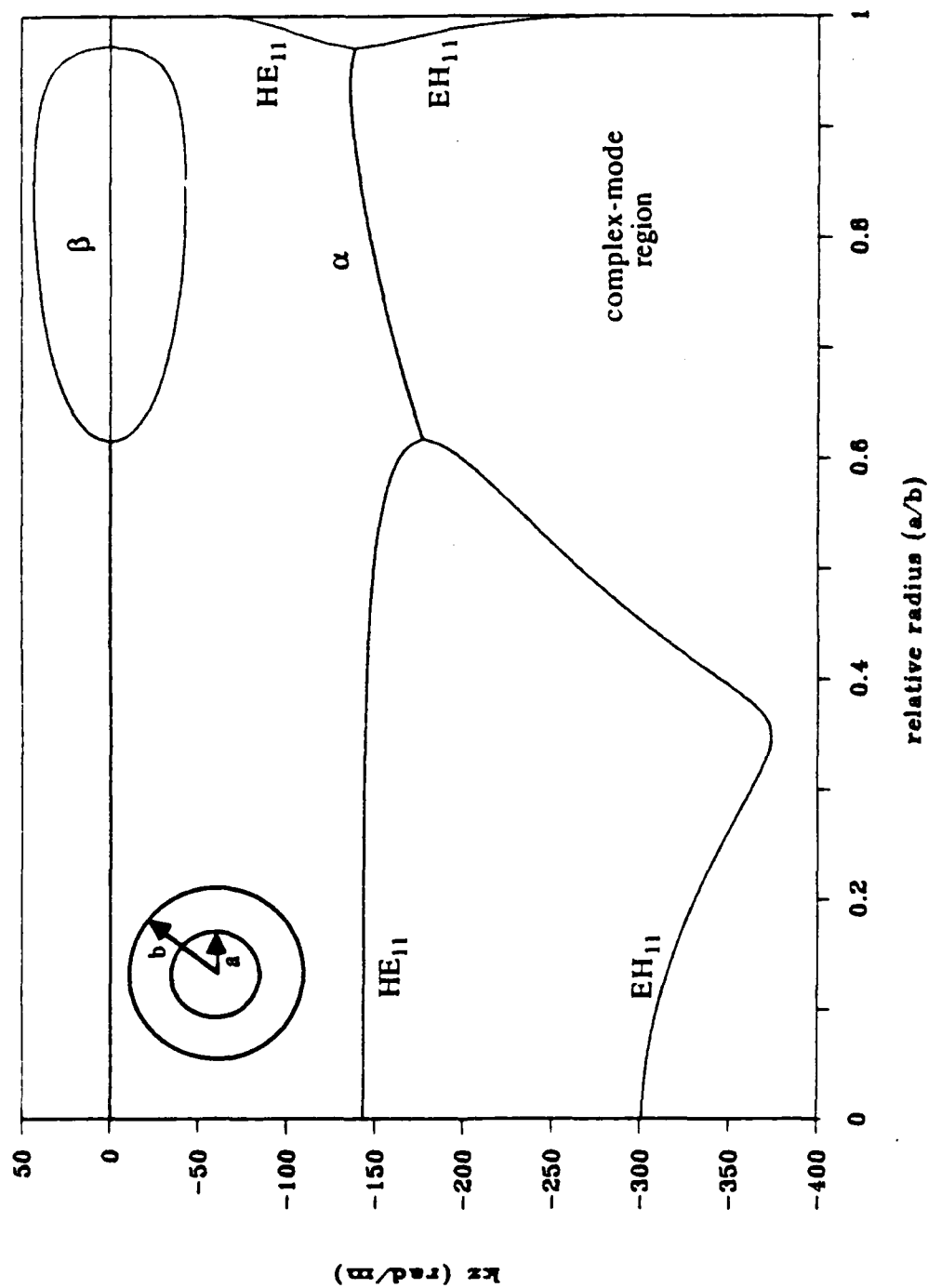


Figure 3.9. Trace of  $k_z$  versus relative rod radius for the  $HE_{11}$  and  $EH_{11}$  modes, including the complex-mode region, in the rod-insert waveguide having  $b=0.5$  in,  $f=1$  GHz,  $\epsilon_{r1}=37.6$  and  $\epsilon_{r2}=1$ .

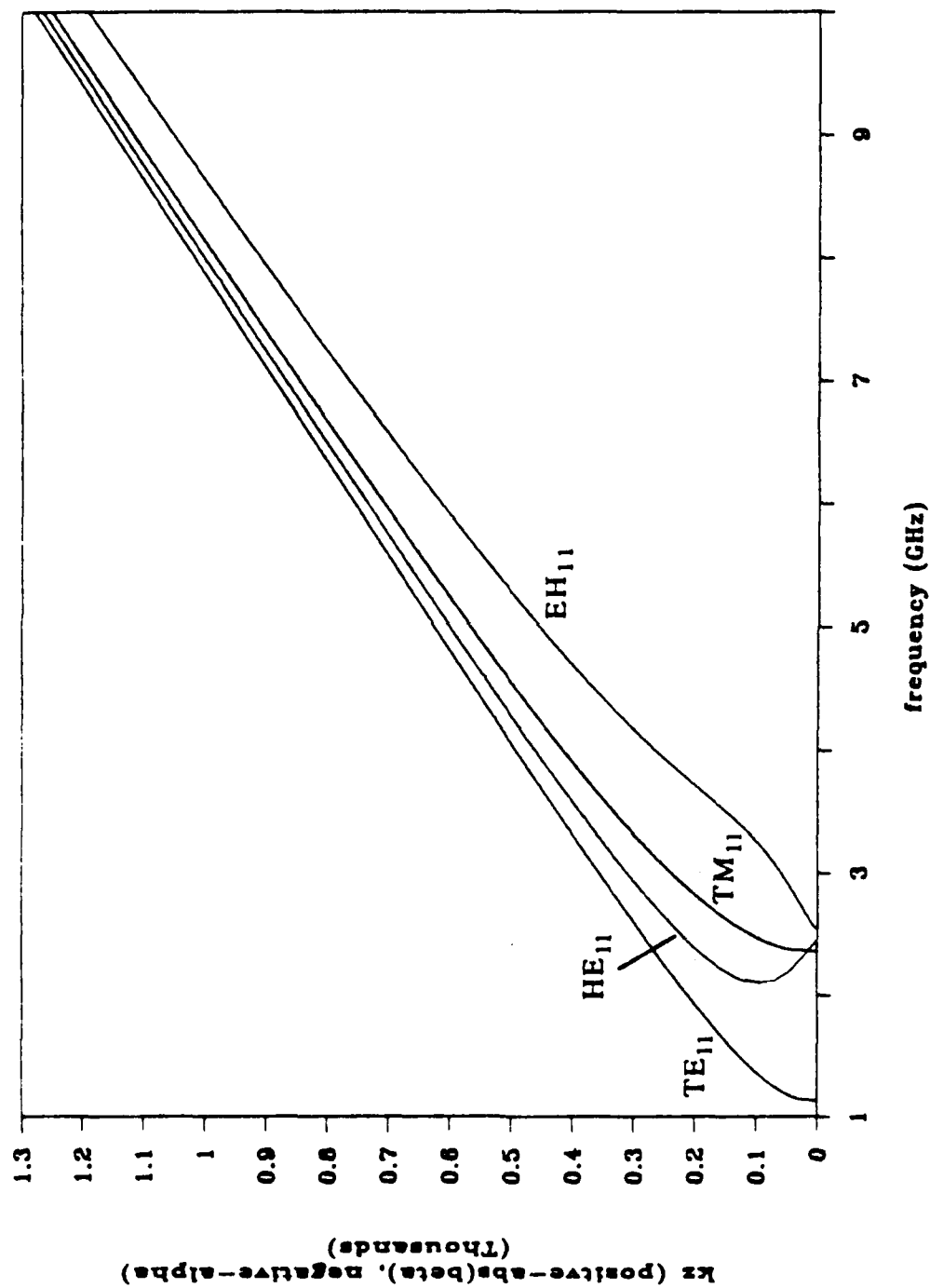


Figure 3.10. The  $\beta$ - $\omega$  curves for both the rod-insert guide having  $a/b=0.788$ ,  $b=0.5$  in,  $\epsilon_{r_1}=37.6$  and  $\epsilon_{r_2}=1$ , and the homogeneous guide of radius 0.5 in and  $\epsilon_r=37.6$ .



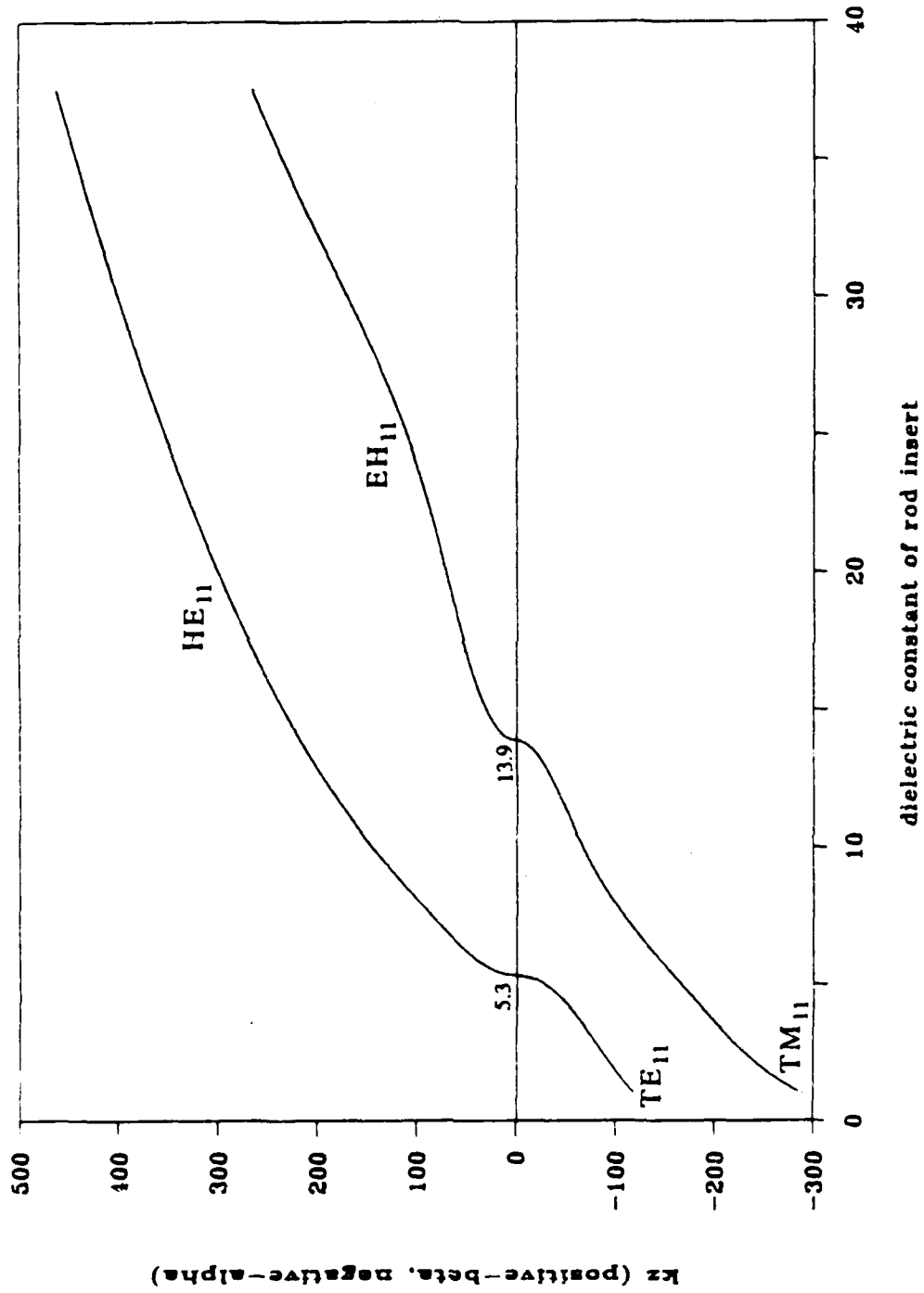
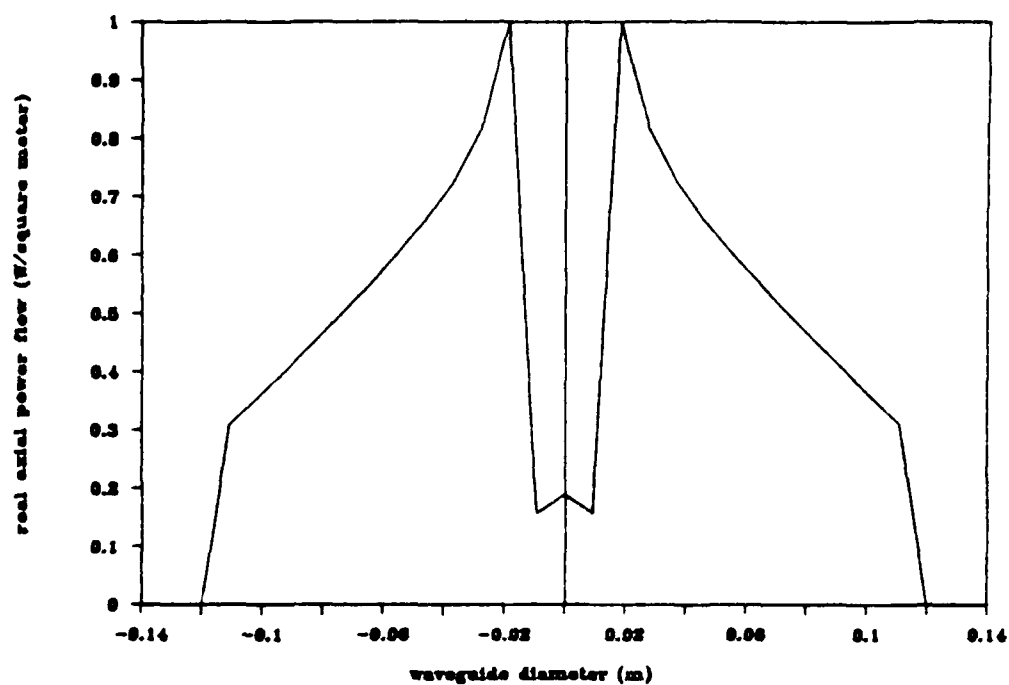
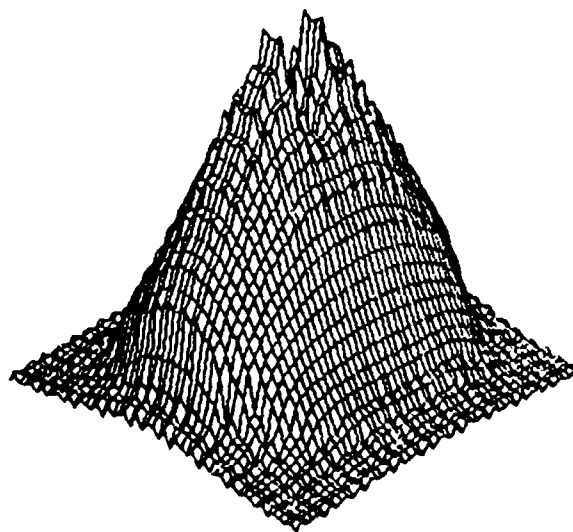


Figure 3.11. Trace of  $k_z$  versus  $\epsilon_r$  for the  $HE_{11}$  and  $EH_{11}$  modes in the rod-insert waveguide having  $a/b=0.788$ ,  $b=0.5$  in,  $\epsilon_{r_2}=1$  and  $f=4$  GHz.

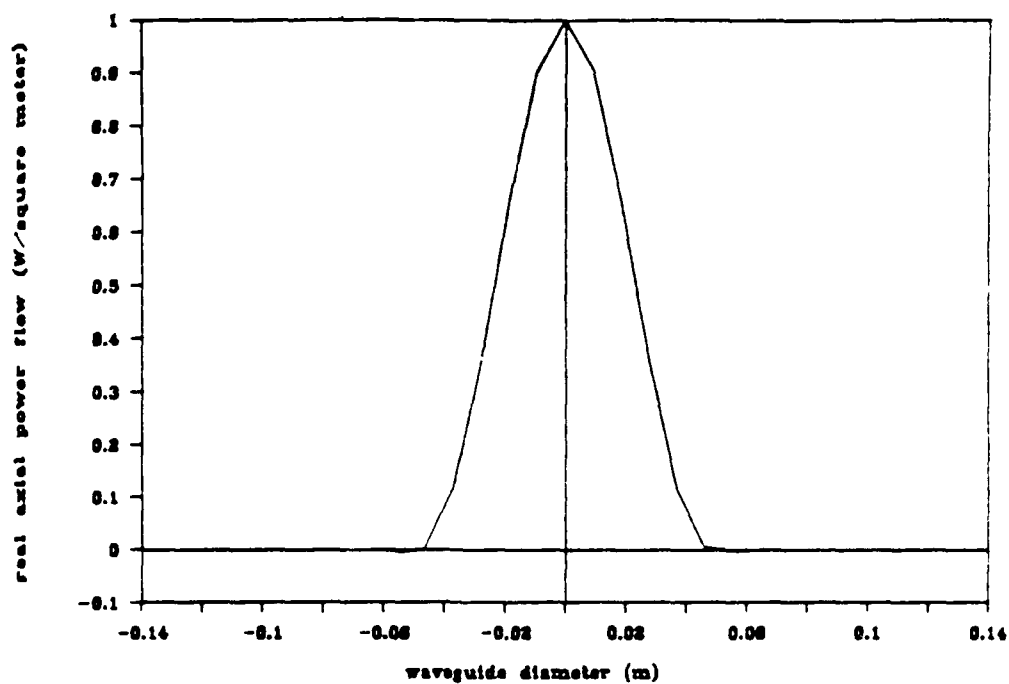


(a)

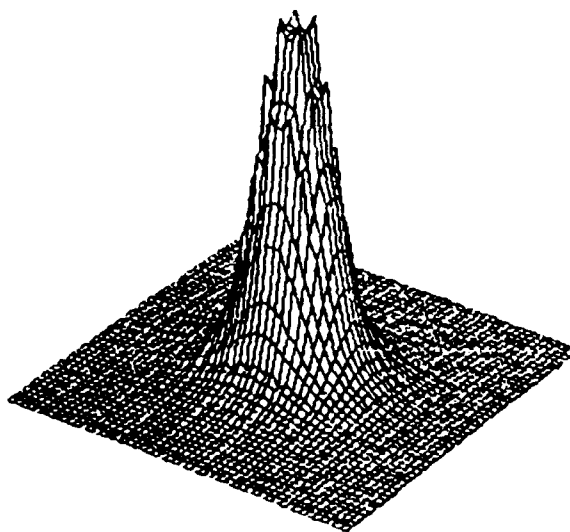


(b)

Figure 3.12. Axial real power flow of the  $HE_{11}$  mode (a) in the  $\phi=0$  plane and, (b) 3-D, for point A in the  $k_z$  trace of Figure 3.3 having  $a/b=0.1$ ,  $b=0.4\lambda$ ,  $f=1$  GHz,  $\epsilon_{r1}=10$  and  $\epsilon_{r2}=1$ .

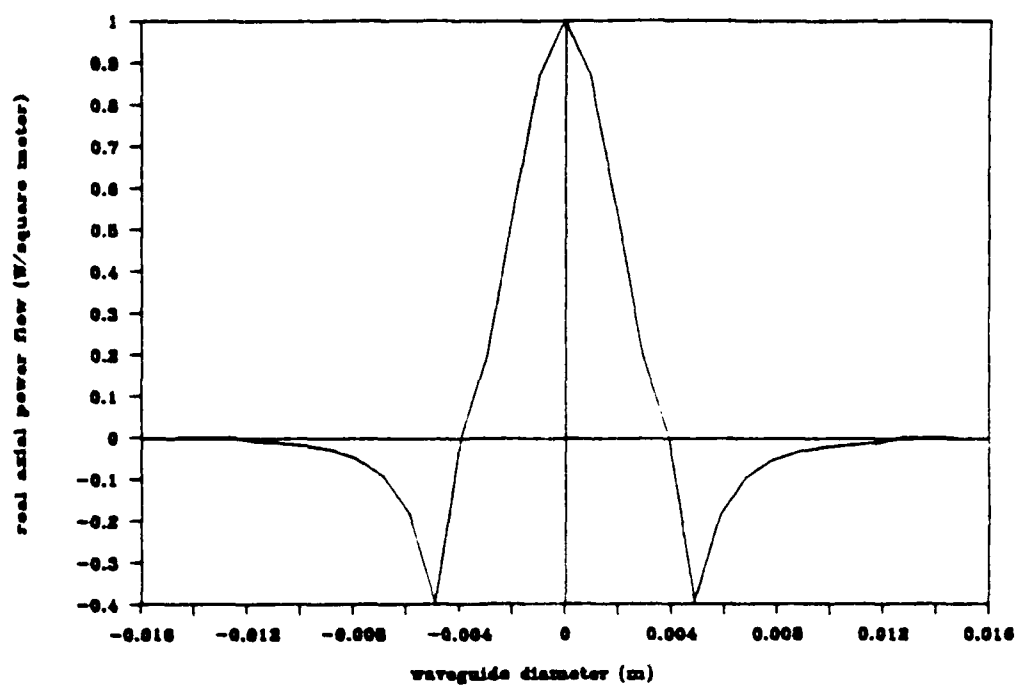


(a)

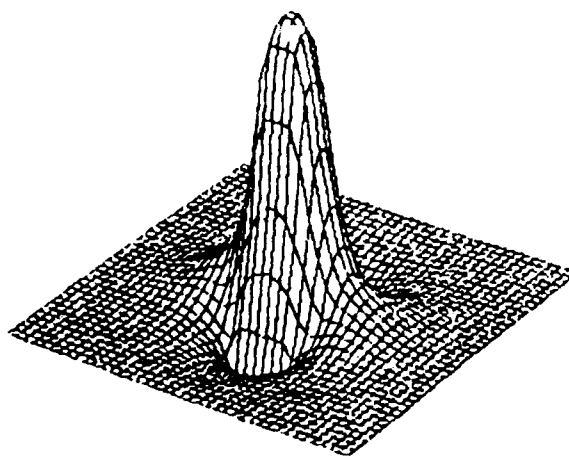


(b)

Figure 3.13. Axial real power flow of the  $HE_{11}$  mode (a) in the  $\phi=0$  plane and, (b) 3-D, for point D in the  $k_z$  trace of Figure 3.3 having  $a/b=0.4$ ,  $b=0.4\lambda$ ,  $f=1$  GHz,  $\epsilon_{r1}=10$  and  $\epsilon_{r2}=1$ .

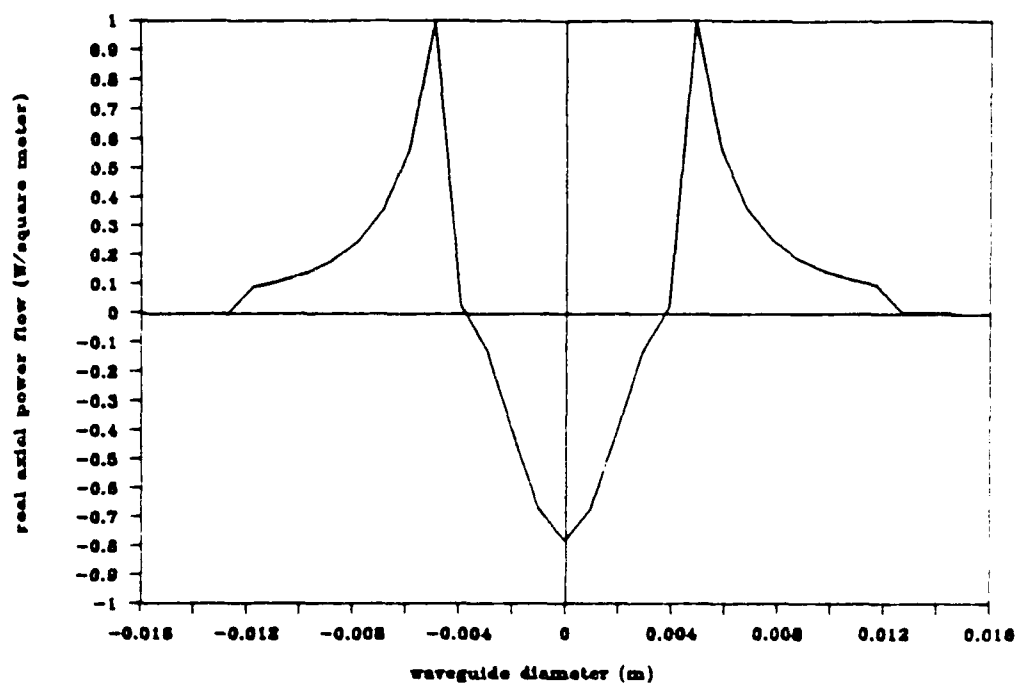


(a)

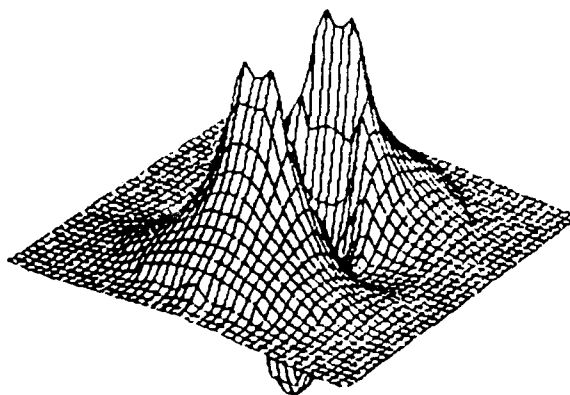


(b)

Figure 3.14. Axial real power flow of the HE<sub>11</sub> mode (a) in the  $\phi=0$  plane and, (b) 3-D, for point C in the  $k_z$  trace of Figure 3.5 having  $a/b=0.36$ ,  $b=0.5$  in,  $f=4$  GHz,  $\epsilon_{r1}=37.6$  and  $\epsilon_{r2}=1$ .

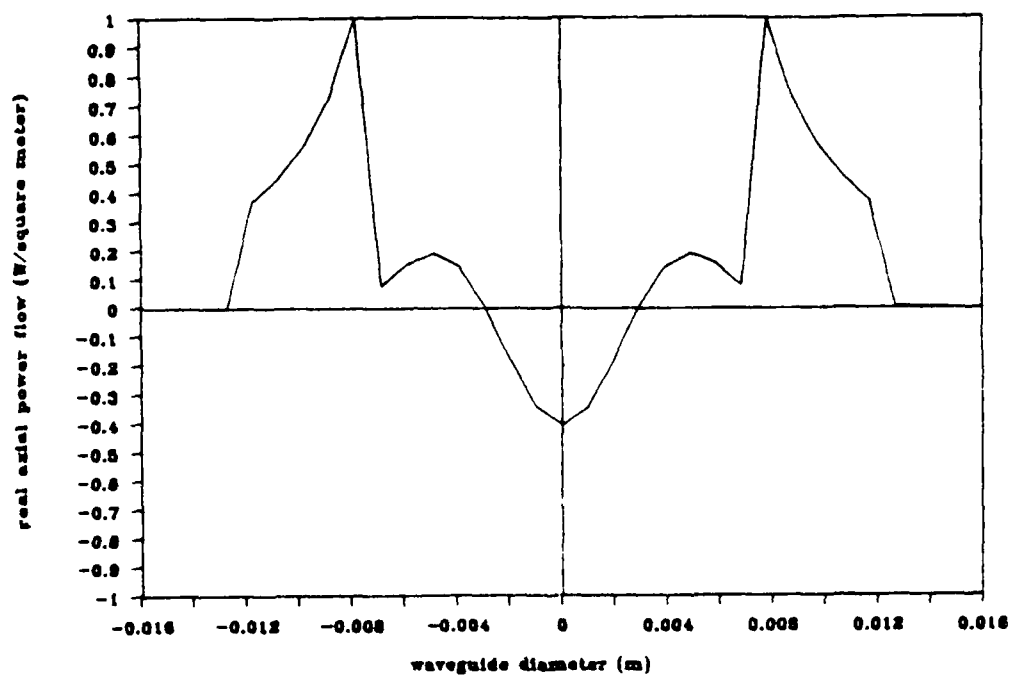


(a)

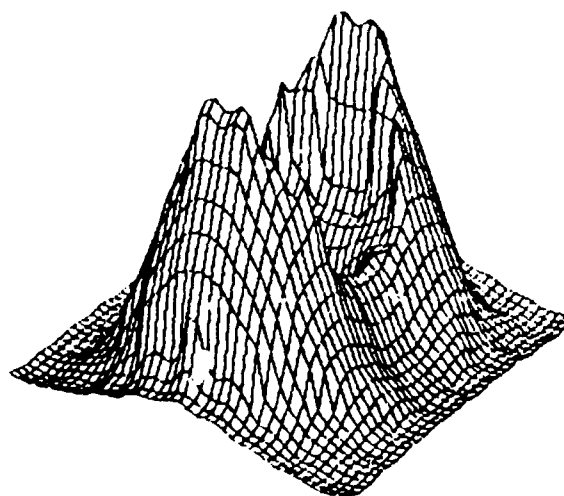


(b)

Figure 3.15. Axial real power flow of the  $EH_{11}$  mode (a) in the  $\phi=0$  plane and. (b) 3-D, for point A in the  $k_z$  trace of Figure 3.5 having  $a/b=0.3646$ ,  $b=0.5$  in,  $f=4$  GHz,  $\epsilon_{r1}=37.6$  and  $\epsilon_{r2}=1$ .



(a)



(b)

Figure 3.16 . Axial real power flow of the  $EH_{11}$  mode (a) in the  $\phi=0$  plane and, (b) 3-D, for  $k_z=70$  in the  $k_z$  trace of Figure 3.5 having  $a/b=0.5815$ ,  $b=0.5$  in,  $f=4$  GHz,  $\epsilon_{r1}=37.6$  and  $\epsilon_{r2}=1$ .

## CHAPTER 4

### INHOMOGENEOUS THREE-LAYERED DIELECTRICALLY- LOADED WAVEGUIDES

The theoretical analysis used to formulate and construct the computer programs for the circular waveguide filled with layered, concentric dielectric media is general enough to find solutions for any number of dielectrics having real or complex constitutive parameters. In the preceding chapter, the cases where two dielectrics filled the waveguide were compared with the previously published work as a verification of the computer codes in addition to investigating the wave behavior for the rod-insert arrangement. In this chapter, the waveguide will be assumed to be filled with three concentric, perhaps lossy, dielectrics. The three-dielectric problem is a reasonable way in which a waveguide-below-cutoff penetration into a shielded enclosure can be modelled when a hose filled with some material is passed through the waveguide, into the shelter. Since the three-dielectric problem is so important, a considerable amount of emphasis will be placed on investigating the wave behavior in such an environment and obtaining representative samples of the key characteristics, such as attenuation.

The amount of attenuation the wave undergoes in the waveguide is the most important characteristic in shielding applications. Hence, the wave attenuation will be calculated as a function of both relative dielectric radius and frequency for varying permittivities. Only losses from the dielectrics will be considered here since the typical waveguides are short (6-12 in) so the metal waveguide wall losses will be relatively small. A very important result, which will be shown in Section 4.3, is that if the dielectric losses increase in the guide, the wave attenuation is not necessarily increased and may actually be decreased! This remarkable finding is due to a redistribution of power flow into less lossy dielectrics, that is not possible in homogeneous waveguides.

Also in this chapter, a new modal designation will be presented for propagating modes in the backward-wave regions. This new designation will be shown to be more consistent with other properties of the wave, such as net power flow and boundedness of the wave. A spinoff from this discussion is an investigation into perhaps a refined definition for the modal cutoff frequency when backward waves are present in the dispersion graph.

#### 4.1 Lossless Three-Dielectric Waveguides

In most applications of the waveguide below cutoff where a fluid is transferred into a shielded enclosure, the waveguide can be modelled as a three-dielectric problem, that is, a hose filled with some material inside an air-filled guide. Theoretical investigations into this arrangement proceed almost identically to those in Chapter 3 for the two-dielectric guide. The computer programs were modified slightly to reflect a hose as the second dielectric by keeping the radius difference between the inner dielectric and that of the hose's outer radius constant as the inner radius is increased in a  $k_z$  versus relative radius plot. An example of the results for the  $k_z$  versus  $a/b$  tracing process in the three-dielectric problem is given in Figure 4.1 for the lossless case. Here a 0.1908 in thick hose of  $\epsilon_r=3$  F/m is increased in diameter inside a 2.005 in radius waveguide at 1 GHz while the permittivity of the filling inside the hose is varied for the  $HE_{11}$  and  $EH_{11}$  modes. All the curves vary smoothly until  $a/b=0.9$  where the outer edge of the hose meets the waveguide wall. For radii greater than this, the hose is gradually "pushed out" of the guide until  $a/b=1$  where the guide becomes homogeneous. This  $a/b=1$  point is a convenient check for the correctness of the mode classification as discussed in Section 3.3. These  $k_z$  versus relative radius plots, in addition to their interpretation as  $k_z$ - $\omega$  plots, can also be viewed as transition diagrams of the axial wavenumber as the guide changes from an inhomogeneous guide of (q-1) dielectrics to a homogeneous guide filled with a material having parameters  $(\mu_{r1}, \epsilon_{r1})$ .



If the permittivity of the hose is increased from 3 to 10 F/m while all other parameters are left unchanged, a new  $k_z$  versus relative radius plot shown in Figure 4.2 results. There is little difference between this plot and the one in Figure 4.1 except when  $\epsilon_{r1}$  reaches 7 F/m where the  $HE_{11}$  and  $EH_{11}$  mode traces form continuous curves. A complex-mode region develops between these two curves from  $a/b \approx 0.5$  to 0.6. Interestingly, a complex-mode region has formed but the propagating backward-wave region usually associated with the complex mode is absent. This has been reported elsewhere [14] and this graph provides additional verification of the phenomenon when more than two dielectrics fill the guide.

The  $EH_{11}$  modes in both figures contain regions of negative slope indicative of a backward-wave evanescent mode. Two of these regions exist bracketed by forward-wave evanescent mode regions. Although purely evanescent here, the introduction of losses will impart propagating-wave behavior onto the fields and the amount of attenuation in these modes will then become important. The  $HE_{11}$  modes do not exhibit this backward-wave behavior in the evanescent region, but in Figure 4.2, for  $a/b$  greater than approximately 0.9, propagating backward waves are evident. (An exception to this is when  $\epsilon_{r1} = 2$  F/m and  $a/b > 0.9$ , when the  $HE_{11}$  mode does have a slight negative slope.)

When the permittivity of the innermost dielectric is made larger than approximately 10 F/m, the tracing process for the  $k_z$  versus relative radius plots becomes complicated by the interactions of modes with the same azimuthal variation but differing radially. Figures 4.3 through 4.6 form a series of graphs pictorially depicting these interactions in the same waveguide arrangement as above, but  $\epsilon_{r1}$  ranging from 10 to 30 F/m. Both the HE and EH modes with unity azimuthal variation are shown for the radial variations 1, 2 and 3. As  $\epsilon_{r1}$  increases, a few mode traces break closed contours with other modes and form smooth traces which cover the entire  $a/b$  range as with the  $HE_{11}$  and  $EH_{11}$  modes in Figures 4.3 and 4.4. Conversely, some modes that were smooth across the entire range form closed contours, as with the  $HE_{12}$  and  $EH_{12}$  modes. Where the slope becomes infinite in any of

these traces, complex modes begin and continue with increasing  $a/b$  until either a proper evanescent or propagating mode is reached. (For clarity, the complex modes are not indicated in these plots and only purely propagating or evanescent modes are shown.)

A difficulty arises in Figure 4.5 where it is not obvious how the  $EH_{11}$  mode can begin at  $a/b=0$ , and then end as a  $TM_{12}$  mode at  $a/b=1$ . Physically this is not possible, since by the definition of the mode, the number of  $\rho$  variations is a constant integer. A similar situation occurs for this mode in Figure 4.4 for a smaller  $\epsilon_{r1}$ , but the transition occurs between two infinite slope regions characteristic of the complex modes. It is the  $HE_{12}/EH_{12}$  and  $HE_{12}/EH_{11}$  coupled complex modes which provide the vehicle for smooth mode traces across the entire range of  $a/b$ . Reasoning similar to this explains how the mode transition from  $EH_{11}$  at  $a/b=0$  to  $TM_{12}$  at  $a/b=1$  can take place in Figure 4.5 since it is these same complex modes which are providing the bridge for transition from one trace to another. This reasoning is further justified by Figure 4.7 where the complex modes are now included in the figure. The axial wavenumbers for each mode should, and can, be traced by a smooth curve across the entire range of increasing relative dielectric radius. However, as shown here, some complex modes must be included occasionally to allow for these smooth transitions. Without them, seemingly nonphysical traces can result which are difficult to explain as was seen in Figure 4.5.

By increasing  $\epsilon_{r1}$  further to 30 F/m the traces in Figure 4.6 emerge. The complexity in the interactions among the various modes increases a great deal in this graph from the previous examples. The  $HE_{12}/EH_{12}$  closed contour in the previous graph has separated and now the  $HE_{13}$  and  $EH_{12}$  modes form closed contours in addition to the  $HE_{11}/EH_{11}$  modes. Without graphing these traces in this figure and those in the past three, it would be difficult to properly identify some segments in the traces of this figure, such as the segment S. However, by examining the other traces and observing the progression with increasing  $\epsilon_{r1}$  (which can be thought of as "pegging" the left-hand side of the traces and slowly increasing the right-hand edge) this segment can be identified as an  $HE_{13}$  mode

trace. Although the mode is evanescent in this region, for lossy materials, this mode and those nearby in the graph will propagate with some large amount of attenuation. Knowledge of the behavior of these lower-order modes is important even though they are evanescent in the lossless case.

## 4.2 Complex and Backward-Wave Modes

The question arises as to what mode the backward-wave region in Figure 4.5 (which includes the point A) should be named. Following the past work of Clarricoats and Waldron [9], [13], this region would be designated the  $HE_{11}$  mode—in particular, a "paranormal sub-mode" in keeping with Waldron's denotation [31]. This idea seems reasonable since as the permittivity of the loading dielectrics is increased, the  $HE_{11}$  mode's  $\beta$ - $\omega$  curve gradually changes from that of a homogeneous guide to one containing a backward-wave region for the inhomogeneous case as in Figure 3.10 and [13]. Waldron, among others, expresses the belief that the whole curve belongs to the  $HE_{11}$  mode, but in the region below cutoff, in the backward-wave area,  $k_z$  is double-valued for this mode, so that the  $EH_{11}$  mode apparently "disappears" for the range of values where the backward-wave region exists. It will be worthwhile at this point to investigate whether or not this is a correct assessment.

The wavenumbers and  $(C_{11}, C_{13})$  coefficients for a number of points labelled in Figure 4.5 of the  $HE_{11}$  and  $EH_{11}$  modes in the propagating region are listed in Table 4.1. In order to choose the correct  $k_z$  root for these points and especially point A, a small amount of loss is added to the dielectrics ( $\epsilon_{r1}=20-j0.5$ ,  $\epsilon_{r2}=3-j0.1$  F/m). From the table, it is apparent that the sign of the real part of  $C_{13}$  for point A agrees with points B, C and D, all of which belong to the  $EH_{11}$  mode trace. In keeping with Snitzer's scheme (cf. Section 2.5), the backward-wave region is labelled  $EH_{11}$ . If on the other hand, the root  $k_z$  for point A had been chosen on the other branch, which for the backward wave is  $k_z=9.3+j1.5$

rad/m, the new  $C_{13}$  coefficient would be  $40.4+j1.1$ . The sign of the real part of this coefficient would then agree with the  $HE_{11}$  mode but the net power flow would be negative. Since the net power flow is to be away from the source, the first root is the correct one (it also has positive net power flow) and the backward-wave region is rightly labelled an  $EH_{11}$  mode and nowhere in the  $k_z$  trace does the  $EH_{11}$  mode disappear. This idea was illustrated earlier in Section 3.5 for the two-dielectric guide in reference to the sign of the net power flow. Depending on which branch  $k_z$  was chosen to be on, the 3-D transverse power flow plot appeared similar to either the  $HE_{11}$  or  $EH_{11}$  mode graphs from other points on the dispersion plots. The correct choice was made by examining the type of wave propagation present (either forward augmented or backward augmented) in addition to the sign of the net power flow.

An argument against this type of modal designation is that the  $HE_{11}$  mode does not appear to have a cutoff frequency which is not to be expected for a propagating mode. In the usual lossless case, the cutoff frequency is defined by  $k_z=0$ . From the separation relation (2.12), the phase velocity,  $v_p = \frac{\omega}{\beta}$ , is then infinite and the group velocity,  $v_g = \frac{\partial \omega}{\partial \beta}$ , is zero at cutoff. Since the group velocity can be a measure of energy velocity under the appropriate conditions, the criterion of  $v_g=0$  may be more fundamental than  $v_p=\infty$  for defining the cutoff frequency. In Figure 4.7 for example, the  $HE_{11}$  mode has  $v_g=0$  but  $v_p \neq 0$  at  $a/b=0.48$  where the slope becomes infinite. This point could represent a cutoff frequency of the two coupled complex modes as  $a/b$  increases and the *cutoff* frequency of two other modes, the forward-wave  $HE_{11}$  and the backward-wave  $EH_{11}$ .

The plausibility of such a notion as defining the cutoff frequency by  $v_g=0$  and not necessarily with  $v_p=\infty$  can be investigated simply by considering the separation relation in the definition of  $v_g$  as

$$\frac{1}{v_g} = \frac{\partial \beta}{\partial \omega} = \frac{\partial}{\partial \omega} \text{Re}\{k_z\} = \text{Re}\left\{ \frac{\partial k_z}{\partial \omega} \right\} . \quad (4.1)$$

After some manipulation and noting that  $\text{Re}\{z\} = \frac{z+z^*}{2}$

$$\frac{\partial \omega}{\partial \beta} = \frac{4|k_z|^2}{2\omega\mu_i\epsilon_i(k_z+k_z^*) - k_z^* \frac{\partial k_{p_i}^2}{\partial \omega} - k_z \left( \frac{\partial k_{p_i}^2}{\partial \omega} \right)^*} \quad (4.2)$$

By defining the cutoff frequency as

$$\lim_{\omega \rightarrow \omega_c} \frac{\partial \omega}{\partial \beta} = 0 \quad (4.3)$$

(4.3) is satisfied, by considering (4.2), in the two cases when

(i)

$$\begin{aligned} |k_z|^2 = 0 & \Rightarrow \beta^2 = -\alpha^2 \\ & \Rightarrow \beta = \alpha = 0 \text{ for } \alpha, \beta \text{ real} \end{aligned} \quad (4.4)$$

and

(ii)

$$\lim_{\omega \rightarrow \omega_c} \left[ k_z^* \frac{\partial k_{p_i}^2}{\partial \omega} + k_z \left( \frac{\partial k_{p_i}^2}{\partial \omega} \right)^* \right] \rightarrow \infty \quad (4.5)$$

Equation (4.4) is the usual definition for the cutoff frequency,  $k_z=0$ . Equation (4.5), however, is a new relation valid only in dispersive situations, since for a homogeneous guide,  $k_p$  is a constant depending only on the "electrical diameter" of the waveguide. Therefore, in a *homogeneous* guide, (4.5) will never be satisfied. The  $k_{p_i}$  becomes

frequency dependent in the inhomogeneous guide because  $k_z$  is now the known variable from which  $k_{pi}$  is calculated and not the other way around as in the homogeneous guide. Clearly,  $k_z$  is frequency dependent as any  $k_z$ - $\omega$  plot of the inhomogeneous guide will attest. In an inhomogeneous guide, (4.5) will be satisfied and  $v_g=0$  whenever  $\frac{\partial k_z}{\partial \omega} = \infty$ . Although this was known beforehand, Equation (4.2) lends some insight into why an alternative definition of the cutoff frequency is necessary in the inhomogeneous waveguide. In this light then, the homogeneous guide criterion for cutoff,  $v_g=0$  and  $v_p=\infty$ , is a special case of the more general situation where cutoff is defined by  $v_g=0$  and  $v_p \neq \infty$  in the inhomogeneous guide.

Additional confirmation for this method of naming the backward-wave modes is provided by the graphs in Figures 4.8 through 4.11. Here the  $HE_{11}$  and  $EH_{11}$  mode plots are given for the three-dielectric inhomogeneity with a small amount of loss as  $\epsilon_{r1}'$  is varied from 10 to 30 and  $\epsilon_{r1}''=0.5$  F/m for  $\epsilon_{r1}=\epsilon_{r1}'-j\epsilon_{r1}''$ . The physical parameters used to generate these graphs are the same as before except for the hose, which has a new thickness of 0.2 in, that will also be used in the next section for attenuation calculations in the three-dielectric lossy guide. This thickness is close enough to the previous one of 0.1908 in for an accurate comparison. All these plots illustrate the splitting of the complex modes with the introduction of loss into the dielectrics. In Figure 4.8, the modes progress smoothly from evanescent to complex and then either to propagating for  $HE_{11}$  or back to mostly evanescent for the  $EH_{11}$  mode. No propagating backward wave is encountered by these two modes. In the complex-mode region, the  $HE_{11}$  mode is an augmented backward wave while the  $EH_{11}$  is an attenuated forward wave. The introduction of loss produces some phase difference between the two complex waves such that nonzero net power flow is possible.

The appearance of the backward-wave region begins in Figure 4.9 for  $\epsilon_{r1}=15-j0.5$  F/m. The  $EH_{11}$  mode becomes backward augmented here in contrast to the previous figure

when the  $HE_{11}$  mode was. Indeed, the backward-wave region in Figure 4.9 has  $\beta$  negative as previously predicted. This appears even more reasonable here since a smooth trace for  $\beta$ , from a negative value in the complex-mode region for conservation of energy reasons (in the limit as the losses go to zero), to the positive values for forward propagation, is provided by negative values of  $\beta$  in the backward-wave region. Figures 4.10 and 4.11 contain plots displaying similar behavior for  $\epsilon_{r1}=20-j0.5$  and  $\epsilon_{r1}=30-j0.5$  F/m, respectively.

In the Figures 4.8 through 4.11, the backward-wave propagating region only appears when the  $EH_{11}$  mode changed from evanescent to propagating as  $a/b$  is varied from zero to one. As was mentioned in Section 3.3, if anywhere in the  $k_z$  trace there exists propagating backward waves, this necessarily implies that somewhere else in the trace complex modes exist. Considering these traces then, it is evident that the backward-wave region is needed to preserve the continuity in the  $\beta$  trace and assure that conservation of energy is satisfied in addition to the boundedness of the wave. In summary of this, under certain conditions, complex-wave regions in the  $k_z$  trace can exist without backward-wave regions appearing. However, if backward-wave regions do exist, somewhere in the trace complex modes form since there is no other way for the mode to end as evanescent, for decreasing  $a/b$ , and still preserve continuity in the  $k_z$  trace.

One very curious phenomenon apparent in the plots having a backward-wave region is the metamorphosis of the modes, as  $a/b$  is increased, from either evanescent  $HE_{11}$  or  $EH_{11}$  modes, to not propagating  $HE_{11}$  and  $EH_{11}$  modes as would be expected, but rather to propagating  $EH_{11}$  or  $HE_{11}$  modes, respectively. This behavior is not witnessed in Figure 4.8 where there is no propagating backward-wave region. As an example of this, starting with the  $HE_{11}$  mode at  $k_z \approx -j27$  rad/m in Figure 4.9, as  $a/b$  is increased from zero to one, the mode is first evanescent  $HE_{11}$ , then backward augmented in the complex-mode region. The mode next becomes a propagating backward  $EH_{11}$  mode and finally a forward propagating and attenuated  $EH_{11}$ . The gradual change from an  $HE_{11}$ -like to an  $EH_{11}$ -like

mode is clearly evident in this example. In this line of thought then, naming the backward-wave region  $EH_{11}$  may seem up to the designator and not really dependent on any physical reasoning. However, in addition to the material already presented in support of naming this mode  $EH_{11}$ , this trace clearly has propagating behavior exclusively associated with the  $EH_{11}$  mode, whereas the  $HE_{11}$  mode is cut off on this trace. The  $HE_{11}$  mode displays propagating behavior only on the other trace which begins an evanescent  $EH_{11}$  in Figure 4.9 and ends a propagating  $HE_{11}$  mode.

Another curiosity, which will be mentioned in passing, is the  $EH_{11}$  trace in Figure 4.10. In Figures 4.9 and 4.11, the  $EH_{11}$  trace is "bent" as it passes from  $\beta$  negative to positive with the associated bulge in  $\alpha$ . In the lossless cases, as in Figures 4.4 and 4.6, this bulge provides the transition from a backward propagating  $EH_{11}$  mode to a forward propagating  $EH_{11}$  mode without  $v_g$  becoming infinite, which would not be physical. When this type of behavior in the  $EH_{11}$  mode is observed, as in Figure 4.10, it has been reported by Waldron [13] that a maximum backward-wave region has been attained. For all other values of  $\epsilon_{ri}$ , with  $i=1,\dots,q$ , the bulge will be smaller as evidenced by the plots in Figures 4.9 and 4.11. This phenomenon has been previously associated with the  $HE_{11}/EH_{11}$  degeneracy at the point where  $\beta=0$  as in Figure 4.10 [10], [13]. From the work that has been presented here, the mode is better named  $EH_{11}$ , so there is no mode degeneracy as both the backward- and forward-wave regions are  $EH_{11}$ . This is certainly only a modal nomenclature and in no way is meant to invalidate the results of the previous authors. The material presented in this section and in the preparatory ones is meant simply to report a new way to name the backward-wave region that is more consistent with other properties of the wave and modal designations.



### 4.3 Attenuation in Lossy Three-Dielectric Waveguides

The most important characteristic in this study of the three-dielectric waveguide is the attenuation afforded by dielectric losses above cutoff. Once the modes have been properly identified, the losses for a particular mode can be calculated as a function of relative radius or frequency with the loading dielectric's  $\epsilon_r$  as the parameter. The physical dimensions of the waveguide and hose, for these theoretical calculations, were chosen as representative of a typical application for the waveguide-below-cutoff penetration in a shielded enclosure discussed in Chapter 1. A 4 in waveguide of inner radius 2.005 in was chosen and a 1 in hose of inner radius 0.4909 in and thickness 0.2 in will enclose the filling material in the center.

The  $\epsilon_r$  of the hose was selected by consideration of the traces in Figure 4.12. Here,  $\alpha$  is plotted against frequency for the  $HE_{11}$  mode inside the 4 in waveguide with the 1 in hose filled with a three-point dispersive methanol having values given in Section 5.4. The parameter that is varied among these plots is the loss in the hose. A value of  $\epsilon_{r_2}' = 2.7$  F/m was chosen from listings of values for rubber derivatives in von Hippel [22]. From the traces in Figure 4.12, a value of  $\epsilon_{r_2}'' = 2$  F/m was selected since this value placed the  $\alpha$ - $\omega$  trace in with a "family" of traces with higher  $\epsilon_r''$ 's.

It appears from this graph quite strange that more hose loss causes less wave attenuation. The reason this occurs is as  $\epsilon_{r_2}''$  increases, the power flow is "expelled" from the inner two dielectrics and out to the third, where there is no loss and the wave is attenuated less. If the guide walls were lossy, this effect would be less pronounced; however, in this study, the guide is very short so the wall losses will be negligible compared to the dielectric losses. In this section then, the attenuation afforded by dielectric losses will be calculated using a value of  $\epsilon_{r_2} = 2.7 - j2$  F/m for the hose and all the permittivities of the dielectrics inside the guide assumed to be independent of frequency.

The modes that will be considered for these attenuation plots are the three lowest-ordered nonazimuthally symmetric modes—the  $HE_{11}$ ,  $EH_{11}$  and  $HE_{21}$ . Figures 4.13 through 4.18 contain traces of  $\alpha$  versus  $a/b$  for these three modes with  $\epsilon_{r1}' = 2$  and 10 F/m. These two values were chosen heuristically and yield enough disparity to discern trends in the attenuation as various parameters are changed. For each  $\epsilon_{r1}'$  value, five  $\epsilon_{r1}''$  values (1, 3, 5, 7 and 10 F/m) were chosen as parameters for the loss. (Although these plots give  $\alpha$  in Np/m, conversion to dB/m is possible by multiplying  $\alpha$  by  $8.6859 = 20 \log_{10}(e)$ .) Probably the most noticeable characteristic of these plots is that a higher  $\epsilon_{r1}''$  value does not necessarily imply more loss as would be the case in a homogeneous guide. These graphs clearly show that the relative amount of attenuation between two lossy filling materials is not only a function of the dielectric loss but also on how large the inner diameter of the pipe is in relation to the sheath size. A specific example of this is in Figure 4.13 with  $a/b=0.6$ . At point A,  $k_z=11.1-j14.1$  for  $\epsilon_{r1}=2-j10$ , and at point B,  $k_z=3.7-j24$  rad/m for  $\epsilon_{r1}=2-j1$  F/m. More attenuation is provided by the  $\epsilon_{r1}=2-j1$  F/m dielectric than by the other. This relation reverses itself as the guide becomes homogeneous, as it should, since in this case a higher  $\epsilon_{r1}''$  implies higher attenuation from dielectric losses [20]. Although only the  $HE_{11}$  mode was considered in more detail here, all of these modes in Figures 4.13 through 4.18 contain elements of the same basic behavior.

Another common characteristic among these modes is the existence of a region from  $a/b=0$  to some point nearby where all traces have approximately the same values for  $\alpha$ , after which the traces separate. This region is the cutoff region where the modes are propagating only slightly but are highly attenuated. The wave impedance in this region is mostly reactive and the attenuation is primarily caused by the wavelength of the excitation field being too large to create transverse standing waves in the waveguide. Beyond this cutoff region, the attenuation is due to losses in the loading dielectrics. In a lossless guide, this transition is abrupt and the cutoff frequency is prominent at  $k_z=0$ . When losses are

present, the cutoff becomes "smeared" somewhat and it becomes difficult to locate the specific point of cutoff.

The other range against which the attenuation will be plotted is frequency. Figures 4.19 through 4.24 contain plots of  $\alpha$  versus frequency for the same physical arrangement as in the previous  $\alpha$  versus  $a/b$  plots—specifically, the 1 in hose of  $\epsilon_{r2}=2.7-j2$  F/m in the 4 in guide. The  $\epsilon_{r1}$  values used as parameters are the same for this graph series as in the previous, which are listed on the plots. The frequency band is slightly different for each mode and was selected as a good example of attenuation near the cutin for each mode.

A common characteristic throughout these plots, and also very similar to the  $\alpha$  versus  $a/b$  plots, is that the relative amount of attenuation between two  $\epsilon_{r1}$  values with similar physical dimensions is dependent not only on the sizes of the  $\epsilon_{r1}$ 's but also on the frequency. This is equivalent to the conclusion reached with the  $\alpha$  versus  $a/b$  plots provided  $\epsilon_r$  is not a function of frequency, which it is not here. A similar statement can be made for the relation between  $\epsilon_{r1}$  and the amount of attenuation: a larger  $\epsilon_{r1}$  does not automatically imply higher attenuation for all frequencies in these inhomogeneous guides.

An interesting phenomenon displayed in Figures 4.19, 4.20 and 4.22 is that the largest amount of attenuation is obtained by the smallest  $\epsilon_{r1}$  value. That is, for  $\epsilon_{r1}=1$  F/m, much more attenuation is realized at higher frequencies than for a larger  $\epsilon_{r1}$ . The reason for this was discussed earlier in conjunction with Figure 4.12, where for the lower  $\epsilon_{r1}$  value the power flow is concentrated primarily in the inner dielectric and moves primarily to the outermost dielectric for larger  $\epsilon_{r1}$  values where there is no loss. This redistribution of power flow is marked by the magnitudes and phases of the radial wavenumbers in the dielectrics. As discussed earlier in Section 3.5, the axial power flow concentrates in the dielectric with a higher real radial wavenumber. With losses present, the  $k_{\rho i}$ 's are, in general, neither purely real nor purely imaginary. Instead, the axial power flow concentrates in the dielectric having a  $k_{\rho i}$  that is large and has a real part that is much larger than its imaginary part.

#### 4.4 Power Flow in Lossy Three-Dielectric Waveguides

It was pointed out in the last section that the amount of loss present in the loading dielectrics can have a very large effect on the power-flow distribution in the inhomogeneous guide. This redistribution can greatly change the amount of attenuation the wave will undergo when the dielectrics within the guide have largely differing permittivities. The effect that the losses in the dielectrics have on the power flow and wave attenuation can be quite pronounced depending on the many factors mentioned in the previous section, including the relative radius of the inner dielectrics in relation to the sheath diameter. A good example of this can be illustrated by considering the four cases marked in Figure 4.13. The percentages of the total absolute real power flow in each dielectric are listed in Table 4.2. At  $a/b=0.6$ , the power flow is distributed in roughly a similar manner for both cases A and B having  $\epsilon_{r1}=2-j10$  and  $\epsilon_{r1}=2-j1$  F/m, respectively. This is reaffirmed by the 3-D plots of the power flow in Figures 4.25 and 4.26 for these two cases. However, the wave attenuation in each case is largely different with  $\alpha=14.1$  Np/m in case A and 24 Np/m in case B, even though the loss is ten times less in the second case. When  $a/b$  is increased to 0.88, these distributions change drastically and display a couple of interesting attributes. For one, in case C ( $\epsilon_{r1}=2-j1$  F/m,  $\alpha=22.5$  Np/m) nearly 90% of the total absolute real power flow is in the innermost dielectric while in case D ( $\epsilon_{r1}=2-j10$  F/m,  $\alpha=33.4$  Np/m) there is only 25%. Secondly, in case D, nearly half the power is flowing in the *pipe* when it covers only 19% of the cross-sectional area, with the remainder roughly distributed between the two other dielectrics. The higher dielectric loss in region one has caused the power flow to concentrate more in the pipe (region two) and also in the air-filled region (region three). This tremendous change in the distribution of the power flow is illustrated in the 3-D plots for cases C and D in Figures 4.27 and 4.28, respectively.

The attenuation characteristics have reversed from those at  $a/b=0.6$ , such that now, for  $a/b=0.88$ , the waveguide arrangement having the larger dielectric loss also has the larger wave attenuation. That is, case C has  $\alpha=22.5$  Np/m while case D, which has more dielectric loss in region one, has  $\alpha=33.4$  Np/m. By increasing the losses in region one, less power flows in this region, in comparison to a similar guide of lesser dielectric loss in region one (as cases A to B and D to C), but the amount of attenuation is dependent on the relative sizes of the dielectric diameters to the sheath size.

The effects that the relative sizes of the dielectric constants have on the power-flow distribution and attenuation can also be quite pronounced. The four cases marked in Figure 4.14 correspond to the four cases in Figure 4.13, except  $\epsilon_{r1}'$  has been increased from 2 to 10 F/m. Between cases B and F at  $a/b=0.6$ , the higher  $\epsilon_{r1}'$  value unexpectedly gives rise to a smaller attenuation—from 24 to 16.9 Np/m. When the radius is increased to  $a/b=0.88$  in cases D and H, the wave is attenuated almost equally in both instances with  $\alpha=33.4$  and 31.5 Np/m, respectively. Furthermore, cases C and G show the greatest amount of difference in the power-flow distributions, but surprisingly have nearly the same attenuation. The reason for this is that both points have  $\epsilon_{r1}''=1$  F/m, which is near that of  $\epsilon_{r2}''=2$  F/m producing roughly the same amount of loss in both dielectrics and, in addition, nearly the same percentage of power flows in the inner two dielectrics in both cases C and G. These facts in combination produce the effect of attenuation which varies only moderately when the dielectric constant in region one is increased by a factor of five. These three comparisons demonstrate that the differences in the dielectric constants among the regions in the waveguide can have a large impact on the power-flow distribution and wave attenuation. More importantly, these comparisons also show that there is no simple relation between the attenuation and power-flow distributions to the relative dielectric diameters and dielectric constants for the inhomogeneous waveguide. The relationships are very complicated and must be obtained for each waveguide arrangement individually as

was done for these examples— by tracing out the  $k_z$  *versus*  $a/b$  plots for many cases while varying the physical parameters.

Furthermore, a large redistribution in power flow by itself does not necessarily imply a significant change in the attenuation. For between cases B and C there is a huge change in the power-flow distribution with only a small change in attenuation, while in cases A and D there is a large redistribution of power flow *and* a large change in attenuation. A large variation in the losses among the dielectrics is an additional factor which must also be considered when making attenuation evaluations for varying physical parameters such as the dielectric radii. Again it should be emphasized that the power-flow distributions and the wave attenuation inside the inhomogeneous, layered waveguide are very complicated functions of the dielectric radii, constitutive parameters, sheath size and frequency. No simple rules-of-thumb are applicable to these waveguides and the correct relationships must be obtained numerically by tracing out the axial wavenumber and computing the desired fielded characteristic.

Table 4.1.

Axial wavenumbers and field expansion coefficients for the seven cases labelled in Figure 4.5 of the  $HE_{11}$  and  $EH_{11}$  modes in the lossy three-dielectric guide having  $\epsilon_{r_1}=20-j0.5$ ,  $\epsilon_{r_2}=3-j0.1$  and  $\epsilon_{r_3}=1$ .

Case	$k_z$ (rad/m)	$C_{11}$	$C_{13}$
A	-9.3-j1.5	1.0	-40.4-j1.1
B	4.9-j0.7	1.0	-54.6+j5.5
C	23.0-j1.0	1.0	-58.0+j2.6
D	28.8-j1.2	1.0	-47.5+j2.0
E	42.3-j2.9	1.0	33.3+j0.5
F	62.1-j1.8	1.0	40.0+j0.4
G	78.1-j1.4	1.0	66.38+j1.1

Table 4.2.

Axial wavenumbers and real absolute power flow distributions for the eight cases labelled in Figures 4.13 and 4.14 of the  $HE_{11}$  mode in the lossy three-dielectric guide having  $b=2.005$  in,  $f=1$  GHz,  $\epsilon_{r_2}=2.7-j2$  and  $\epsilon_{r_3}=1$ .

Case in Figures 4.13 and 4.14	$\epsilon_{r_1}$ (F/m)	$k_z$ (rad/m)	% absolute real power flow in region		
			1	2	3
A	2-j10	11.1-j14.1	-7.402	5.592	87.006
B	2-j1	3.7-j24.0	-18.173	-5.303	76.525
C	2-j1	9.8-j22.5	88.950	3.823	7.227
D	2-j10	37.5-j33.4	24.624	48.645	26.731
E	10-j10	7.9-j12.0	-4.079	7.405	88.515
F	10-j1	2.9-j16.9	7.279	8.861	83.861
G	10-j1	2.5-j29.0	23.965	68.518	7.517
H	10-j10	31.6-j31.5	33.290	45.277	21.434



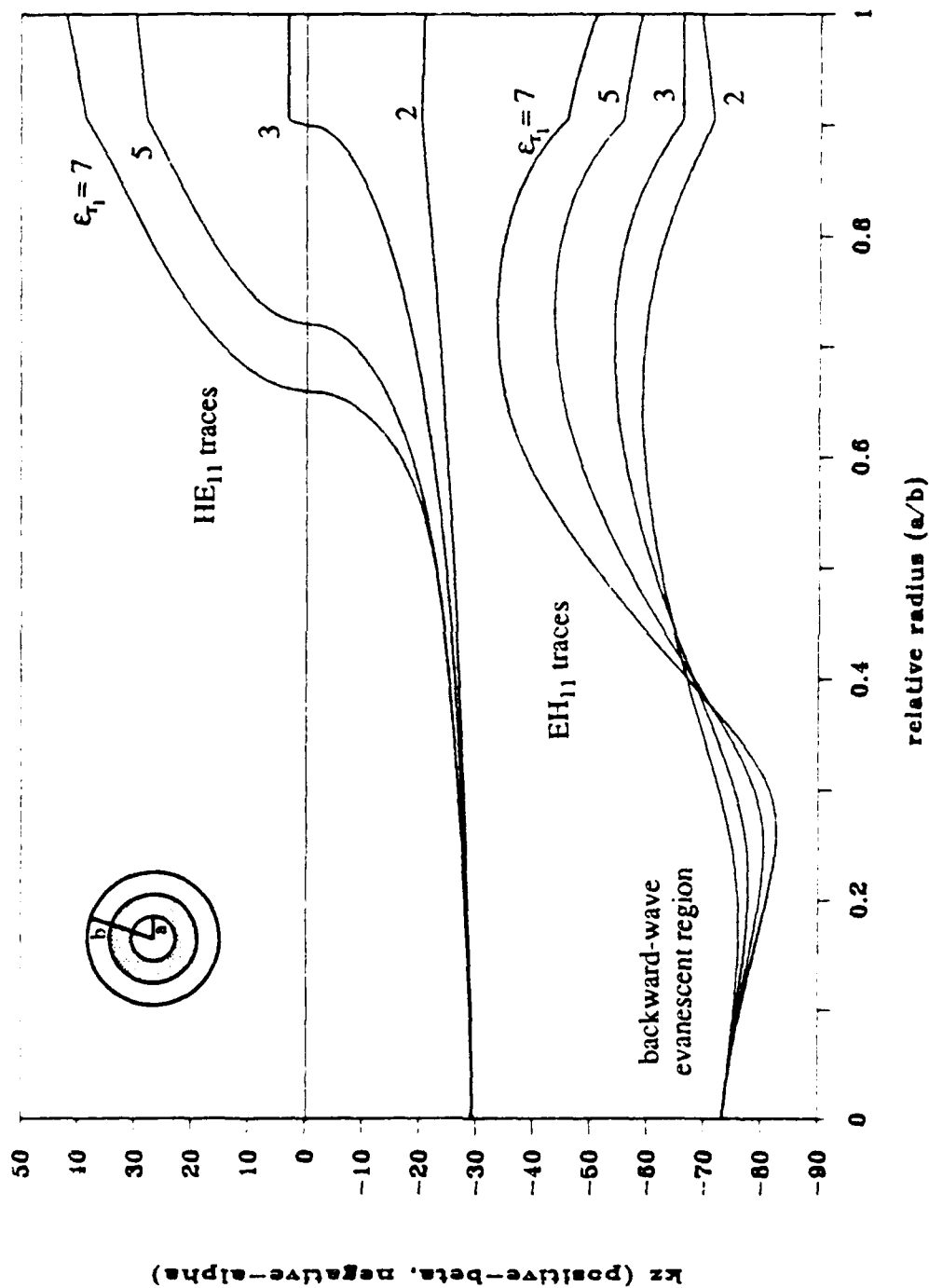


Figure 4.1. Traces of  $k_z$  versus  $a/b$  for the  $HE_{11}$  and  $EH_{11}$  modes in the three-dielectric waveguide at 1 GHz with  $\epsilon_{r1}$  as parameter,  $\epsilon_{r2}=3$  and  $\epsilon_{r3}=1$ .

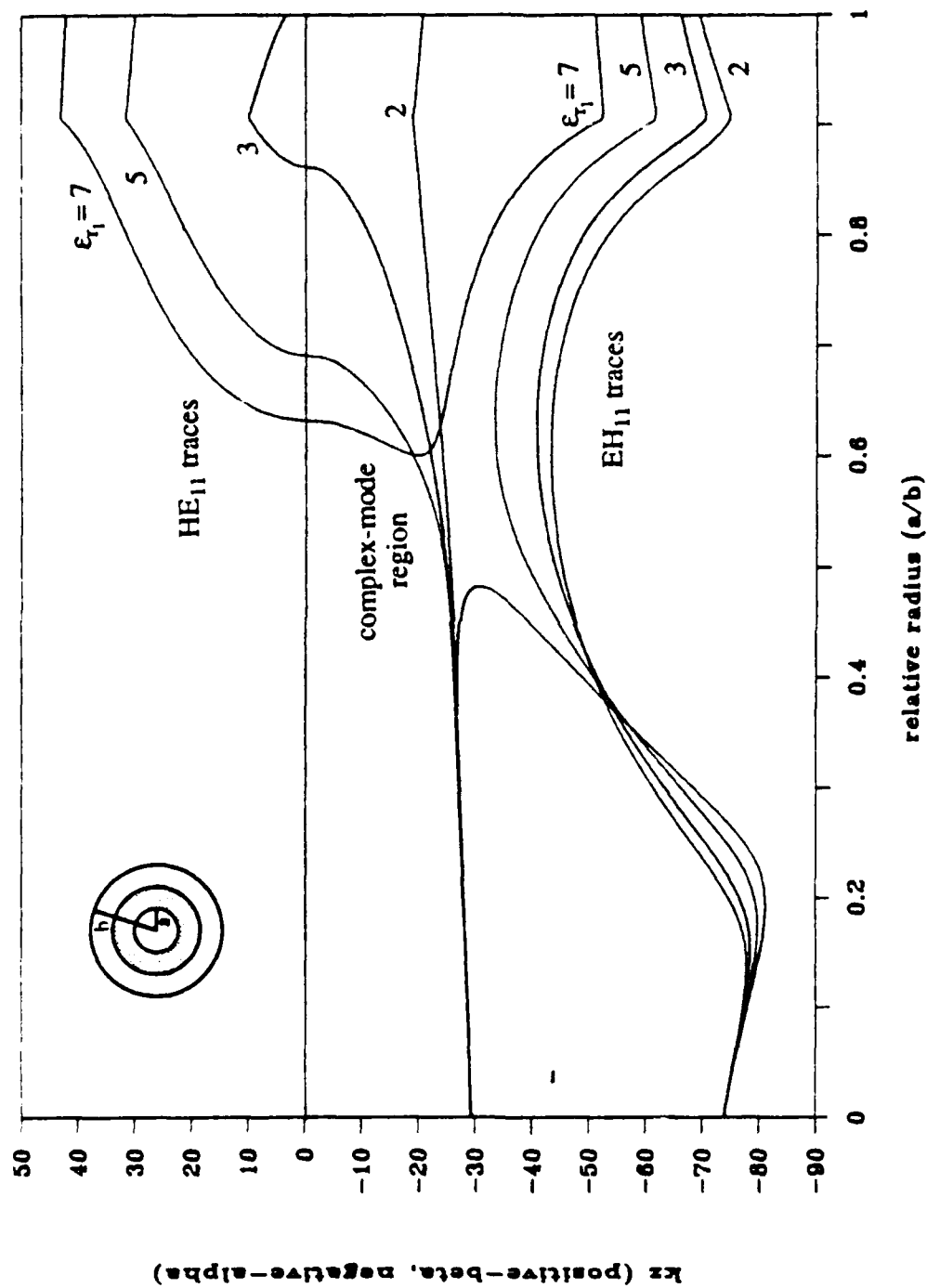


Figure 4.2. Traces of  $k_z$  versus  $a/b$  for the  $HE_{11}$  and  $EH_{11}$  modes in the three-dielectric waveguide at 1 GHz with  $\epsilon_{r1}$  as parameter,  $\epsilon_{r2}=10$  and  $\epsilon_{r3}=1$ .

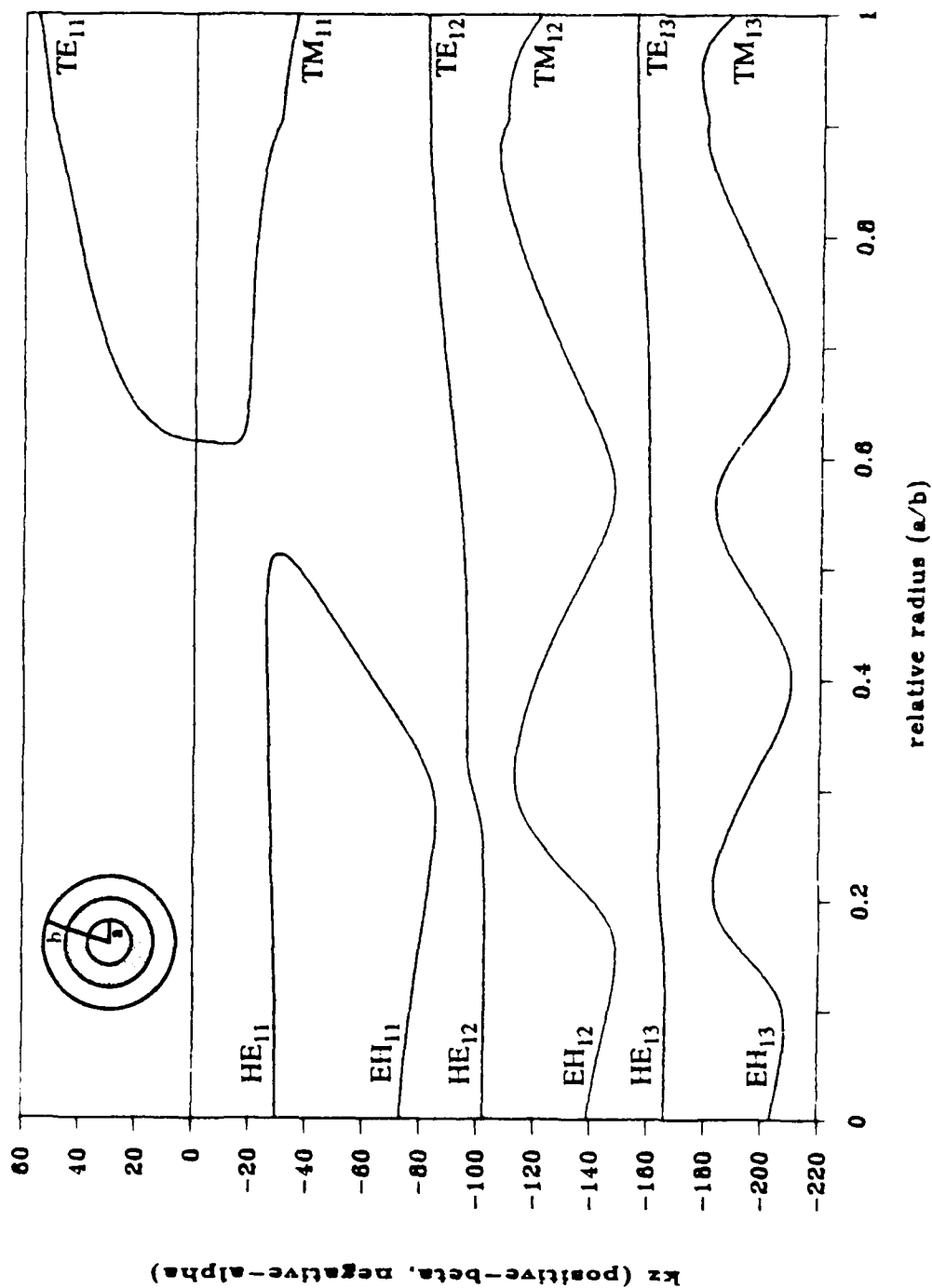


Figure 4.3. Traces of  $k_z$  versus  $a/b$  for the  $HE_{1m}$  and  $EH_{1m}$  modes in the three-dielectric waveguide with  $m=1, 2$  and  $3$ , having  $f=1$  GHz,  $b=2.005$  in,  $\epsilon_{r1}=10$ ,  $\epsilon_{r2}=3$  and  $\epsilon_{r3}=1$ .

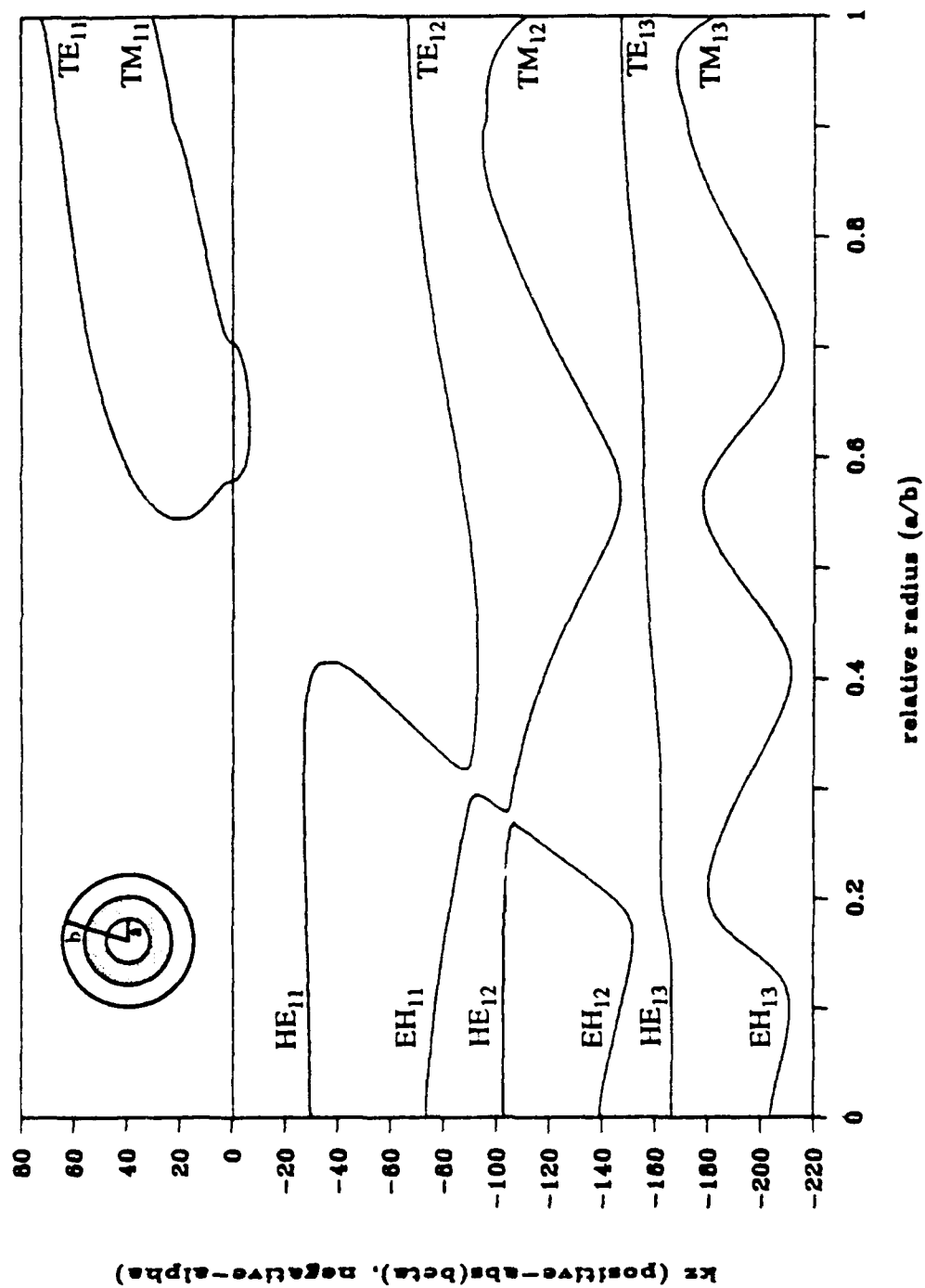


Figure 4.4. Traces of  $k_z$  versus  $a/b$  for the  $HE_{1m}$  and  $EH_{1m}$  modes in the three-dielectric waveguide with  $m=1, 2$  and  $3$ , having  $f=1$  GHz,  $b=2.005$  in,  $\epsilon_{r1}=15$ ,  $\epsilon_{r2}=3$  and  $\epsilon_{r3}=1$ .

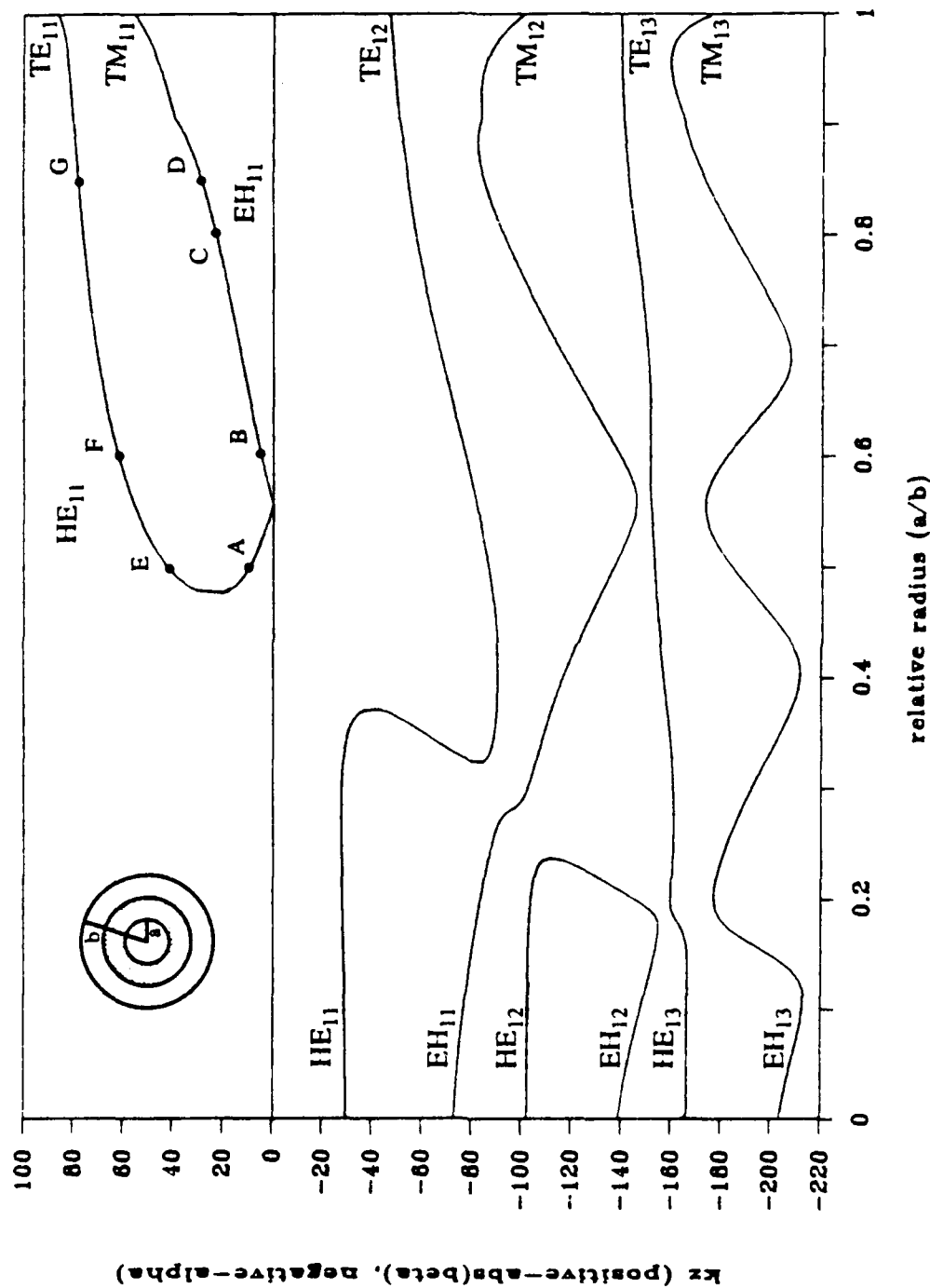


Figure 4.5. Traces of  $k_z$  versus  $a/b$  for the  $HE_{1m}$  and  $EH_{1m}$  modes in the three-dielectric waveguide with  $m=1, 2$  and  $3$ , having  $f=1$  GHz,  $b=2.005$  in,  $\epsilon_{r_1}=20$ ,  $\epsilon_{r_2}=3$  and  $\epsilon_{r_3}=1$ .

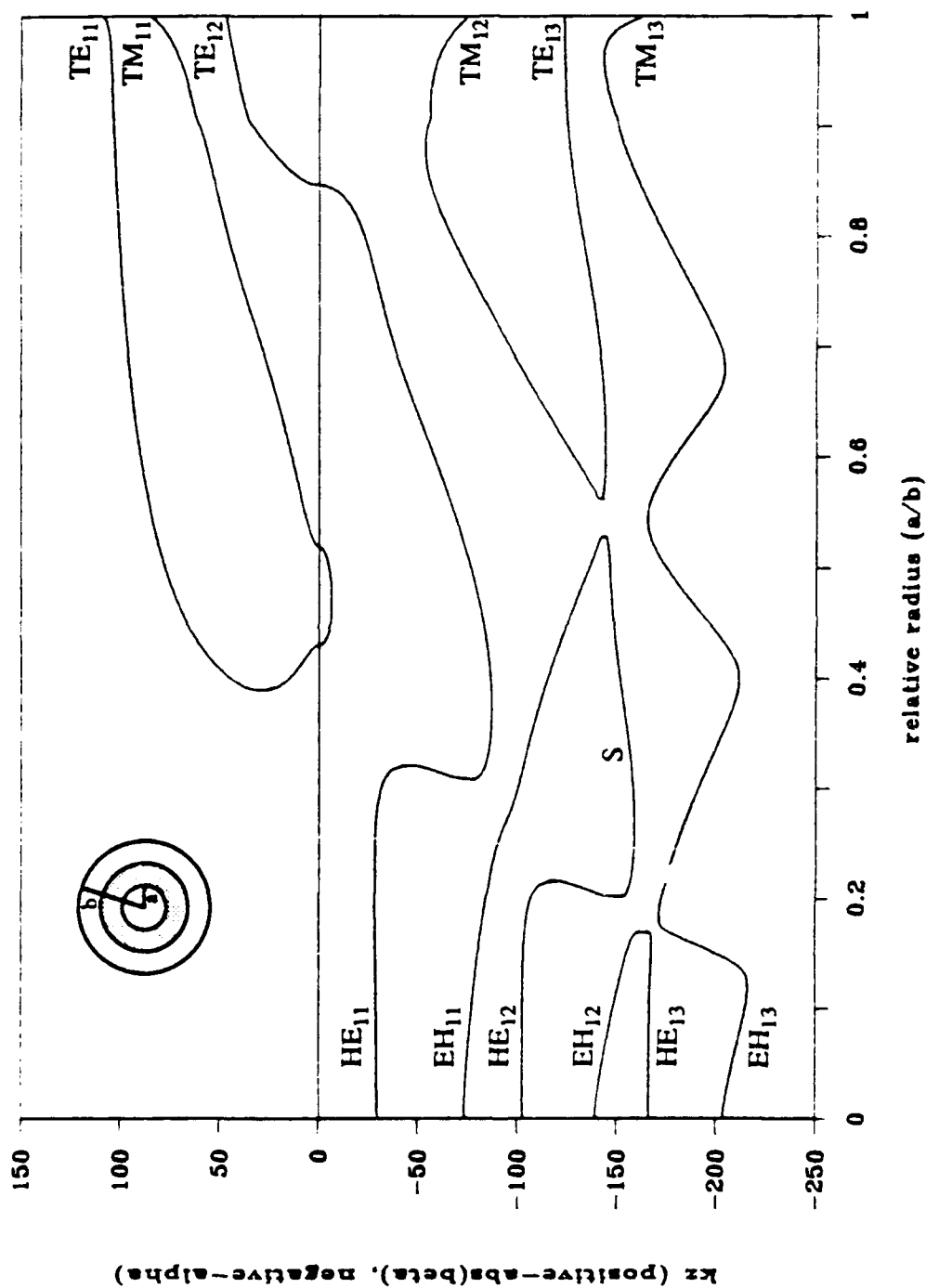


Figure 4.6. Traces of  $k_z$  versus  $a/b$  for the  $HE_{1m}$  and  $EH_{1m}$  modes in the three-dielectric waveguide with  $m=1, 2$  and  $3$ , having  $f=1$  GHz,  $b=2.005$  in,  $\epsilon_{r1}=30$ ,  $\epsilon_{r2}=3$  and  $\epsilon_{r3}=1$ .

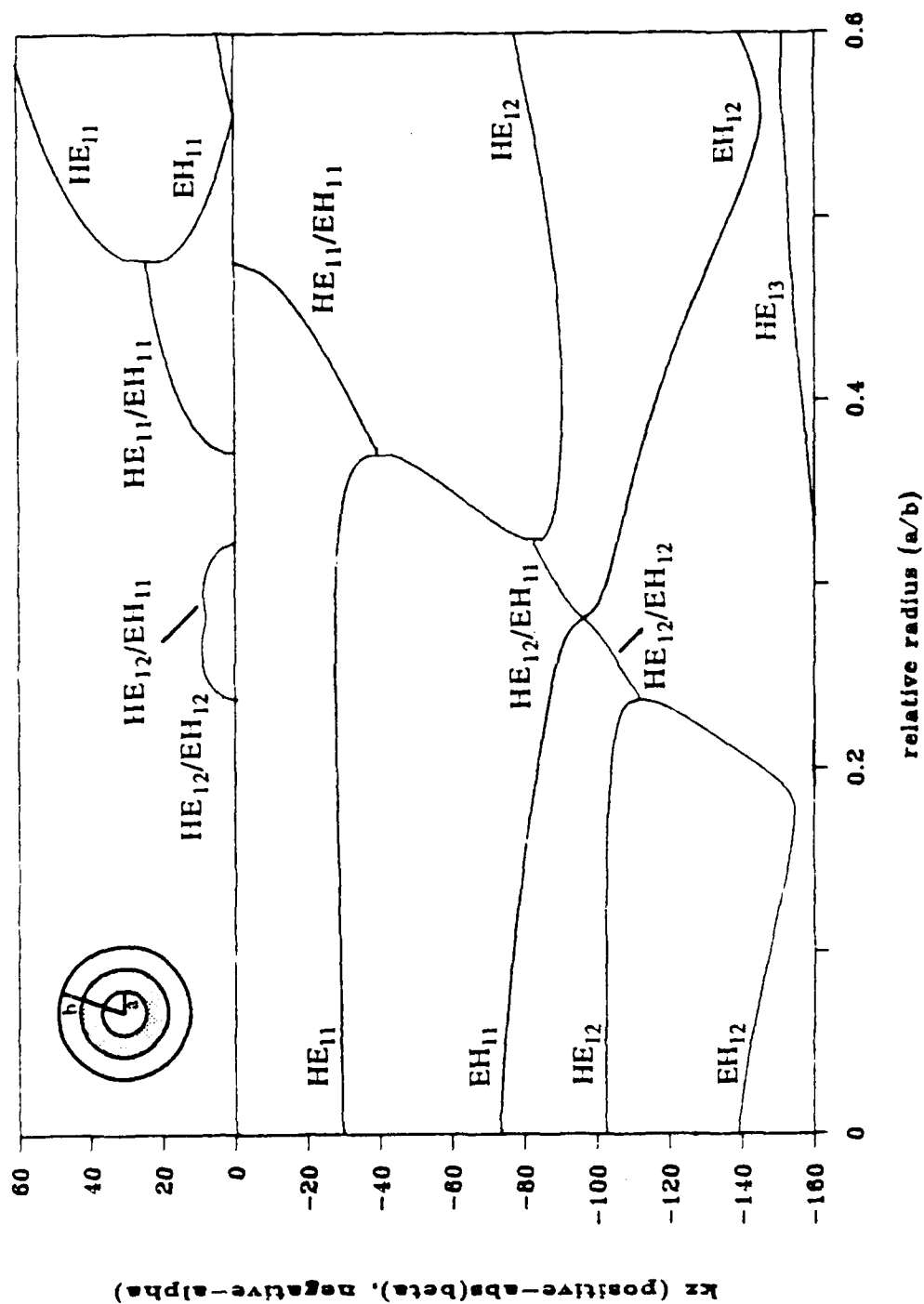


Figure 4.7. Traces of  $k_z$  versus  $a/b$  for the  $HE_{1m}$  and  $EH_{1m}$  modes in the three-dielectric waveguide, including complex modes, with  $m=1, 2$  and  $3$ , having  $f=1$  GHz,  $b=2.005$  in,  $\epsilon_{r1}=20$ ,  $\epsilon_{r2}=3$  and  $\epsilon_{r3}=1$ .

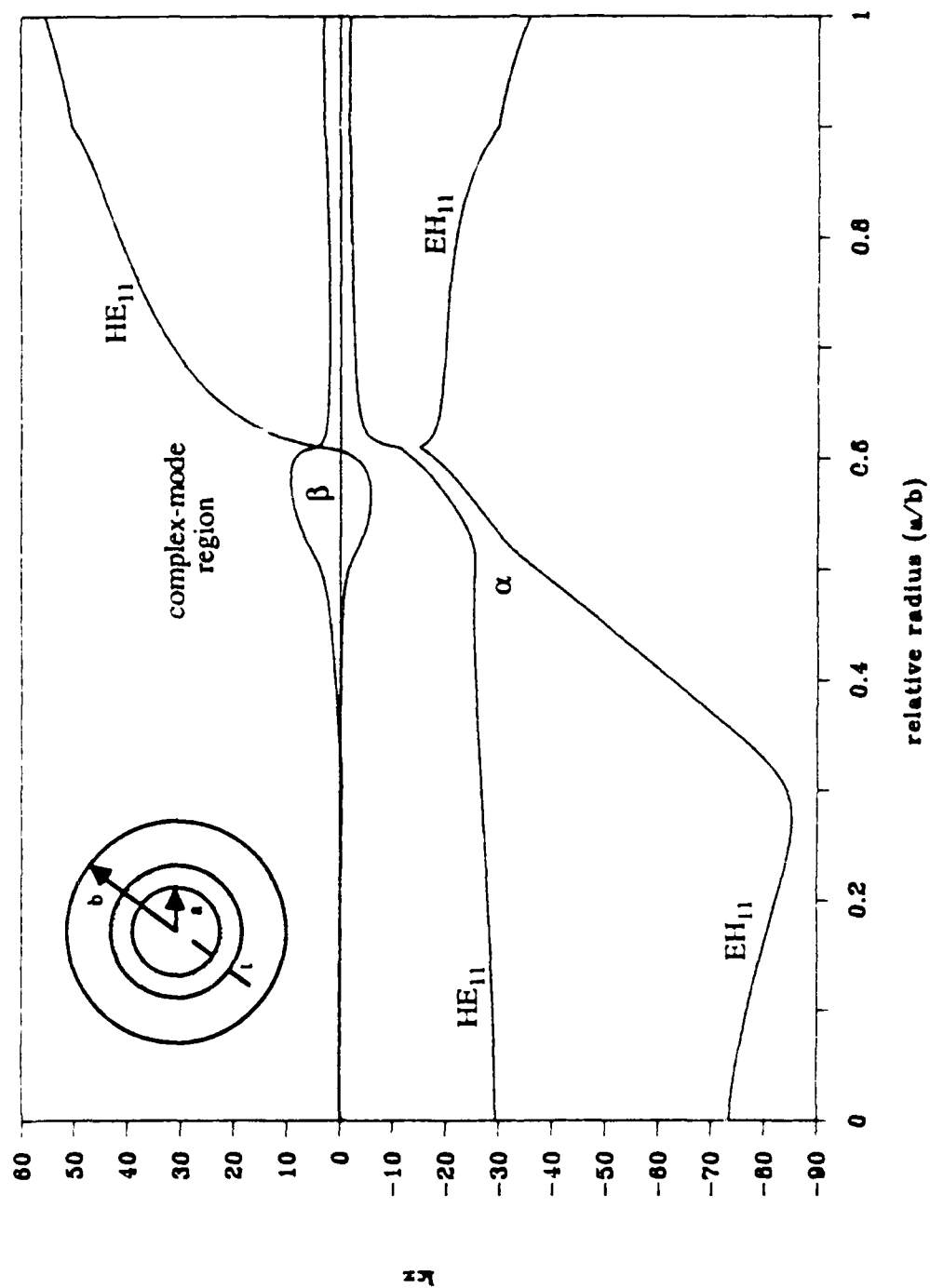


Figure 4.8. Traces of  $k_z$  versus  $a/b$  for the  $HE_{11}$  and  $EH_{11}$  modes in the lossy three-dielectric waveguide having  $f=1$  GHz,  $b=2.005$  in,  $t=0.2$  in,  $\epsilon_{r_1}=10-j0.5$ ,  $\epsilon_{r_2}=3$  and  $\epsilon_{r_3}=1$ .



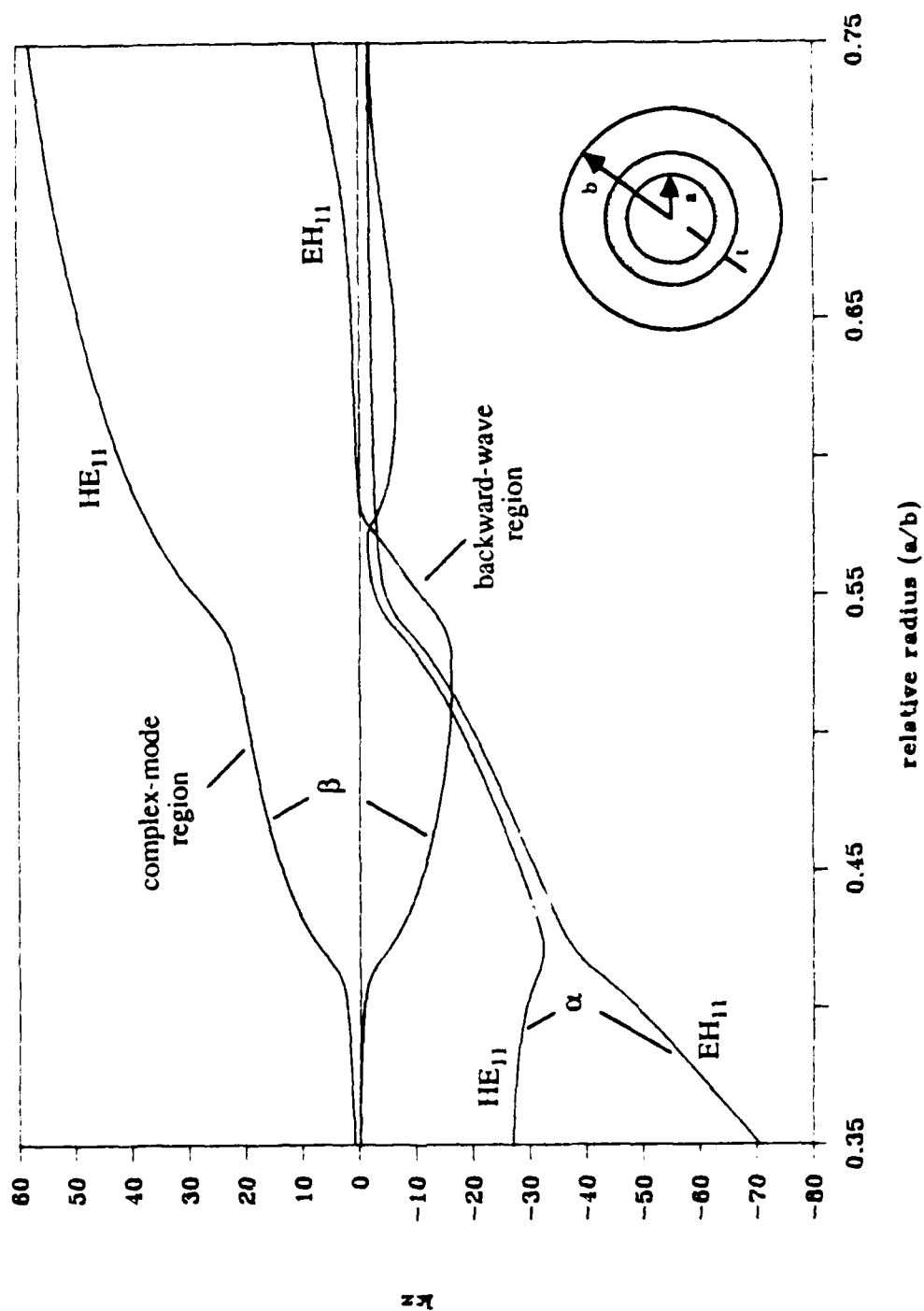


Figure 4.9. Traces of  $k_z$  versus  $a/b$  for the  $HE_{11}$  and  $EH_{11}$  modes in the lossy three-dielectric waveguide having  $f = 1$  GHz,  $b = 2.005$  in,  $t = 0.2$  in,  $\epsilon_{r1} = 15 - j0.5$ ,  $\epsilon_{r2} = 3$  and  $\epsilon_{r3} = 1$ .

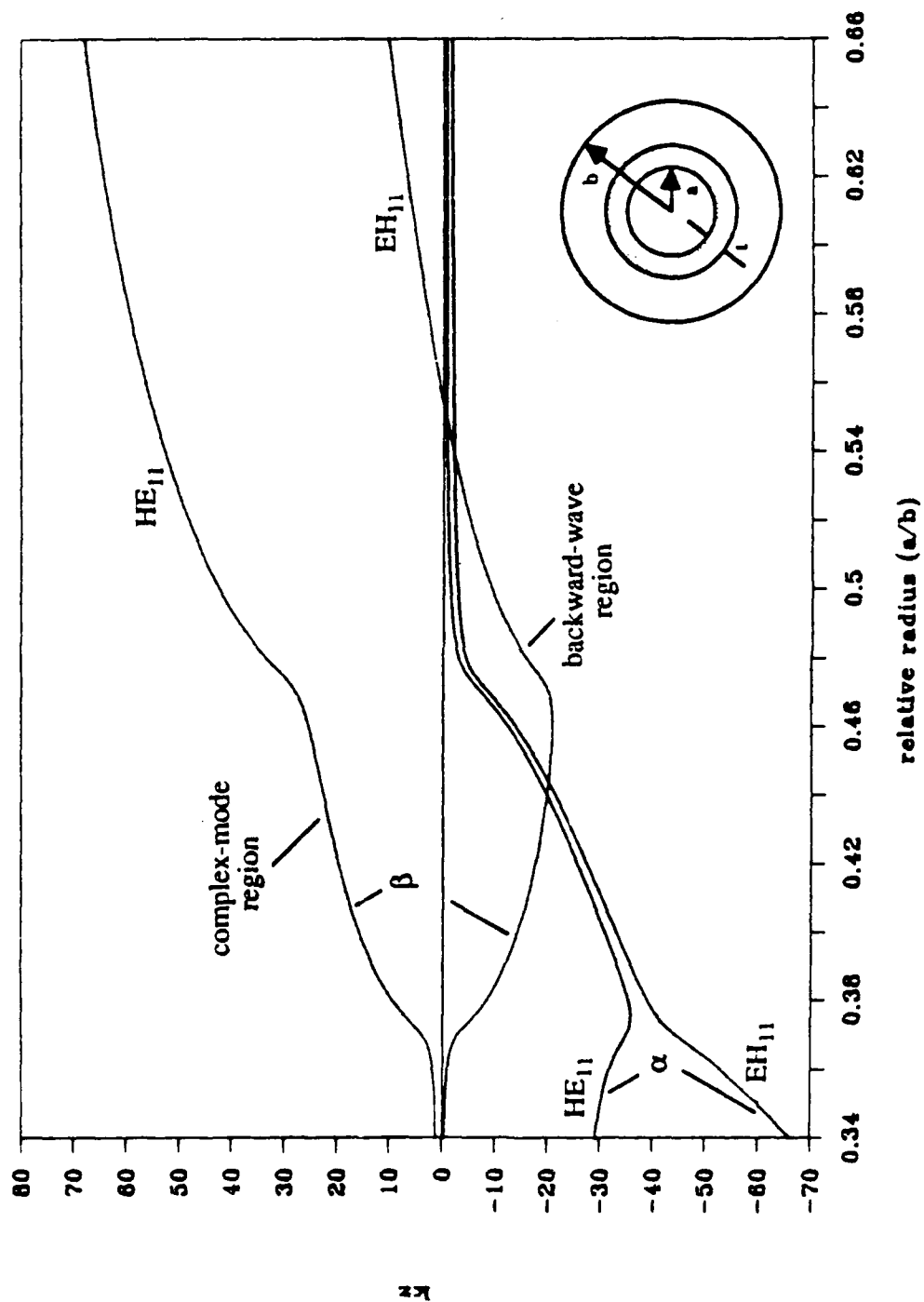


Figure 4.10. Traces of  $k_z$  versus  $a/b$  for the  $HE_{11}$  and  $EH_{11}$  modes in the lossy three-dielectric waveguide having  $f=1$  GHz,  $b=2.005$  in,  $t=0.2$  in,  $\epsilon_{r1}=20-j0.5$ ,  $\epsilon_{r2}=3$  and  $\epsilon_{r3}=1$ .

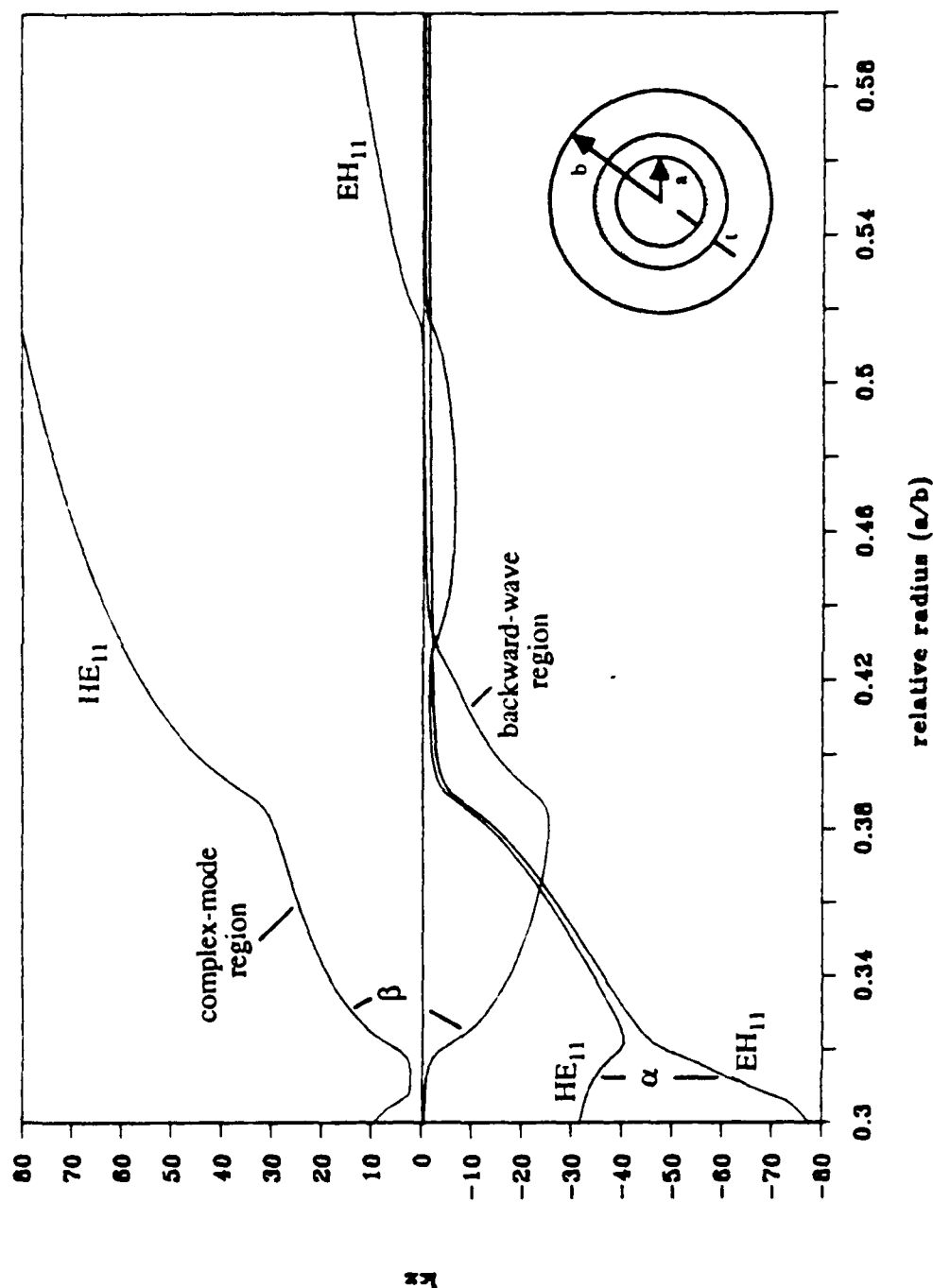


Figure 4.11. Traces of  $k_z$  versus  $a/b$  for the  $HE_{11}$  and  $EH_{11}$  modes in the lossy three-dielectric waveguide having  $f=1$  GHz,  $b=2.005$  in,  $t=0.2$  in,  $\epsilon_{r_1}=30-j0.5$ ,  $\epsilon_{r_2}=3$  and  $\epsilon_{r_3}=1$ .

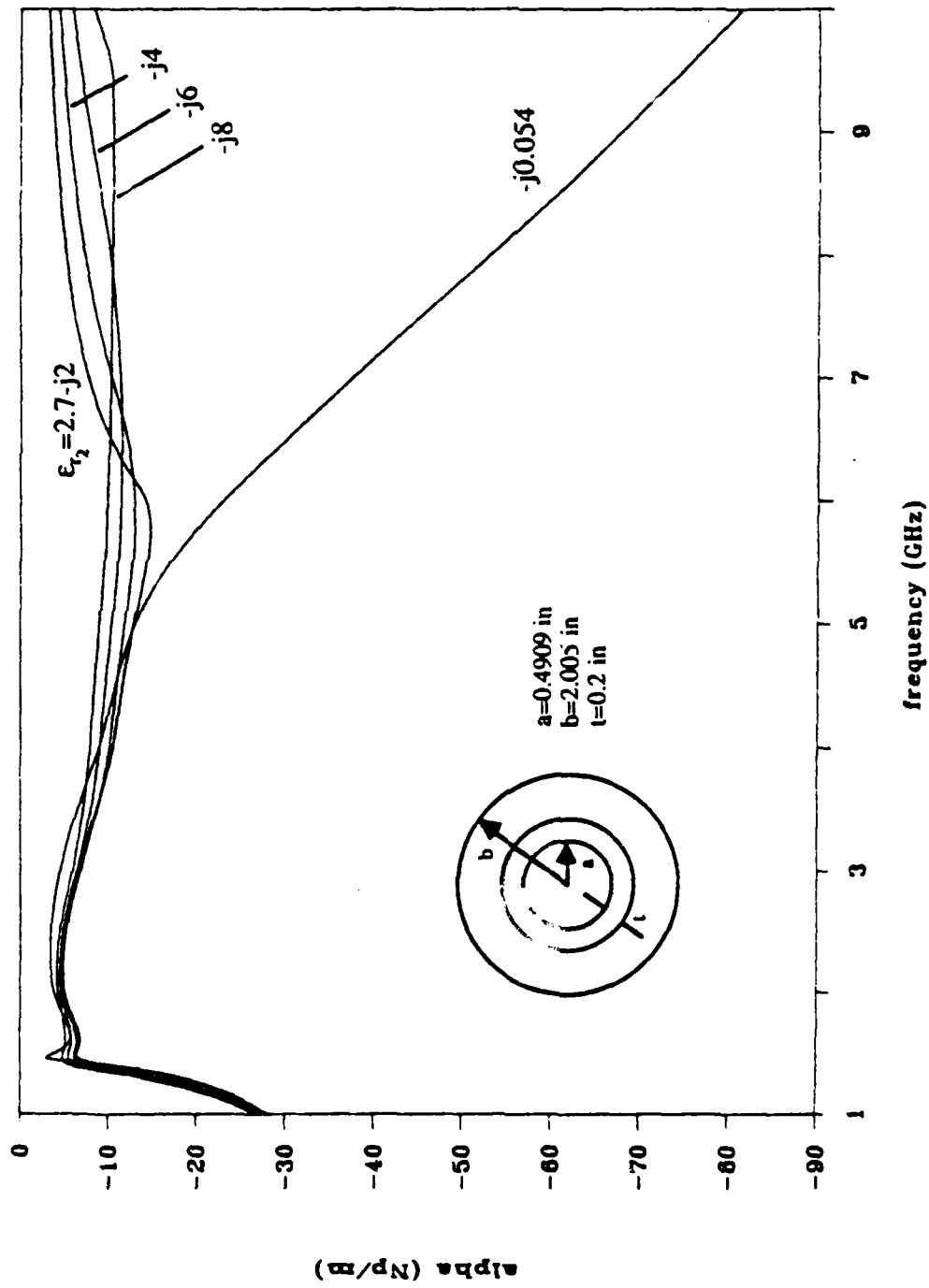


Figure 4.12. Traces of  $\alpha$  versus frequency for the  $HE_{11}$  mode of the three-dielectric guide filled with a pipe containing the three-point dispersive methanol of Section 5.4. The  $\epsilon_{r2}'=2.7$  and the parameter is  $\epsilon_{r2}''$ .

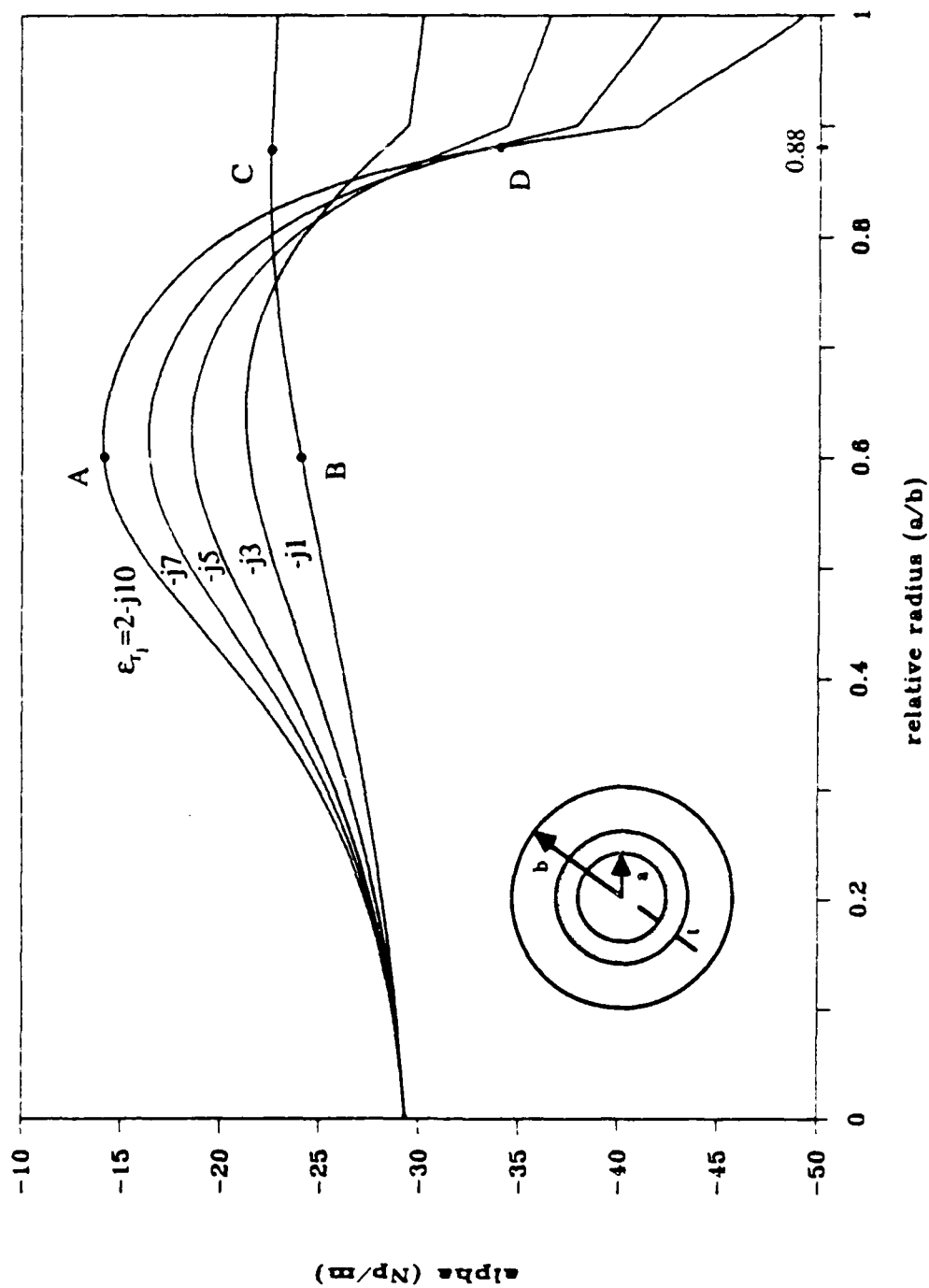


Figure 4.13. Traces of  $\alpha$  versus  $a/b$  for the  $HE_{11}$  mode in the three-dielectric guide having  $f=1$  GHz,  $b=2.005$  in,  $t=0.2$  in,  $\epsilon'_{r1}=2$ ,  $\epsilon'_{r2}=2.7-j2$  and  $\epsilon_{r3}=1$ , with  $\epsilon''_{r1}$  as parameter.

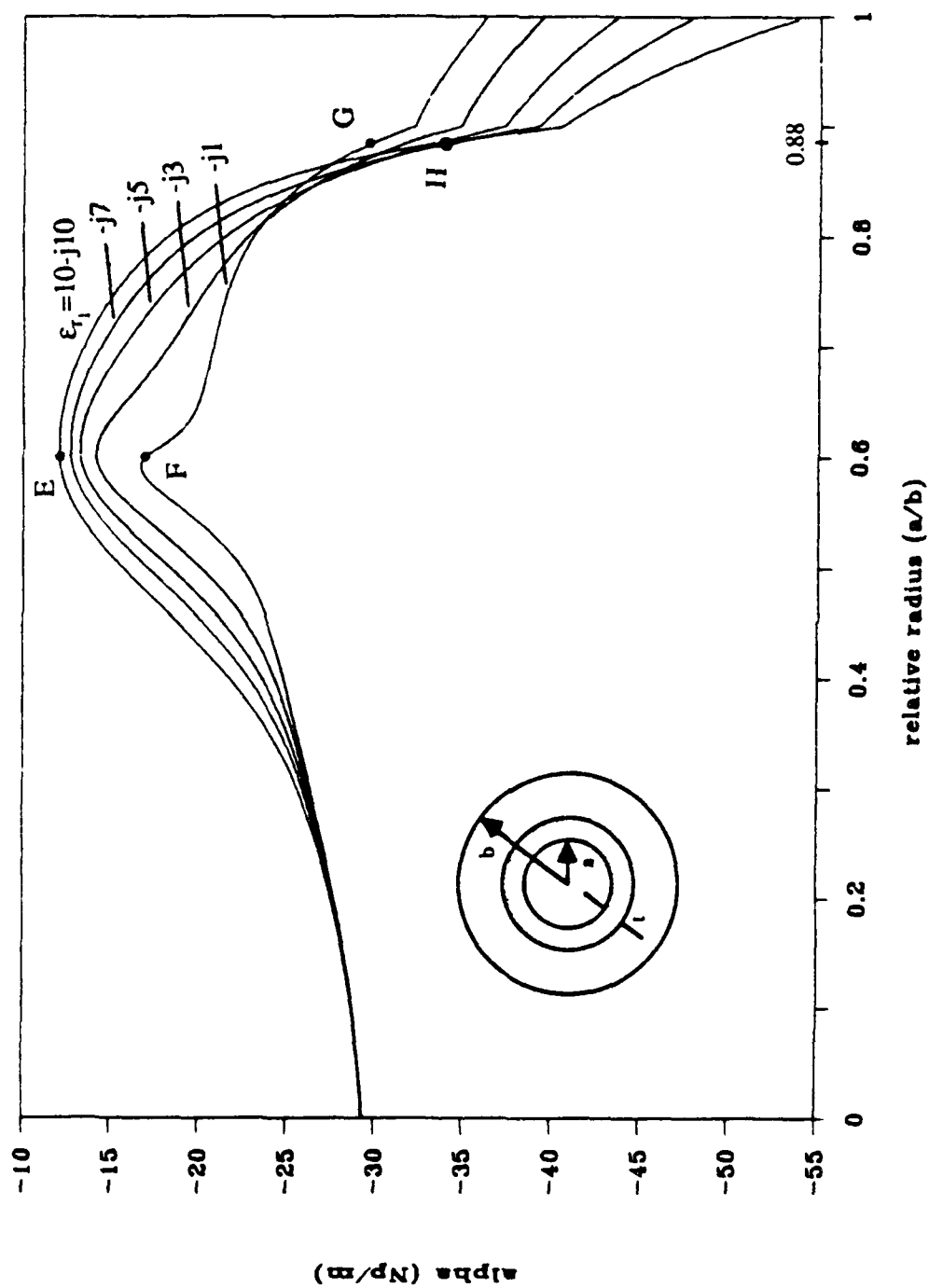


Figure 4.14. Traces of  $\alpha$  versus  $a/b$  for the  $HE_{11}$  mode in the three-dielectric guide having  $f=1$  GHz,  $b=2.005$  in,  $t=0.2$  in,  $\epsilon_{r1}'=10$ ,  $\epsilon_{r2}=2.7-j2$  and  $\epsilon_{r3}=1$ , with  $\epsilon_{r1}''$  as parameter.

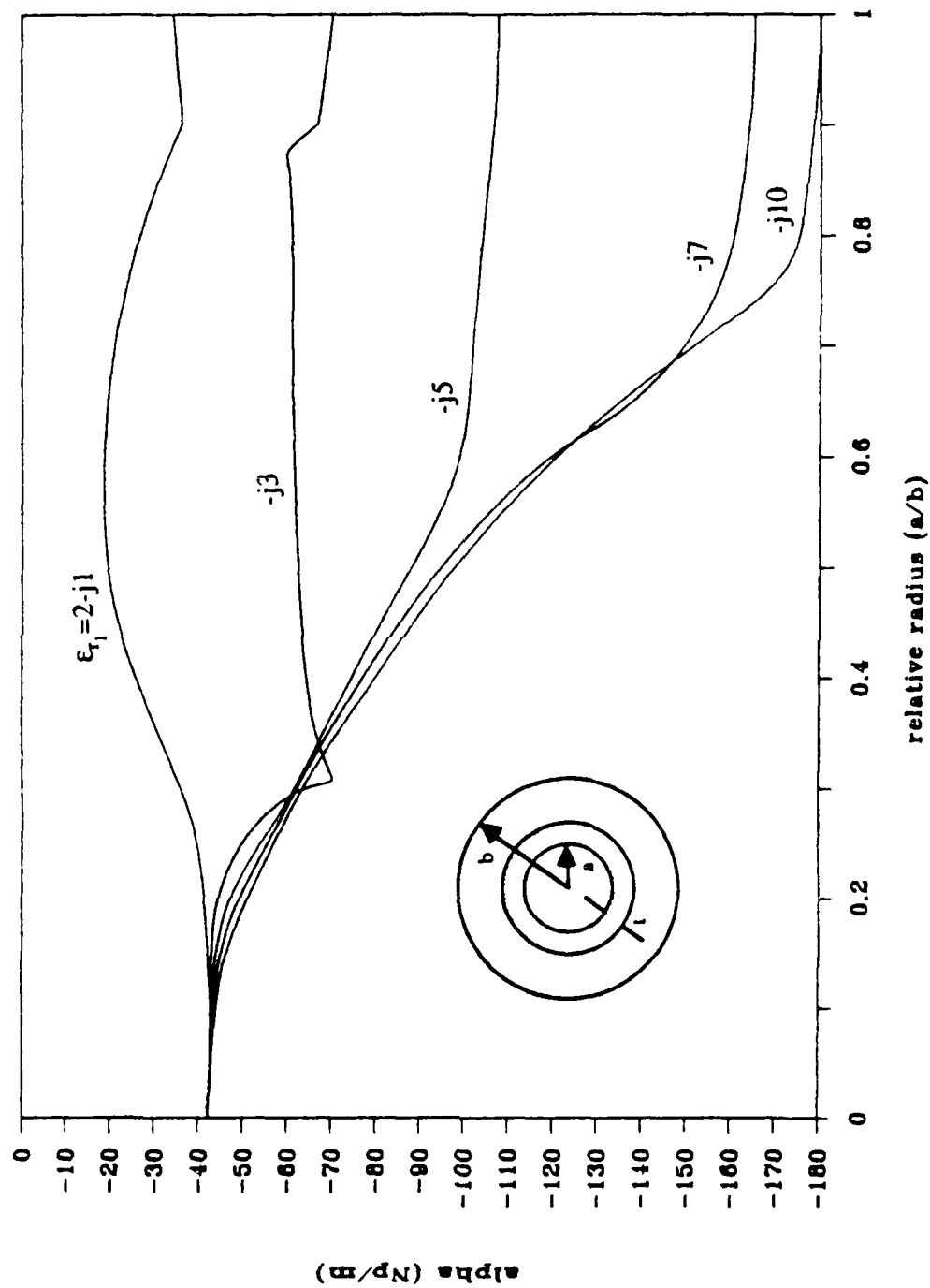


Figure 4.15. Traces of  $\alpha$  versus  $a/b$  for the  $EH_{11}$  mode in the three-dielectric guide having  $f=3$  GHz,  $b=2.005$  in,  $t=0.2$  in,  $\epsilon_{r1}'=2$ ,  $\epsilon_{r2}=2.7-j2$  and  $\epsilon_{r3}=1$ , with  $\epsilon_{r1}''$  as parameter.

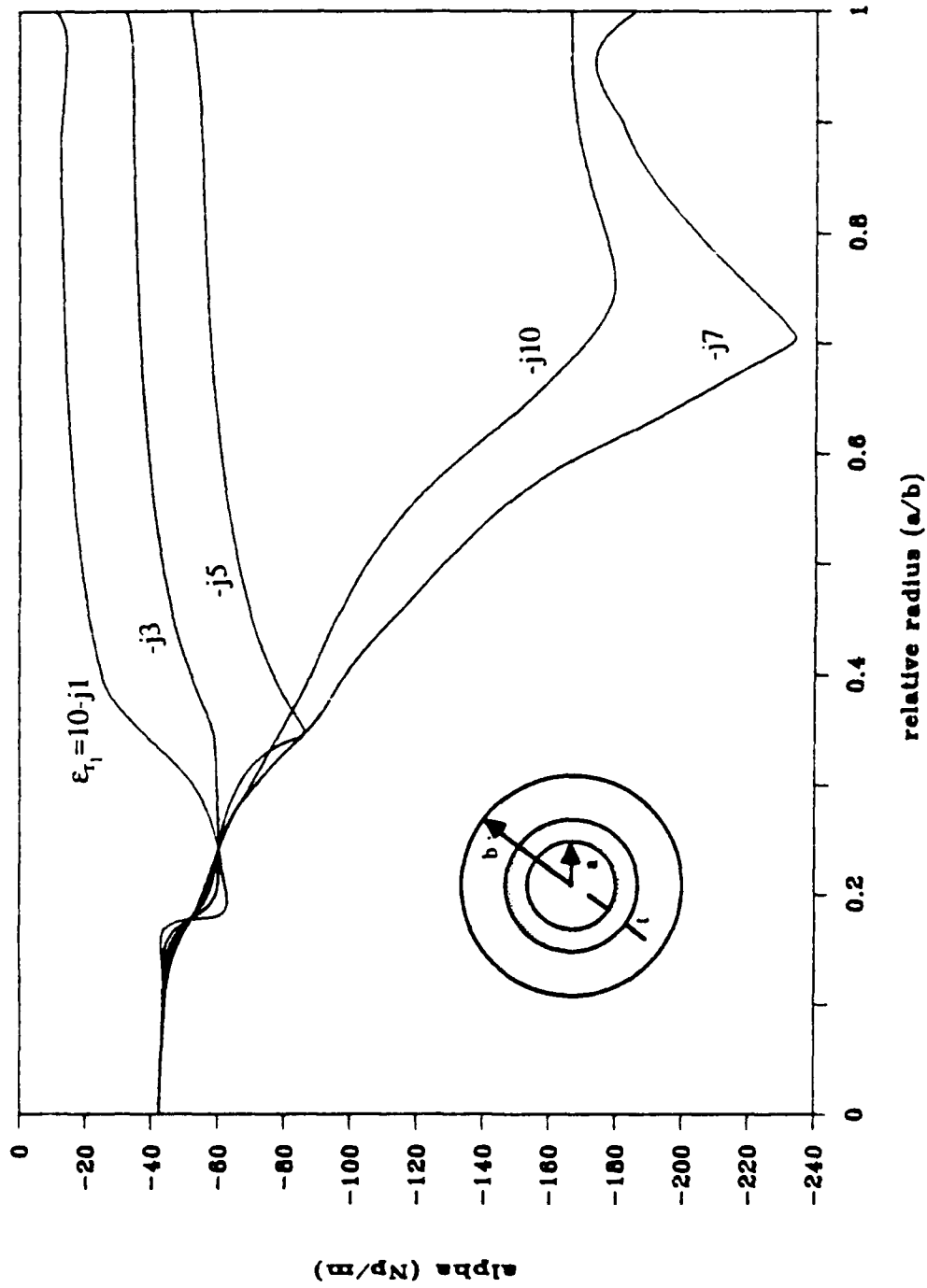


Figure 4.16. Traces of  $\alpha$  versus  $a/b$  for the  $\text{EH}_{11}$  mode in the three-dielectric guide having  $f=3$  GHz,  $b=2.005$  in,  $t=0.2$  in,  $\epsilon_{r1}'=10$ ,  $\epsilon_{r2}=2.7-j2$  and  $\epsilon_{r3}=1$ , with  $\epsilon_{r1}''$  as parameter.



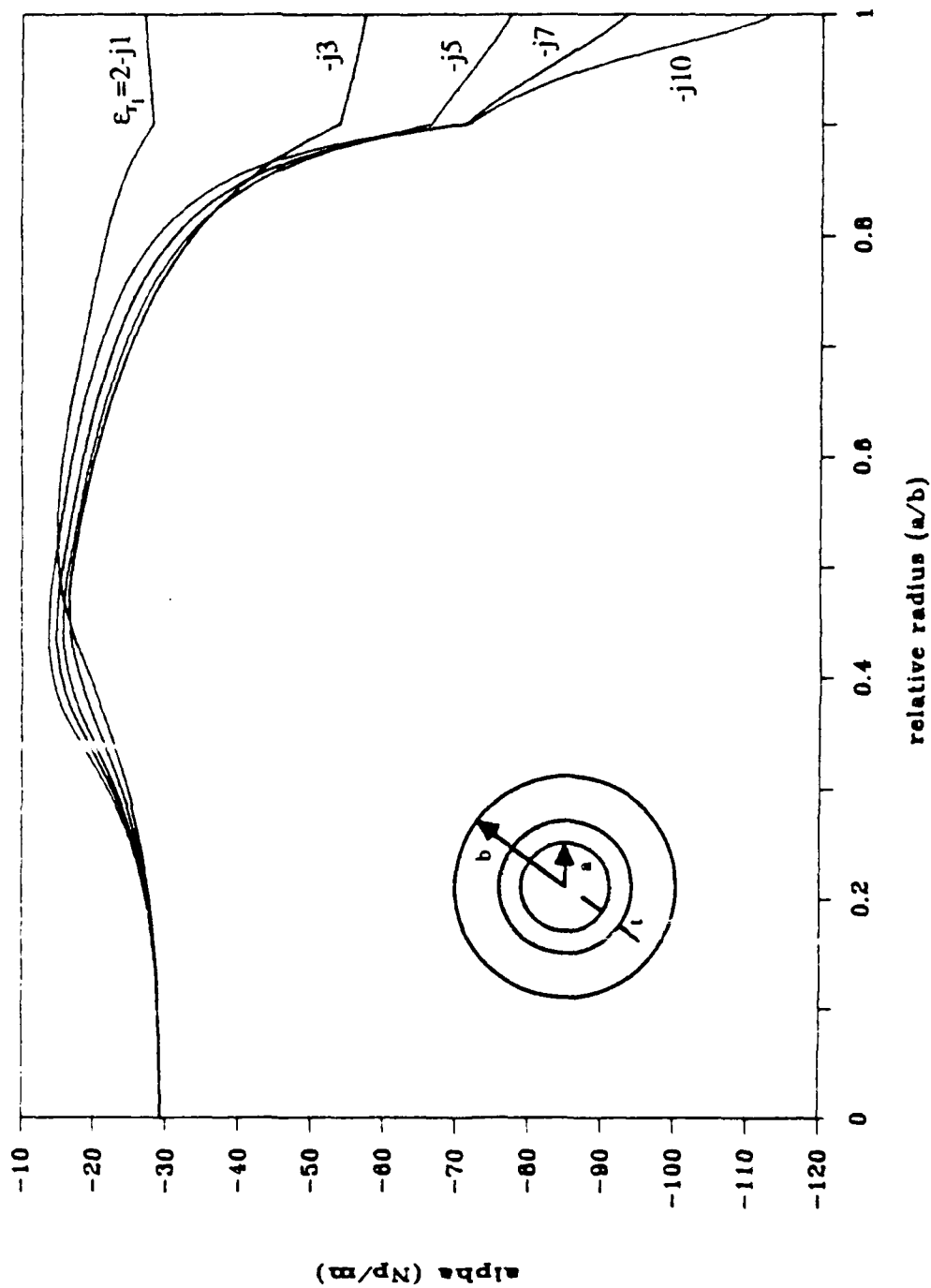


Figure 4.17. Traces of  $\alpha$  versus  $a/b$  for the  $HE_{21}$  mode in the three-dielectric guide having  $f=2.5$  GHz,  $b=2.005$  in,  $t=0.2$  in,  $\epsilon'_{r1}=2$ ,  $\epsilon'_r=2.7-j2$  and  $\epsilon_{r3}=1$ , with  $\epsilon''_{r1}$  as parameter.

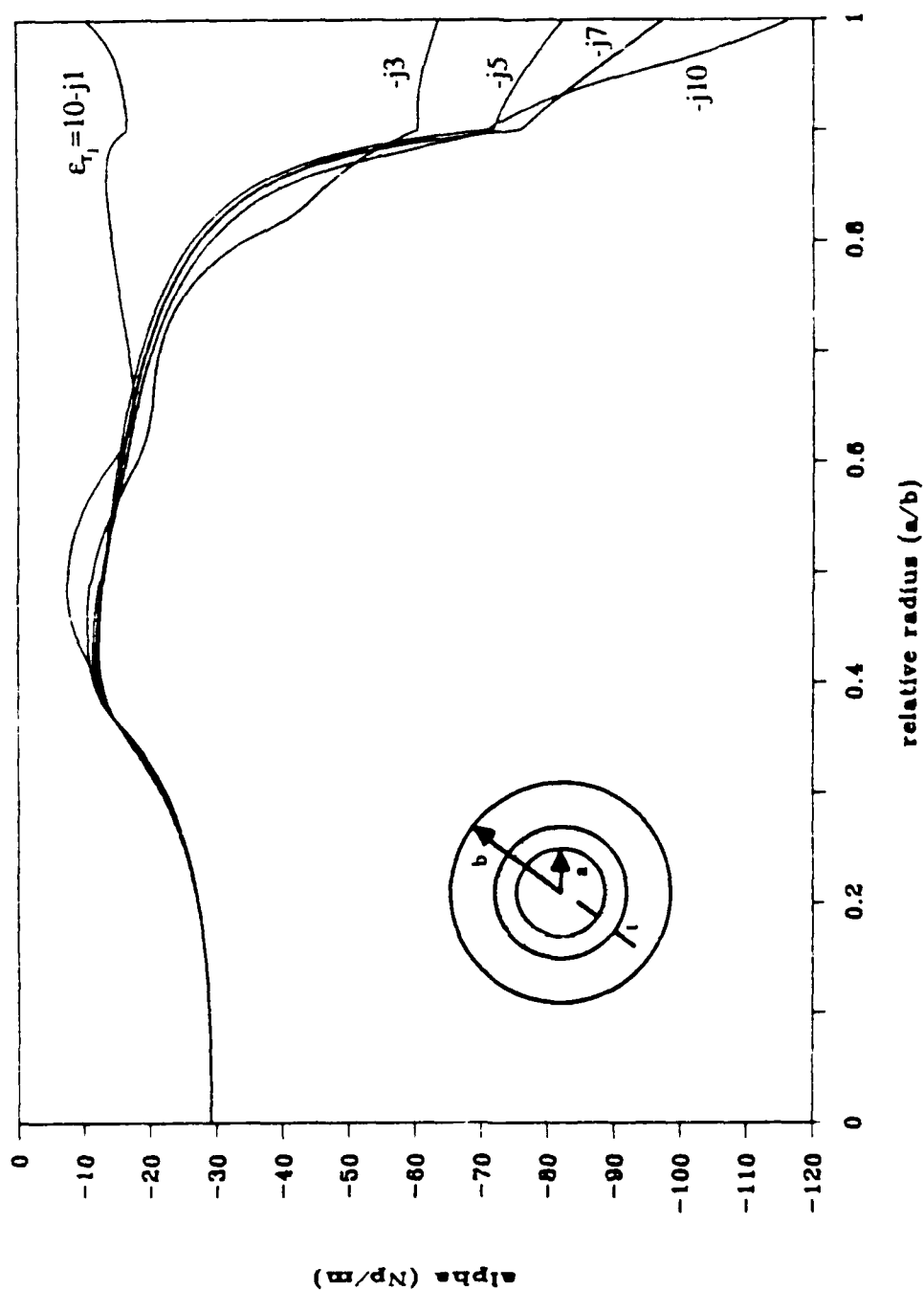


Figure 4.18. Traces of  $\alpha$  versus  $a/b$  for the  $HE_{21}$  mode in the three-dielectric guide having  $f=2.5$  GHz,  $b=2.005$  in,  $t=0.2$  in,  $\epsilon'_{r1}=10$ ,  $\epsilon'_{r2}=2.7-j2$  and  $\epsilon'_{r3}=1$ , with  $\epsilon''_{r1}$  as parameter.

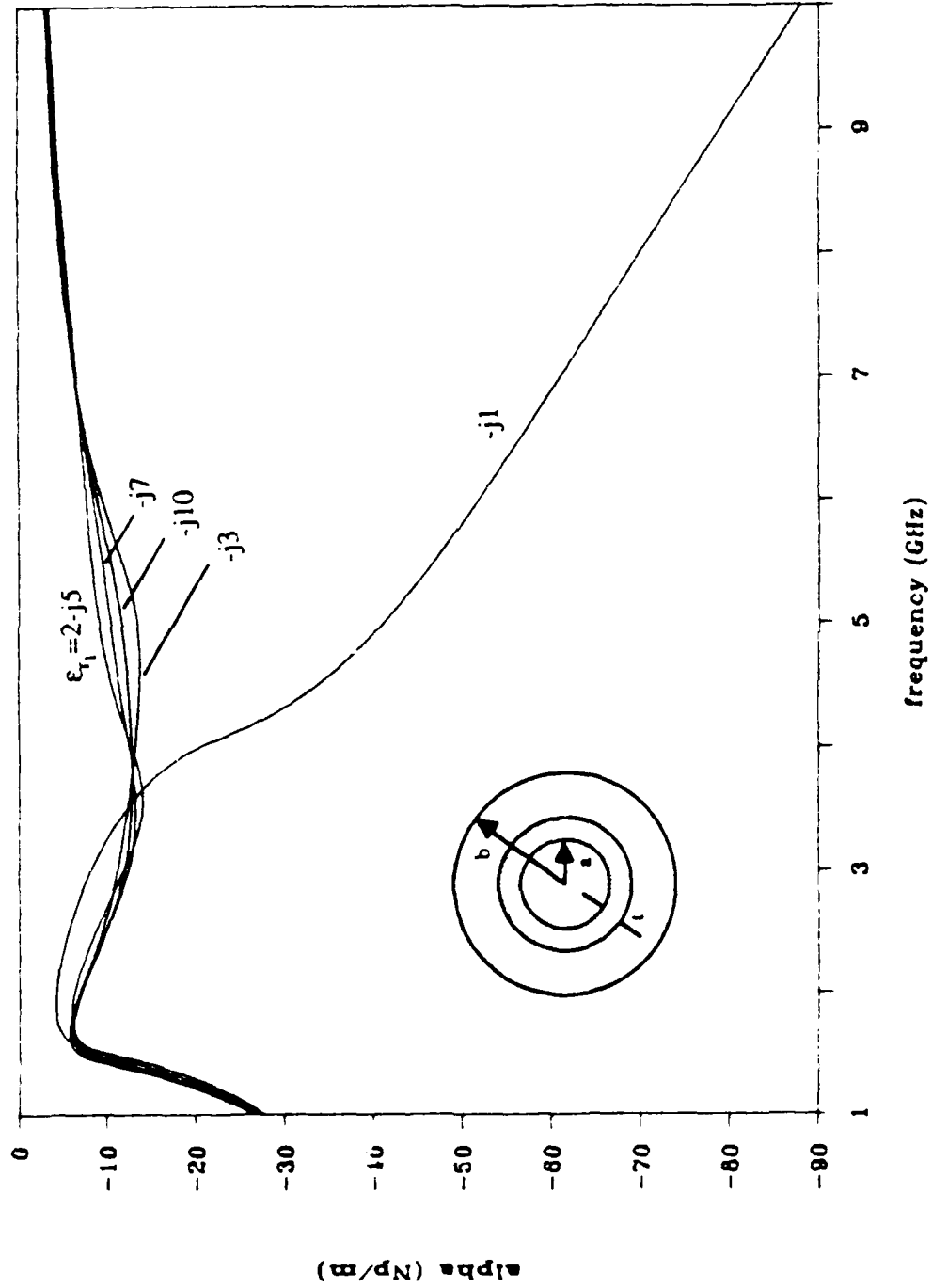


Figure 4.19. Traces of  $\alpha$  versus frequency for the  $HE_{11}$  mode in the three-dielectric guide having  $a=0.4909$  in,  $b=2.005$  in,  $t=0.2$  in,  $\epsilon_{r1}'=2$ ,  $\epsilon_{r2}=2.7-j2$  and  $\epsilon_{r3}=1$ , with  $\epsilon_{r1}''$  as parameter.

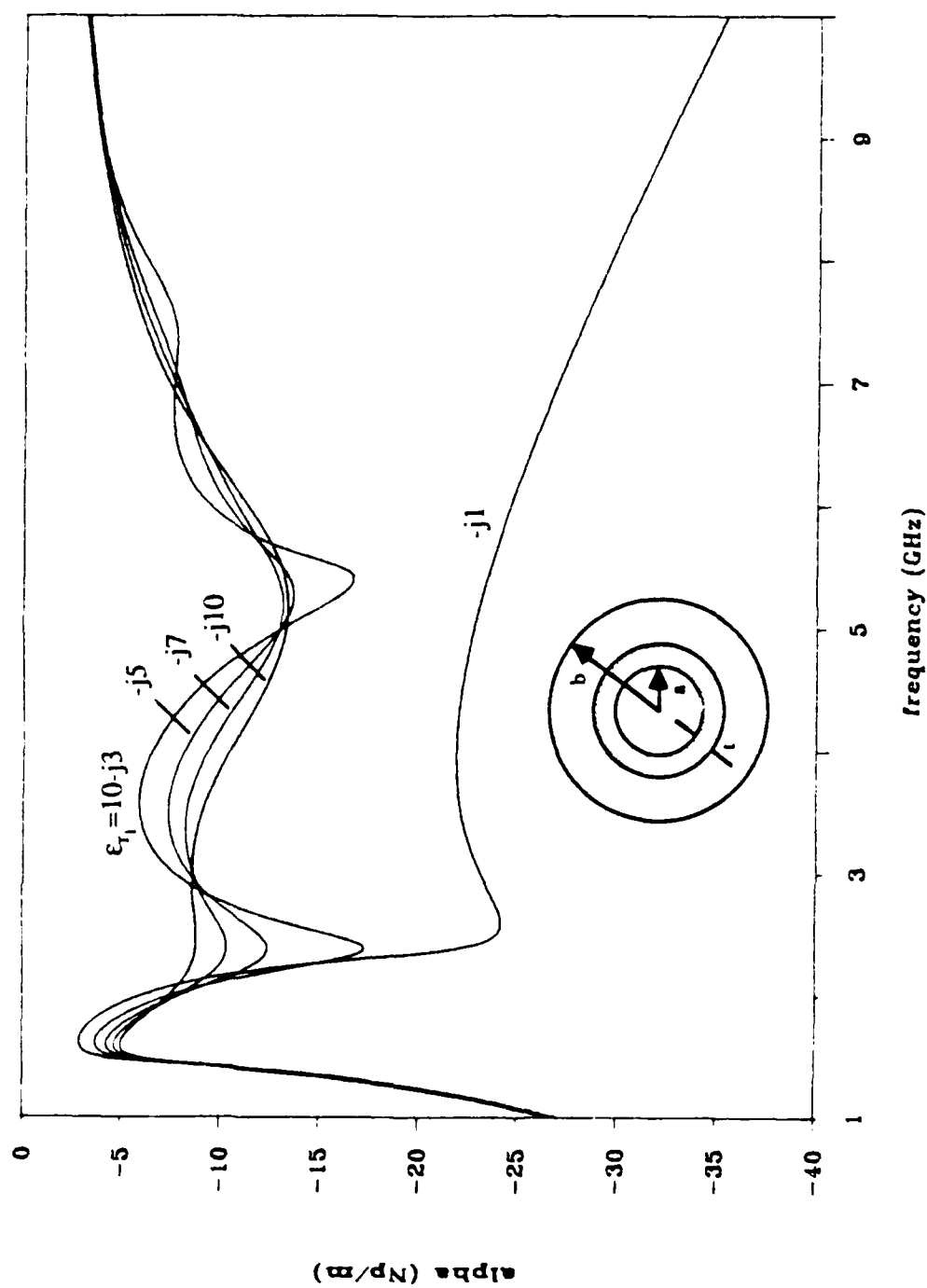


Figure 4.20. Traces of  $\alpha$  versus frequency for the  $HE_{11}$  mode in the three-dielectric guide having  $a=0.4909$  in,  $b=2.005$  in,  $t=0.2$  in,  $\epsilon'_{r1}=10$ ,  $\epsilon'_{r2}=2.7-j2$  and  $\epsilon_{r3}=1$ , with  $\epsilon_{r1}$  as parameter.

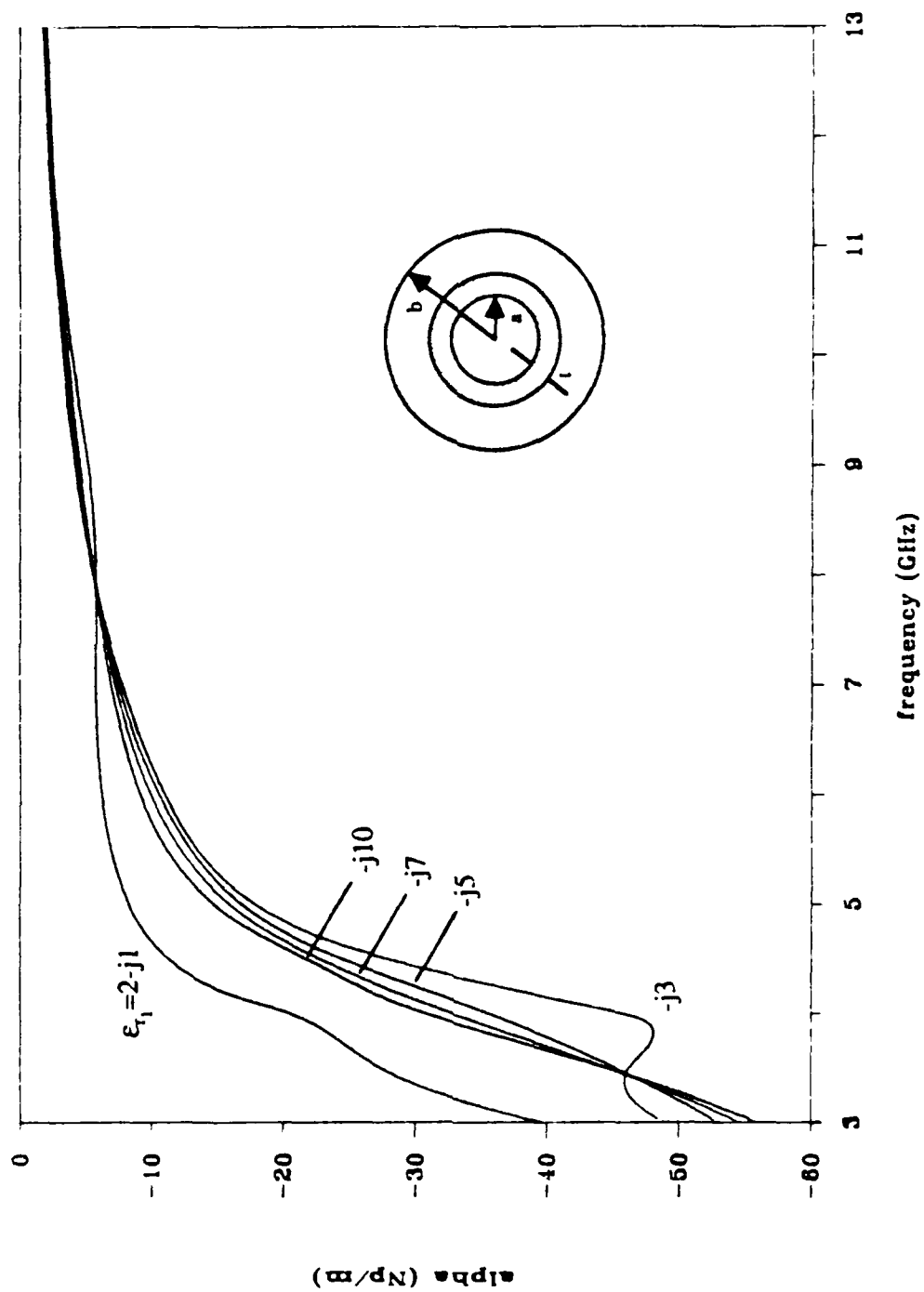


Figure 4.21. Traces of  $\alpha$  versus frequency for the  $EH_{11}$  mode in the three-dielectric guide having  $a=0.4909$  in,  $b=2.005$  in,  $t=0.2$  in,  $\epsilon_{r1}'=2$ ,  $\epsilon_{r1}''=2.7-j2$  and  $\epsilon_{r3}=1$ , with  $\epsilon_{r1}''$  as parameter.

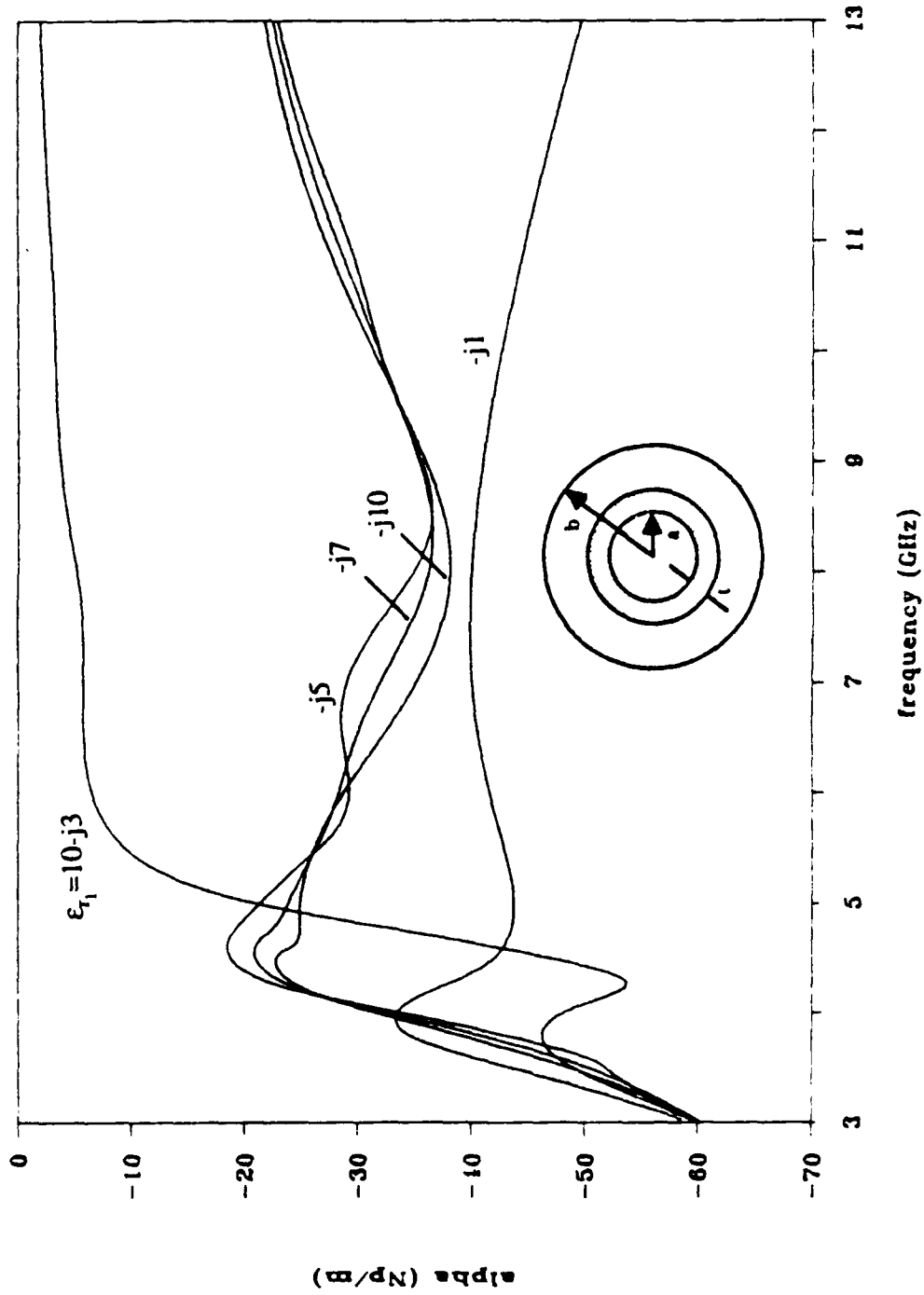


Figure 4.22. Traces of  $\alpha$  versus frequency for the  $EH_{11}$  mode in the three-dielectric guide having  $a=0.4909$  in,  $b=2.005$  in,  $t=0.2$  in,  $\epsilon'_{r1}=10$ ,  $\epsilon'_{r2}=2.7-j2$  and  $\epsilon_{r3}=1$ , with  $\epsilon''_{r1}$  as parameter.

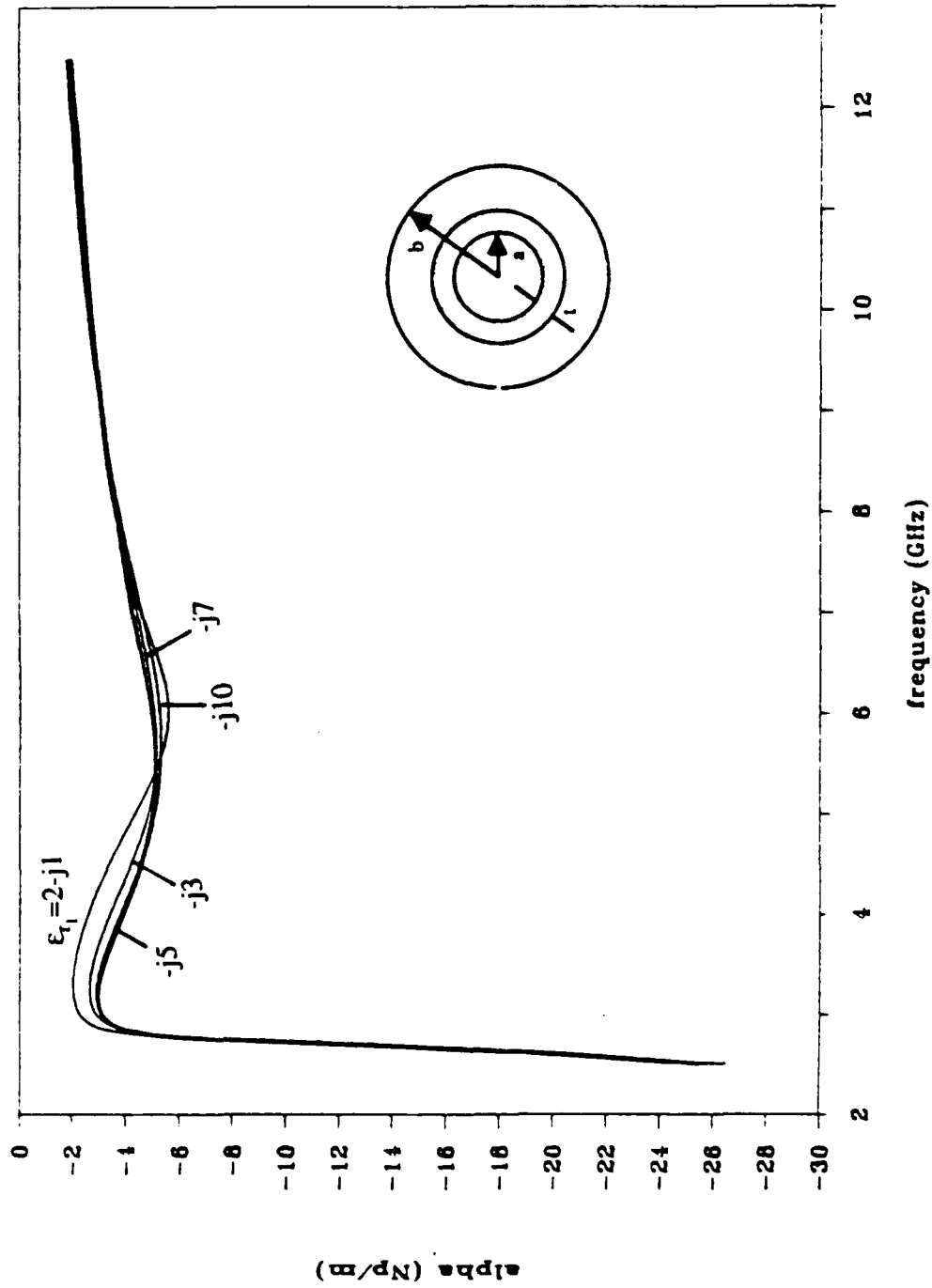


Figure 4.23. Traces of  $\alpha$  versus frequency for the  $HE_{21}$  mode in the three-dielectric guide having  $a=0.4909$  in,  $b=2.005$  in,  $t=0.2$  in,  $\epsilon_{r1}'=2$ ,  $\epsilon_{r2}=2.7-j2$  and  $\epsilon_{r3}=1$ , with  $\epsilon_{r1}''$  as parameter.

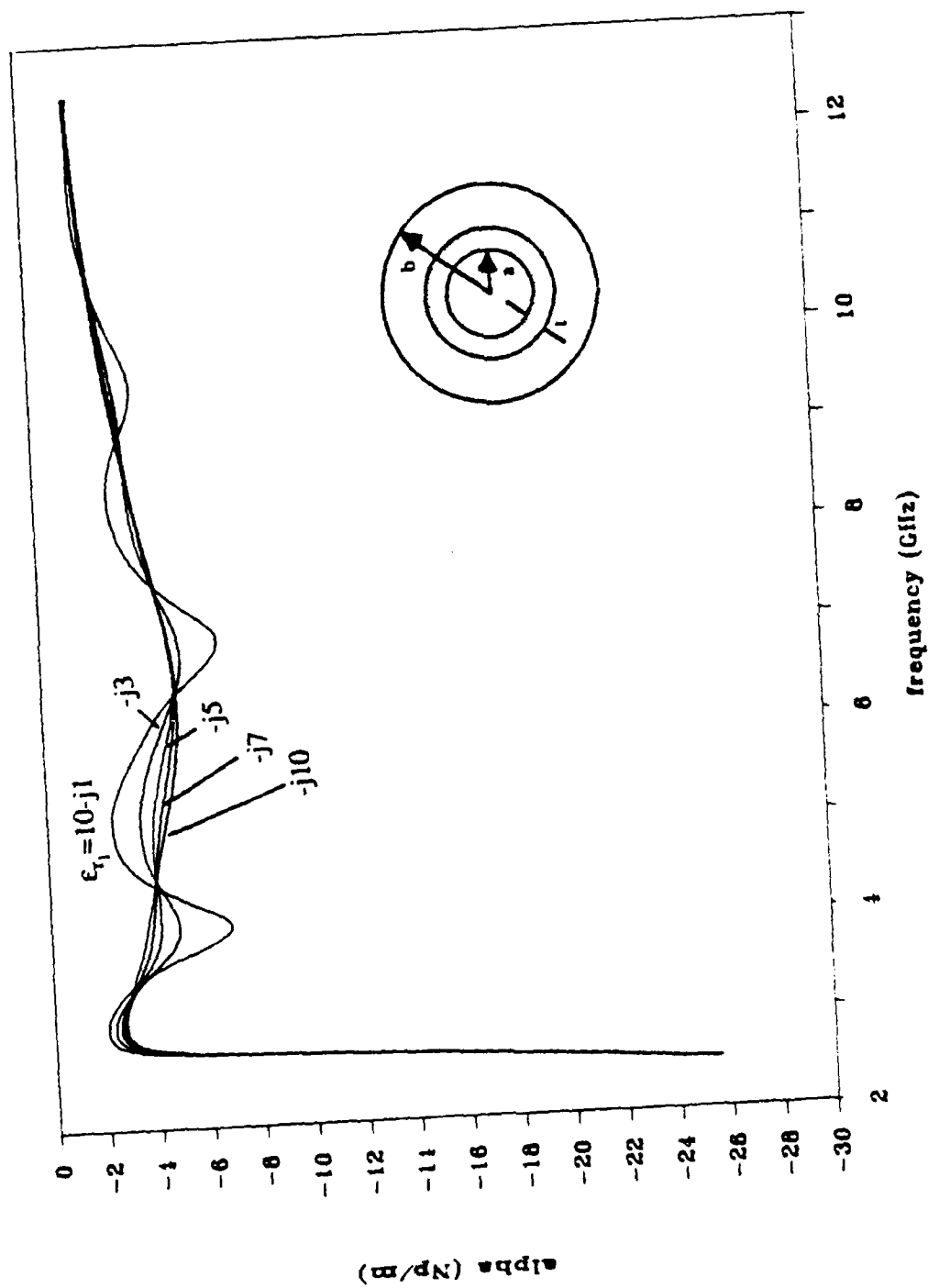
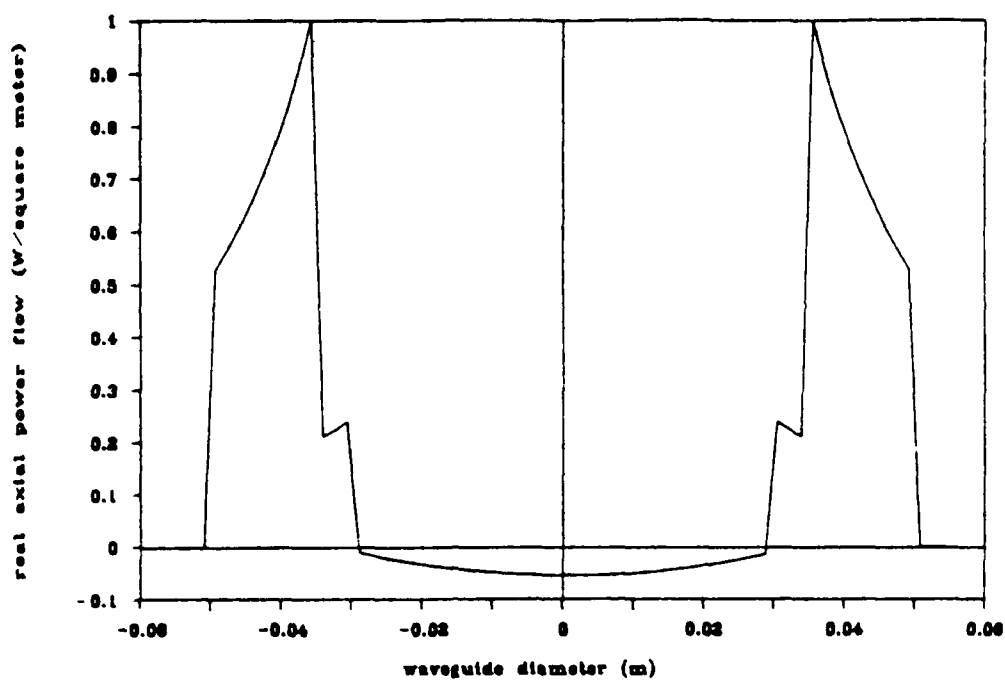
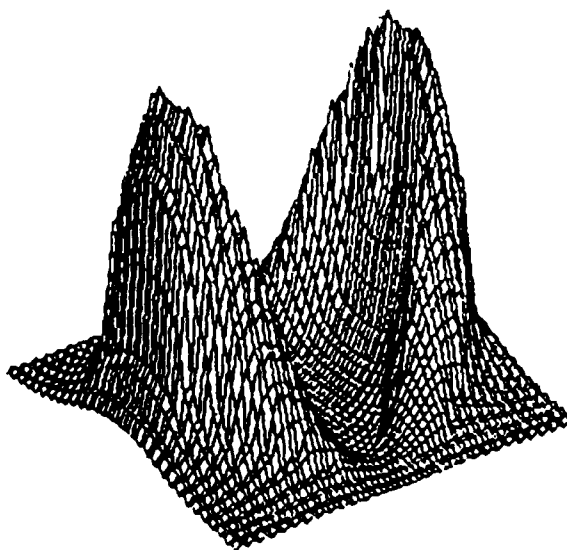


Figure 4.24. Traces of  $\alpha$  versus frequency for the  $HE_{21}$  mode in the three-dielectric guide having  $a=0.4909$  in,  $b=2.005$  in,  $t=0.2$  in,  $\epsilon_{r1}'=10$ ,  $\epsilon_{r2}=2.7-j2$  and  $\epsilon_{r3}=1$ , with  $\epsilon_{r1}''$  as parameter.



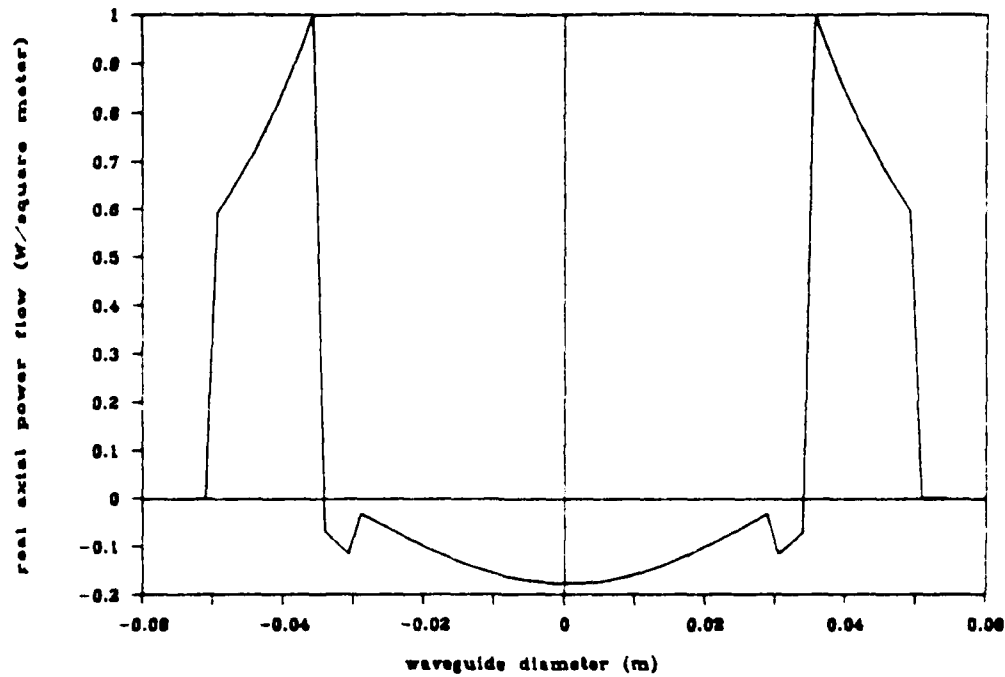


(a)

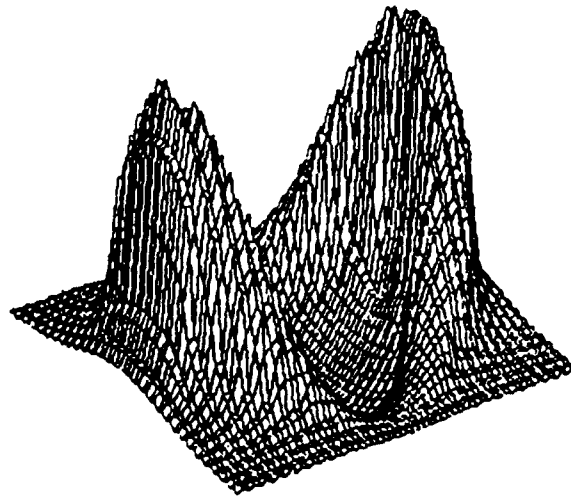


(b)

Figure 4.25. Axial real power flow of the  $HE_{11}$  mode (a) in the  $\phi=0$  plane and, (b) 3-D, for point A in the  $k_z$  trace of Figure 4.13 having  $a/b=0.6$ ,  $b=2.005$  in,  $f=1$  GHz,  $\epsilon_{r1}=2-j10$ ,  $\epsilon_{r2}=2.7-j2$  and  $\epsilon_{r3}=1$ .

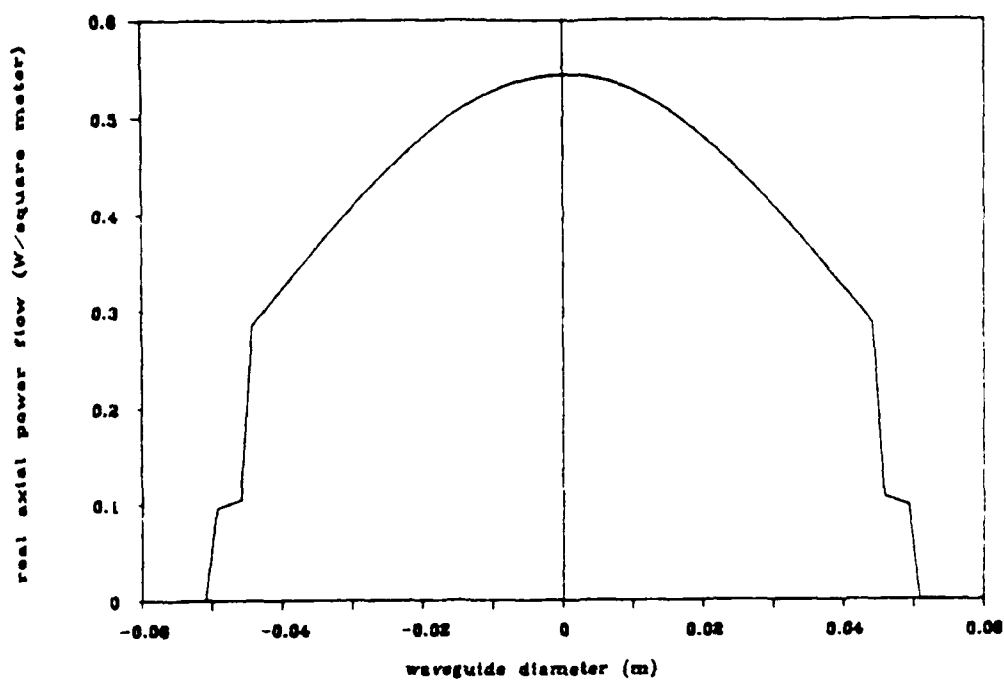


(a)

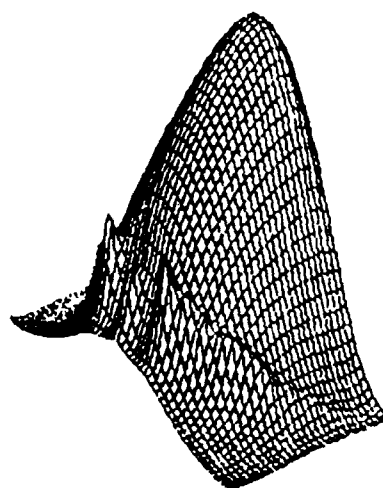


(b)

Figure 4.26. Axial real power flow of the  $HE_{11}$  mode (a) in the  $\phi=0$  plane and, (b) 3-D, for point B in the  $k_z$  trace of Figure 4.13 having  $a/b=0.6$ ,  $b=2.005$  in,  $f=1$  GHz,  $\epsilon_{r1}=2-j1$ ,  $\epsilon_{r2}=2.7-j2$  and  $\epsilon_{r3}=1$ .



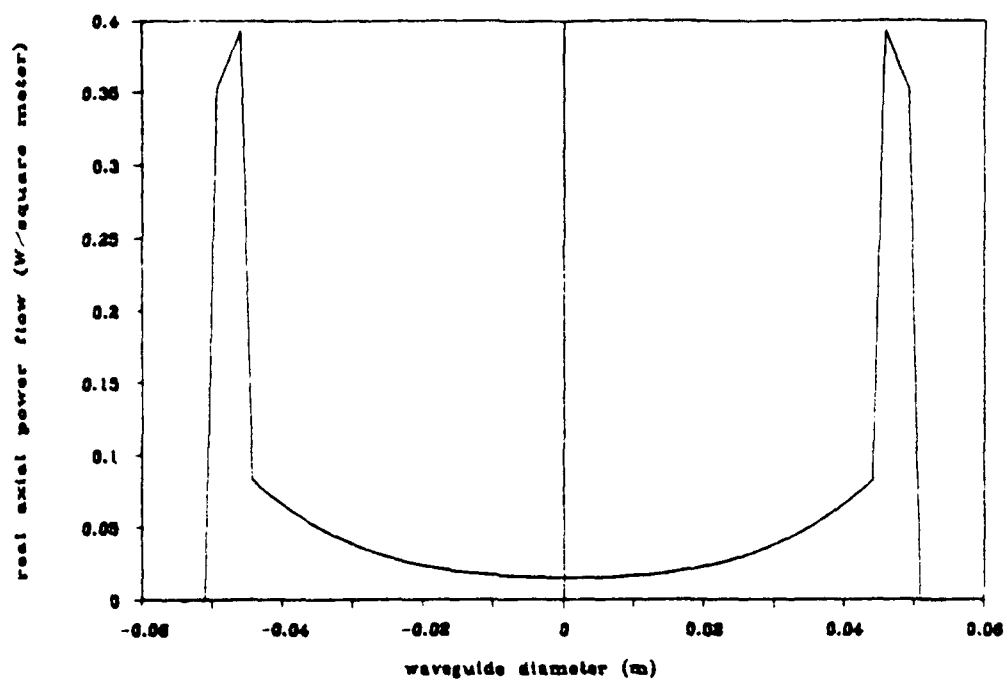
(a)



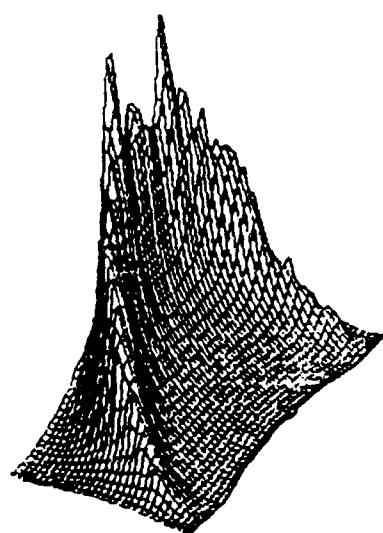
other half of power-flow plot symmetric

(b)

Figure 4.27. Axial real power flow of the HE<sub>11</sub> mode (a) in the  $\phi=0$  plane and, (b) 3-D, for point C in the  $k_z$  trace of Figure 4.13 having  $a/b=0.88$ ,  $b=2.005$  in,  $f=1$  GHz,  $\epsilon_{r1}=2-j1$ ,  $\epsilon_{r2}=2.7-j2$  and  $\epsilon_{r3}=1$ .



(a)



other half of power-  
flow plot symmetric

(b)

Figure 4.28. Axial real power flow of the  $HE_{11}$  mode (a) in the  $\psi=0$  plane and, (b) 3-D, for point D in the  $k_z$  trace of Figure 4.13 having  $a/b=0.88$ ,  $b=2.005$  in,  $f=1$  GHz,  $\epsilon_{r1}=2-j10$ ,  $\epsilon_{r2}=2.7-j2$  and  $\epsilon_{r3}=1$ .

## CHAPTER 5

### EXPERIMENTAL INVESTIGATIONS

The subject matter up to this point has been primarily directed toward the theoretical and numerical aspects of the inhomogeneous circular waveguide and developing an understanding of the principles involved. The emphasis now will be shifted toward the more physical concerns of this problem and the experimental investigations. The purpose of this laboratory work is to see how well the theoretical models and methods used in this development match the physical phenomenon. This also provides a verification for the accuracy of the computer programs developed and written for this project in addition to their utility.

Two very different experimental techniques were devised and used in these measurements. One is a resonant cavity technique which proved very useful for investigations with near lossless materials. The second technique is a finite open-ended waveguide method which is much harder to model theoretically but is useful for lossy and very lossy materials. A major problem encountered in analyzing these experiments was not having accurate values for the permittivities of the loading materials. This made analytical verification difficult but not impossible as additional boundary conditions which appeal to logical argument made predicted permittivities for a select number of materials reasonable.

The finite open-ended waveguide measurements have an additional appeal in that they are also used in the shielding measurements discussed in Chapter 1. In Section 5.4, the results of the attenuation measurements for this arrangement will be seen well modelled by infinite waveguides of identical cross section. This is encouraging for further justification of the use of these programs. However, the use of these codes is limited to explaining measured results. Their use as predictive tools is highly questionable.

### 5.1 Resonant Cavity Method Justification

One technique for measuring the properties of the dielectrically-loaded infinite waveguide is with a resonant cavity [11]. At first glance, the finite, bounded geometry of the cavity may seem far from that of the infinite waveguide. However, the inclusion of end plates on the waveguide does not affect the separability of the geometry inside the cavity. That is, the interior of the cavity remains a separable geometry and the interior fields can be found by using separation of variables as in Chapter 2. Since one would now expect the waves to be traveling back and forth in the cavity and not propagating in only one direction, the choice of  $e^{-jk_z z}$  for the  $z$  variation must be replaced. The choice of

$$h(k_z z) = \sin(k_z z) \text{ or } \cos(k_z z) \quad (5.1)$$

allows for all the transverse electric fields to meet the zero field boundary condition at both pec end plates. Therefore, for zero tangential fields ( $E_p$  and  $E_\phi$ ) at  $z=0$  and  $L$ , the length of the cavity, from Equations (2.5) and (2.6)

$$\begin{aligned} \sin(k_z L) &= 0 \quad \Rightarrow \\ k_z &= \frac{p\pi}{L} \quad p = 0, \pm 1, \pm 2, \dots \end{aligned} \quad (5.2)$$

In order to satisfy this boundedness criterion in the  $z$  direction, another free parameter (either  $\omega$ ,  $\mu$  or  $\epsilon$ ) must be fixed. Using (2.12), assuming  $\mu$  and  $\epsilon$  are known, the resonant frequencies can be fixed for each  $p$ , thus enforcing (5.2). This is in contrast to the waveguide problem where the frequency is given and the  $k_z$  determined. This implies that

solutions to the resonant cavity problem must be found in a different manner than for a waveguide of similar cross section.

With the geometry separable, the dispersion relation given in Equation (2.12) remains valid for the interior of the cavity. Plots of the dispersion relations for both the homogeneous and inhomogeneous waveguides considered earlier are contained in Figure 3.10. The methods for determining these plots in those two cases are dramatically different, but, nonetheless, they are both graphical depictions of the dispersion relations. If metal end caps are placed perpendicular to the guide axis at any two points along  $z$ , a resonant cavity is formed for which the fields still obey the same dispersion relation as the guide fields. The additional boundary condition in (5.2) forces a discretization of these dispersion graphs so  $k_z$  assumes only discrete values spaced uniformly by  $\pi/L$  starting at  $k_z=0$ . Using the *same* dispersion relation for the cavity as for the infinite guide, the resonant frequency for a particular mode can be found through this functional relation of  $k_z$  and  $\omega$ . Therefore, the formulation of the infinite waveguide can be experimentally tested and verified in the laboratory with a resonant cavity! The major benefit of a resonant cavity is that a bounded and controlled environment is provided for more accurate laboratory measurements.

## 5.2 Resonant Cavity Measurements

The resonant cavity used in the laboratory measurements was fabricated from aluminum with the interior dimensions given in Figure 5.1. With the excitation and measuring probes located in the centers of the circular end caps, the  $TM_{0x}$  modes are excited [32]. Although the  $TM_{01}$  mode is not fundamental to the guide, these azimuthally symmetric modes are easy to excite and prove very stable in the sense that small radial variations in the probe dimensions do not excite other spurious modes. The inside of the cavity is approximately 3.7 in in diameter and 5.2 in in length. The measurements

performed in the laboratory were for the three-dielectric case: a hose filled with some material. The hose was suspended concentrically along the cavity axis with two styrofoam rings of approximately 1/4 to 1/2 in thickness. It was determined by measuring a number of resonant frequencies for the cavity, both empty and with the styrofoam, that the rings provided less than a 0.1% change in the center frequency of the resonance,  $f_c$ , implying the styrofoam's dielectric constant is near that of air. The loss due to the rings was also small, since  $\Delta f_{3dB}$  increased only slightly. The measurements of the cavity  $Q$  ( $f_c/\Delta f_{3dB}$ ) were a source of great difficulty. The primary reason for this was the lack of repeatability in the  $\Delta f_{3dB}$  measurements from one setup of the cavity to the next and from one day to the next. Since with this cavity method the  $f_c$  measurements were very consistent, the dielectric losses, which can be derived from the  $Q$ , were measured by a different, more repeatable method to be discussed in Section 5.4.

The excitation and measuring probes in the cavity were straight, 32 gauge wires protruding into the cavity 0.13 in from the end cap. From trial-and-error measurements, both the diameter and length of wire proved to be critical in two respects. One, too large a diameter or length will perturb the geometry of the system excessively and large deviations from the simple end-plate boundary conditions ( $E_\rho = E_\phi = 0$ ) become evident in the smoothed resonant peaks. Two, for a probe too short, the coupling to the fields becomes too small and the resonances are lost in the noise.

The source of excitation for the cavity was a Wiltron 6637A signal sweep generator. To measure the resonances, a Wiltron 560A scalar network analyzer was connected to the cavity output through type-N connectors. Figure 5.2 shows the output from the network analyzer for the arrangement of an empty 0.46 in inner diameter cpvc hose of thickness 0.0825 in with the frequency swept from 2 to 10 GHz. The resonant peaks are quite prominent above the noise level near -65 dB. These resonances are all associated with azimuthally symmetric TM modes. The first peak, the  $TM_{010}$  resonance near 2.3 GHz, corresponds to the cutoff frequency of the  $TM_{01}$  mode in an infinite



waveguide of similar cross section. The loaded  $Q$ 's for these lower-order resonances range from a low of approximately 300 to a high near 1100. The next higher mode, the  $TM_{02}$  in the infinite guide, is first seen in the stepped region near 5 GHz, and the  $TM_{03}$  resonances begin near 8 GHz in the next stepped region. Justification for these designations will become evident shortly when theoretically predicted resonances are compared with these results.

When the hose is filled with a silicone sealant (Dow Corning 732), the resonances in Figure 5.3 result. All the peaks experience a significant downward shift in frequency, but the higher-order  $TM_{02}$  and  $TM_{03}$  resonances undergo the greatest amount. A comparison of the resonant peaks for the above two cases plus those of the empty cavity is shown in Figure 5.4. Although the permittivities of the cpvc and silicone sealant are relatively small (near 3.4 and 2.4 F/m, respectively) there is a large downward shift in the peaks as shown in the figure. Figures 5.5 and 5.6 show the resonant peaks of the same cavity arrangement but having a 3/4 in cpvc hose of inner diameter 0.697 in and 0.09 in thickness, both empty and filled with the sealant, respectively. The  $TM_{01}$  resonances of the empty 3/4 in hose case occur lower in frequency than do the corresponding ones of the 1/2 in hose case. Curiously, for both the  $TM_{02}$  and  $TM_{03}$  modes, the peaks are higher in frequency for the 3/4 in hose than for the 1/2 in one. When the hose is filled with the sealant, however, all the resonances of the 3/4 in hose, including the higher-order modes, occur at much lower frequencies than the corresponding resonances of the 1/2 in hose. All graphs of the resonant responses shown here confirm that the density of the resonant peaks increases with increasing frequency, making it quite difficult to distinguish the individual peaks of the higher-order resonances.

### 5.3 Theoretically Predicted Resonances

Comparison of the measured cavity resonant frequencies with the theoretically calculated ones is a straightforward process. As discussed in Section 5.1, the  $k_z$ - $\omega$  plot for the infinite waveguide is constructed, then the appropriate resonant frequencies of the cavity are obtained by the discretization of the axial wavenumber into its allowed eigenvalues. This process assumes known constitutive parameters. In reality, the  $\epsilon_r$ 's were unknown for the materials used in the laboratory. These parameters can be measured of course, but due to a lack of proper equipment, this was not possible. One way to get around this stumbling block and find an approximate  $\epsilon_r$  is to assume a value, and if many calculated resonant frequencies can be made to match laboratory measured values, then one may assume, with some degree of certainty, that the  $\epsilon_r$  is indeed the correct parameter. One difficulty in this is that if the materials are dispersive, as most are in the microwave region, the  $\epsilon_r$  would need to be continuously varied in many small frequency bands to accurately model the behavior. Since these bands are unknown to begin with, it is not possible to accurately model dispersive materials using this method. Another difficulty is that the materials must be relatively loss-free since this peak-matching method is unique, or nearly so, only in the loss-free case. Therefore, it will be assumed here that the materials are lossless and nondispersive.

For the cpvc hose, Fink and Christiansen [33] give a value of 3.4 F/m for the dielectric constant at 1 GHz and  $\tan \delta = 0.006$ . Using this value for the dielectric constant across the entire 1 to 10 GHz band, the predicted resonant frequencies were calculated from the  $\beta$ - $\omega$  plots for both the empty 1/2 and 3/4 in lossless cpvc hoses. Excellent agreement was realized considering for 32 peaks which clearly matched the theoretical and experimental results, there was an average error of less than 1% and a maximum error of 2.1%. For the filled hose, no data for the permittivity were available on the silicone sealant although Dow Corning has stated that  $\epsilon_r = 2.8$  F/m with  $\tan \delta = 0.0015$  at 100 kHz [34].

Using the heuristic peak matching method, a value of 2.4 F/m for the dielectric constant was arrived at for the sealant. The  $TM_{01}$ ,  $TM_{02}$  and  $TM_{03}$   $k_z$ - $\omega$  plots for the 1/2 and 3/4 in cpvc pipes filled with a material of  $\epsilon_r=2.4$  F/m are given in Figure 5.7. For 29 peaks which matched, there was again an average error of less than 1% and a maximum error of 2.1% with the measured values. A selected sample of values for these two sets of comparisons is listed in Table 5.1. More than likely, the permittivities are not exactly 2.4 F/m for the sealant and 3.4 F/m for the cpvc since it was required they be lossless and nondispersive. However, it is probable that the permittivities are very near those given above since this additional boundary condition based on the logical argument of matching many resonances was met exceptionally well.

Finally, the resonant cavity technique inherently assumes a low-loss material(s) within the cavity. Too high a loss will not allow the cavity to resonate since by the time the wave traverses the length of the cavity twice, the signal is too weak to contribute to the resonance effect. Measurements on methanol, tap water and glycerin (all very lossy) gave the same results—the measured output was completely devoid of resonant peaks. (A typical example of this is shown in Figure 5.8 for the 1/2 in cpvc hose filled with methanol in the cavity.) Other techniques are needed to measure the loss effects. One method that gave surprisingly good results was the finite waveguide excited by horn antennas to be discussed next.

#### 5.4 Finite Open-Ended Waveguide Measurements

To overcome the inherent shortcomings of the cavity-resonator technique's inability to measure attenuation for very lossy dielectrics, a finite-waveguide technique was employed. A small section of guide was attached to a panel on a shielded enclosure, as depicted in Figure 5.9, and illuminated by a horn antenna. (A more detailed description of this type of general experimental arrangement is given in [35].) The wave attenuation

provided by the guide can be measured with regard to a set of reference measurements performed with the two antennas in free space. This is a total attenuation from all sources including diffraction, reflection and wall and dielectric losses. The antenna gains and system losses are assumed removed by the reference subtraction. To approximate the losses due only to the loading dielectrics, a new reference level can be chosen, namely, the total guide setup with the empty hose. Then upon subtraction of this reference level from the guide measurements with the filled hose, the diffraction and reflection losses will be subtracted in addition to the system and antenna losses. This is an approximation since the fields, in addition to reflection from the inner filling, will be redistributed in the guide from the empty to filled hose cases. Hence, the losses from other sources will be modified. However, if these other sources of loss are considered negligible and the filling material inside the hose the only source of loss, then only this material can contribute to the attenuation once diffraction and reflection are subtracted. To reduce the reflection losses from the inner material (which are not accounted for in this referencing subtraction method), conical-shaped styrofoam plugs were used to help reflect the incident energy down the guide. All these seemingly incredulous assumptions prove quite reasonable for these finite-guide measurements since for one, the guide is only 6 in long so the wall losses are small and two, a Teflon hose ( $\epsilon_r = 2.1 - j0.000315$  F/m at 3 GHz [22]) is used to contain the material and is quite lossless. Two separate examples of these finite guide measurements will be discussed, both of which use methanol (which is very lossy) as the filling inside a Teflon tube.

The first example is for a 3/4 in Teflon hose of inner radius 0.3733 in and thickness 0.1908 in filled with methanol inside a 1.5 in diameter aluminum waveguide of inner radius 0.7425 in and length 6 in. The results of this comparison are shown in Figure 5.10. The measured values given are the results of four measurement cycles to verify the repeatability of the experiment and identify any experimental anomalies such as humidity effects. The calculated attenuation shown in the same figure is for the  $HE_{11}$  mode of a perfect guide of

similar cross section and length. As discussed earlier, this eigensolution method, used for the calculated values, indicates only those modes that can exist and not those that actually do in a physical arrangement. However, these two plots are remarkably similar which strongly suggests the existence of this mode in the guide. The  $TM_{01}$  mode also has an attenuation *versus* frequency graph similar to this one, but azimuthally symmetric modes are not likely to be excited by the incident fields from the pyramidal horn antenna used here. Most likely, there are many modes excited in addition to the  $HE_{11}$ , but here it appears that the major behavior of the attenuation is dictated by the  $HE_{11}$  modal properties alone.

As was the case with other materials, the permittivity values for the methanol are primarily unknown; however, von Hippel [22] lists these three values

$$\begin{array}{ll} \epsilon_r = 30.9 - j2.472 \text{ F/m} & \text{at } 0.3 \text{ GHz} \\ \epsilon_r = 23.9 - j15.296 \text{ F/m} & \text{at } 3.0 \text{ GHz} \\ \epsilon_r = 8.9 - j7.209 \text{ F/m} & \text{at } 10.0 \text{ GHz} \end{array}$$

Linear interpolation was used between these known values and is shown pictorially in Figure 5.11. The use of interpolation here is a bit presumptive since the real and imaginary parts of the permittivity cannot be chosen independently. These quantities are related through the Kramers-Kronig equations which specify their unique behavior for proper satisfaction of the causality principle [36], [37], [38].

Even with this series of rough assumptions, the agreement between the theoretically calculated attenuation for the methanol and the measured values is remarkable. Both predict an almost linear increase in attenuation, on the log scale, as the frequency is increased. For frequency values less than 4.2 GHz, the air-filled reference guide is in cutoff and no comparison can be made.

The second example is with a 4 in diameter guide of radius 2.005 in filled with a 1 in diameter Teflon tube of inner radius 0.5008 in and thickness 0.1908 in. The same measurement referencing method is used here as in the previous case. Excellent agreement is evident again, with the results given in Figure 5.12 for methanol in the Teflon tube. Surprisingly, as the frequency is increased here, the attenuation peaks near 6 GHz and quickly decreases to very small values near 10 GHz. This behavior could not be modelled with only one mode, but when the effects of the  $EH_{11}$  mode were included with those of the  $HE_{11}$ , the results were very close to the measured values. This inclusion of the  $EH_{11}$  mode indicates a strong modal conversion between the  $HE_{11}$  and  $EH_{11}$  modes with the  $EH_{11}$  dominating at higher frequencies. In the midband region where neither mode dominates, the correspondence of measured to predicted values is marginal. This is to be expected since the theoretically calculated values assume a dominance of one mode over all others; clearly, this is not satisfied in the midband region. Also, above 8 GHz the attenuation becomes negative which is not to be expected for this passive system. This behavior is attributed to the out-of-band responses of the pyramidal horn antennas which have single-mode operation only up to 8 GHz.

A number of observations can be made concerning these finite-guide measurements. One, the  $EH_{11}$  mode was needed in the 4 in guide measurements to improve correspondence with measured values but not needed for the 1.5 in guide. Examination of this mode in the small guide showed that the minimum attenuation afforded was near 200 dB in the 1 to 10 GHz band. Clearly, this mode would not noticeably affect the attenuation measurements. When it does dominate as in Figure 5.12, the attenuation trend changes considerably. This introduces the next observation: the attenuation has a negative slope and approaches a small value in the 4-in guide case at higher frequencies. This type of behavior is curious from the standpoint that as the frequency increases, the attenuation from the dielectric losses is decreasing. A question arises as to whether this is reasonable and if it is unique to this physical arrangement. The attenuation as a function of

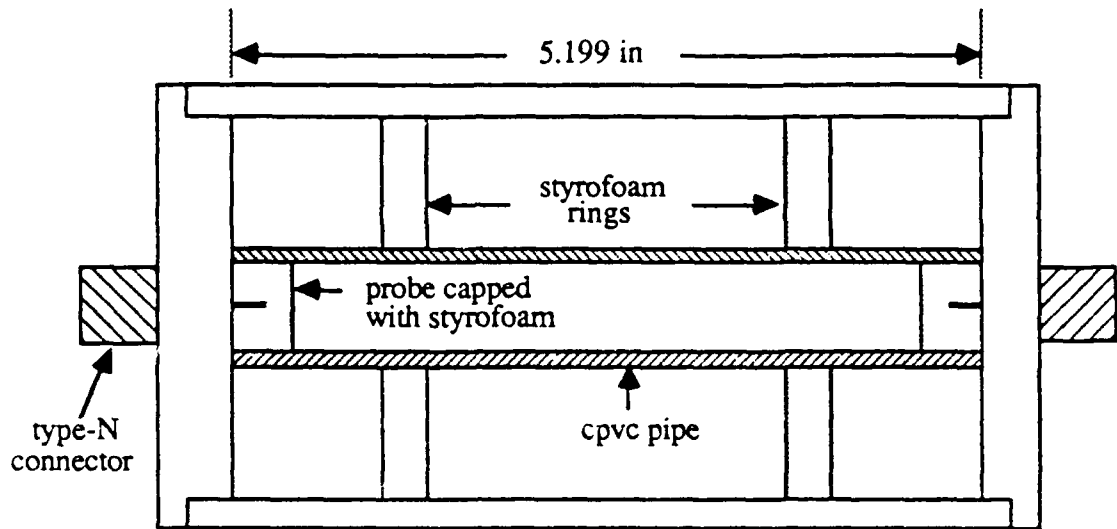
frequency for the *homogeneous* waveguide of varying radius filled with methanol was examined using the linearly interpolated  $\epsilon_r$  values for methanol as shown in Figure 5.11. It was observed that attenuation relationships with frequency for the  $TE_{11}$  and  $TM_{11}$  modes assume similar shapes as in the inhomogeneous guide by appropriate choices of the radius (not necessarily corresponding to either guide), but at much higher attenuation (400-600 dB). However, the negative slope behavior in the high band of the inhomogeneous guide could not be reproduced with the homogeneous guide—the attenuation is always increasing in this band or asymptotically so. Although the conduction losses are decreasing in the methanol with increasing frequency, in the homogeneous guide the losses remain on the rise, while in the inhomogeneous 4-in guide they decrease. This decreasing attenuation with increasing frequency appears to be unique to this inhomogeneous waveguide arrangement.

Table 5.1.

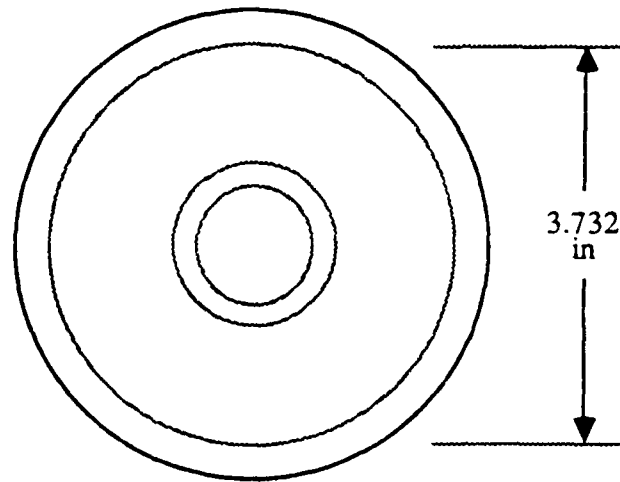
Comparison of the calculated and measured resonant frequencies of the cavity for the 1/2 and 3/4 in cpvc hoses both empty and filled with silicone sealant.

dielectric arrangement		mode	resonant frequencies (GHz)		
			calculated	measured	% error
$\frac{1}{2}$ in hose	empty hose	TM <sub>010</sub>	2.2996	2.313	0.583
		TM <sub>020</sub>	5.1022	5.174	1.407
		TM <sub>030</sub>	8.2070	8.271	0.780
	hose filled with sealant	TM <sub>010</sub>	2.2098	2.215	0.235
		TM <sub>020</sub>	4.7863	4.803	0.349
		TM <sub>030</sub>	7.7988	7.743	-0.715
$\frac{3}{4}$ in hose	empty hose	TM <sub>010</sub>	2.2466	2.293	2.065
		TM <sub>020</sub>	5.1285	5.194	1.277
		TM <sub>030</sub>	8.5003	8.427	-0.862
	hose filled with sealant	TM <sub>010</sub>	2.0704	2.057	-0.647
		TM <sub>020</sub>	4.6700	4.577	-1.991
		TM <sub>030</sub>	7.8297	7.841	0.1443





(a) Side view



(b) End view

Figure 5.1. Geometry and physical arrangement of the resonant cavity filled with the cpvc hose.

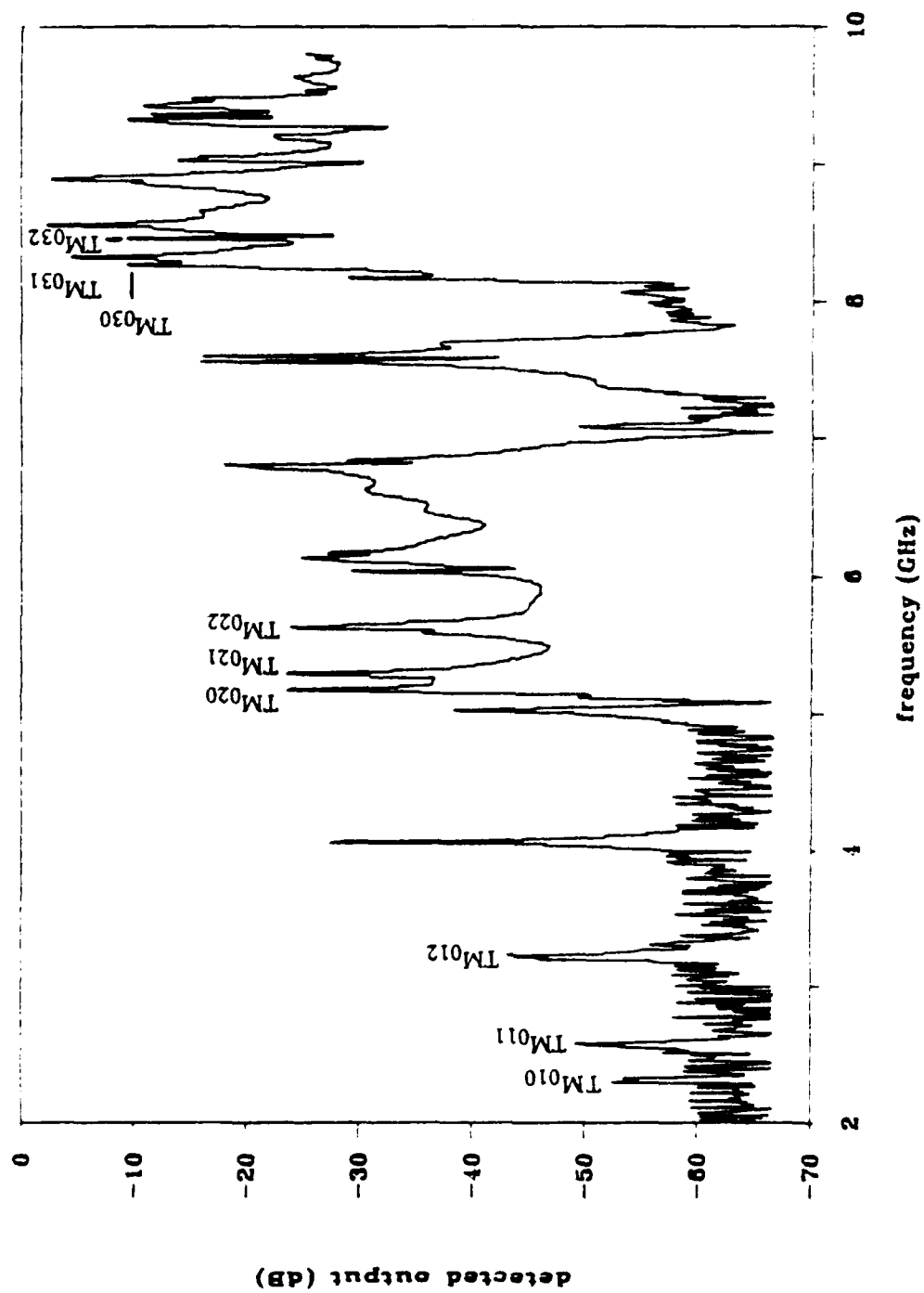


Figure 5.2. Measured cavity resonances when filled with an empty cpvc pipe of inner diameter 0.46 in and thickness 0.0825 in.

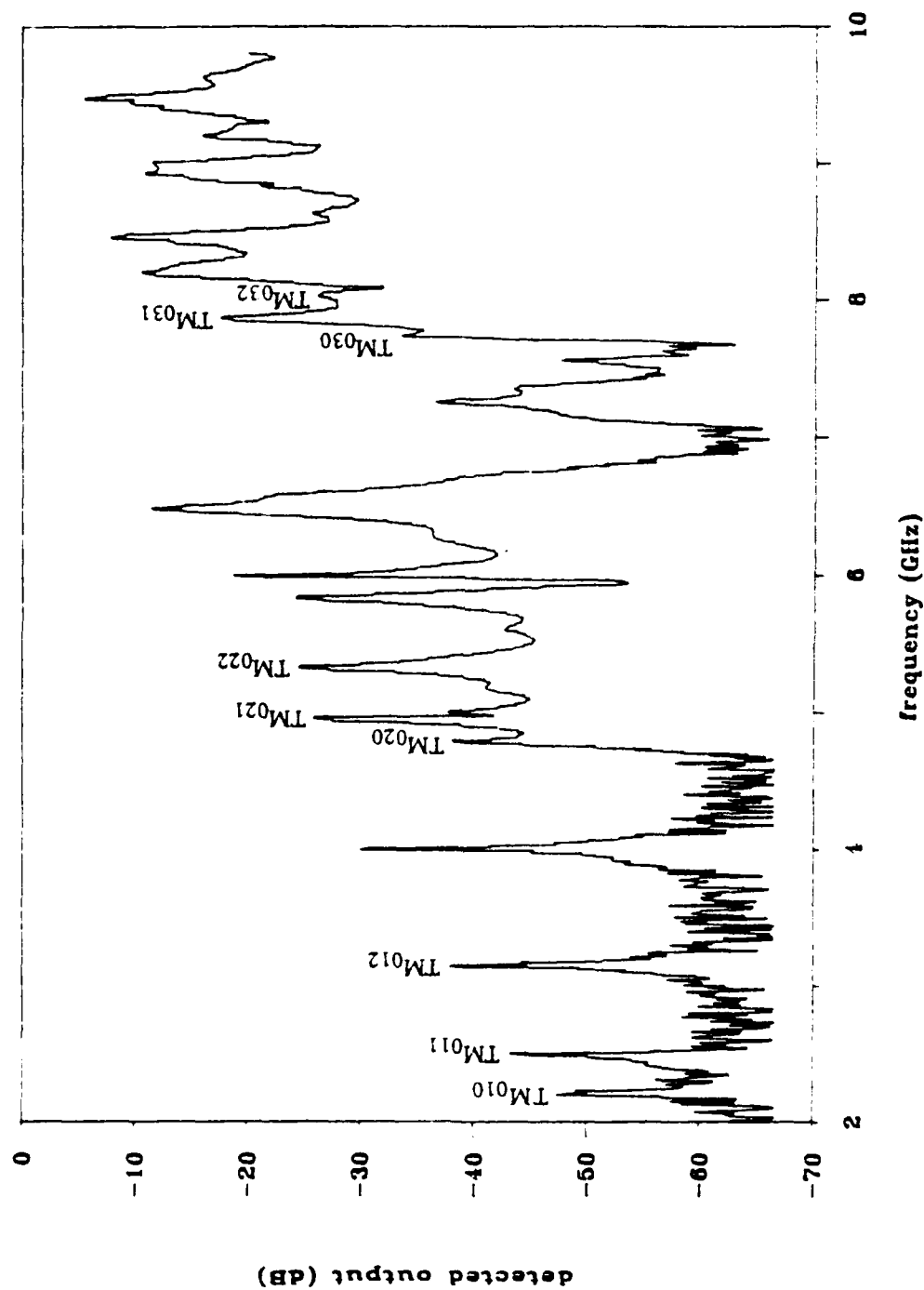


Figure 5.3. Measured resonances of the cavity having the 0.46 in inner diameter cpvc pipe of thickness 0.0825 in filled with the silicone sealant.

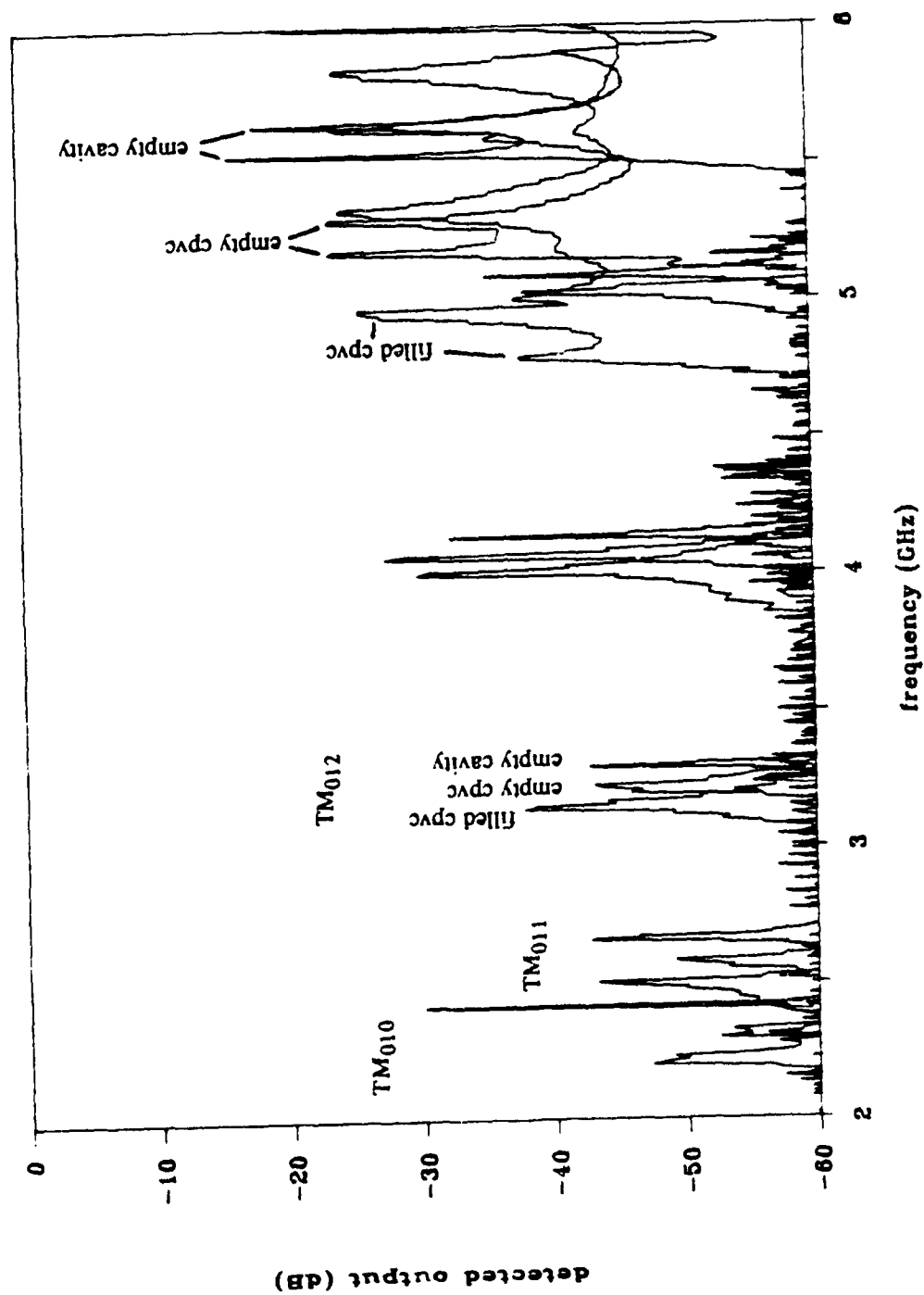


Figure 5.4. Comparison of the measured resonances for the three cases when the cavity is (i) empty, (ii) containing the empty 0.46 in diameter cpvc pipe and (iii) containing the same cpvc pipe filled with the silicone sealant.

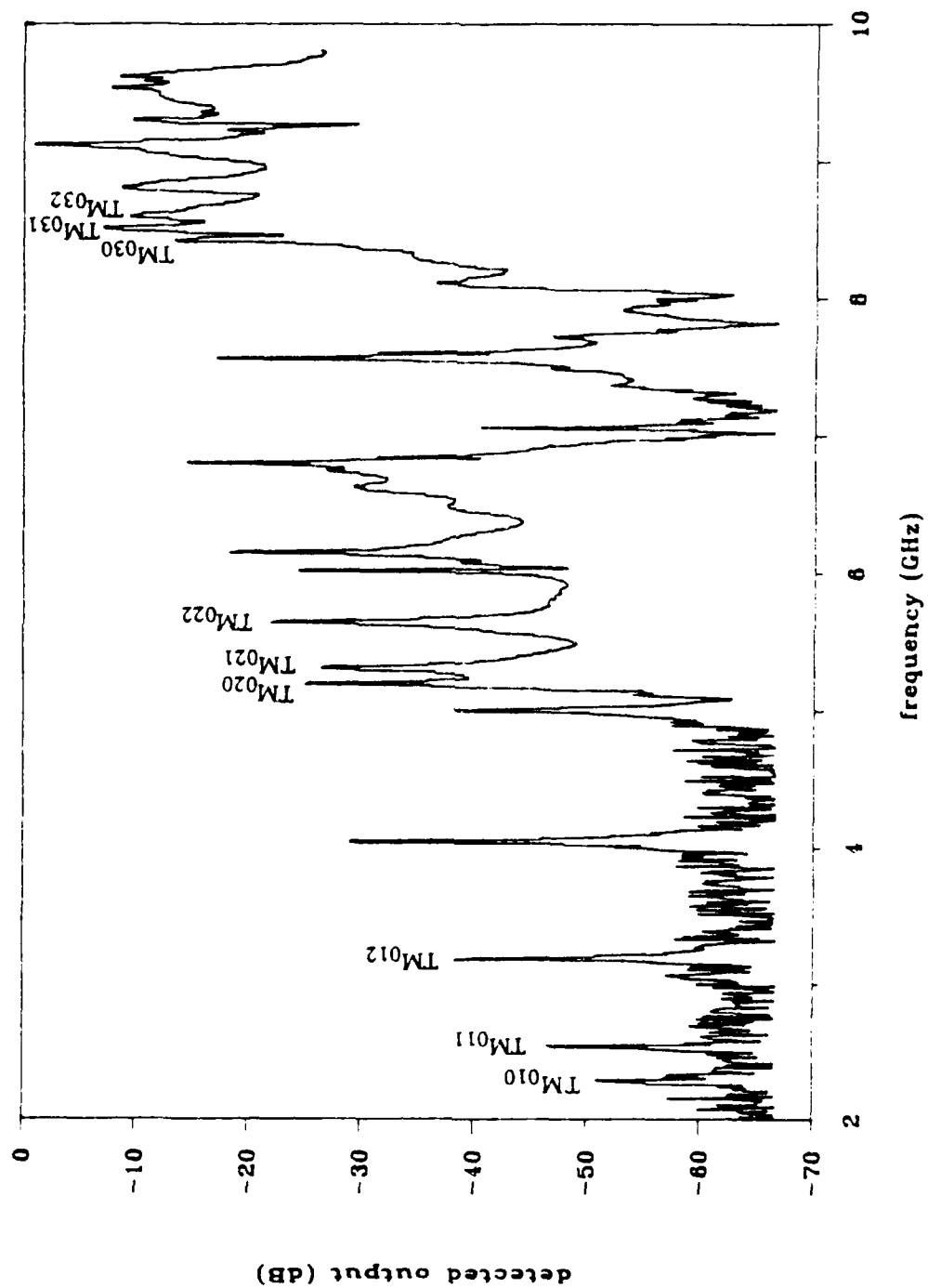


Figure 5.5. Measured cavity resonances when filled with an empty cpvc pipe of inner diameter 0.697 in and thickness 0.09 in.

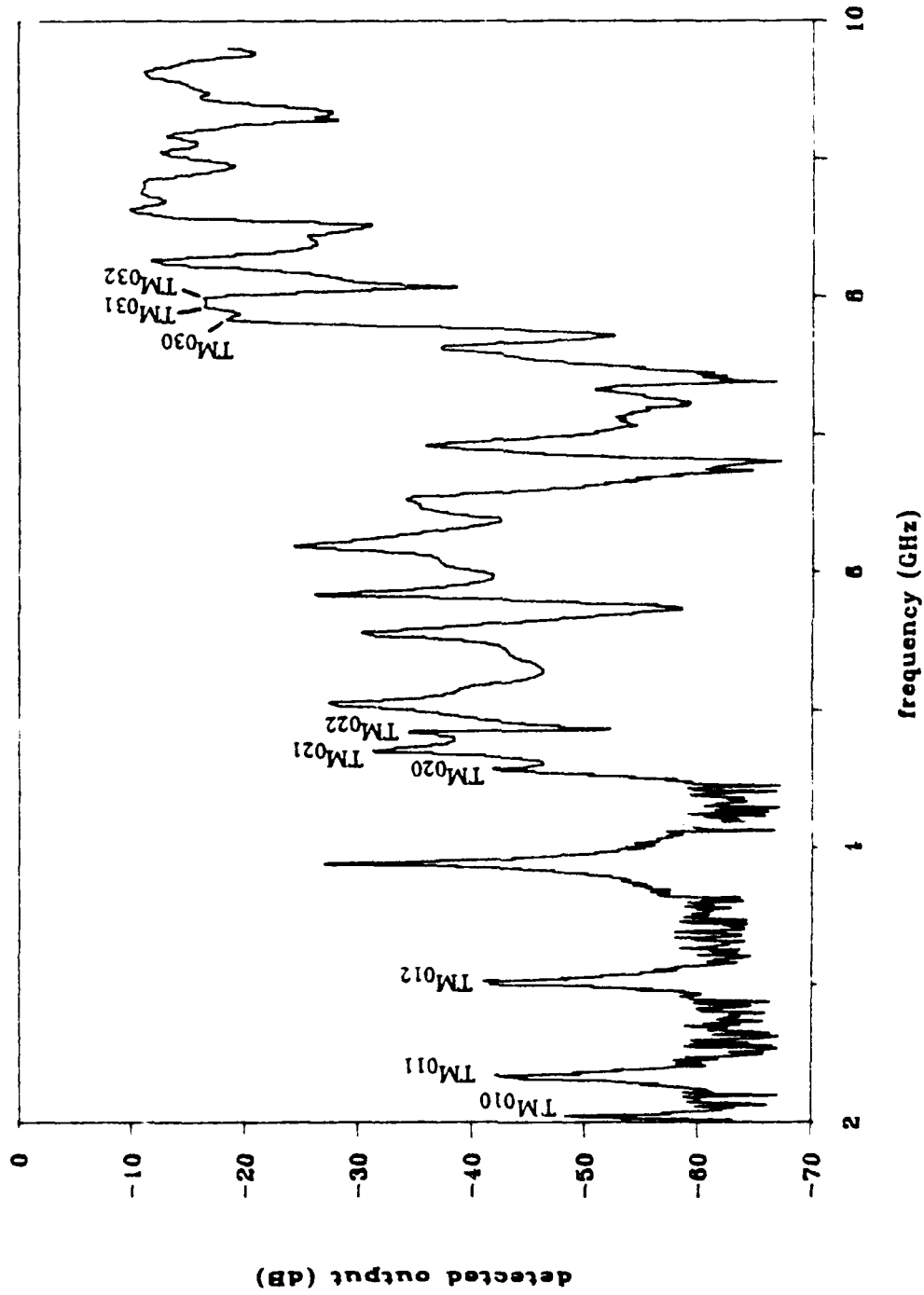


Figure 5.6. Measured resonances of the cavity having the 0.697 in inner diameter cpvc pipe of thickness 0.09 in filled with the silicone sealant.

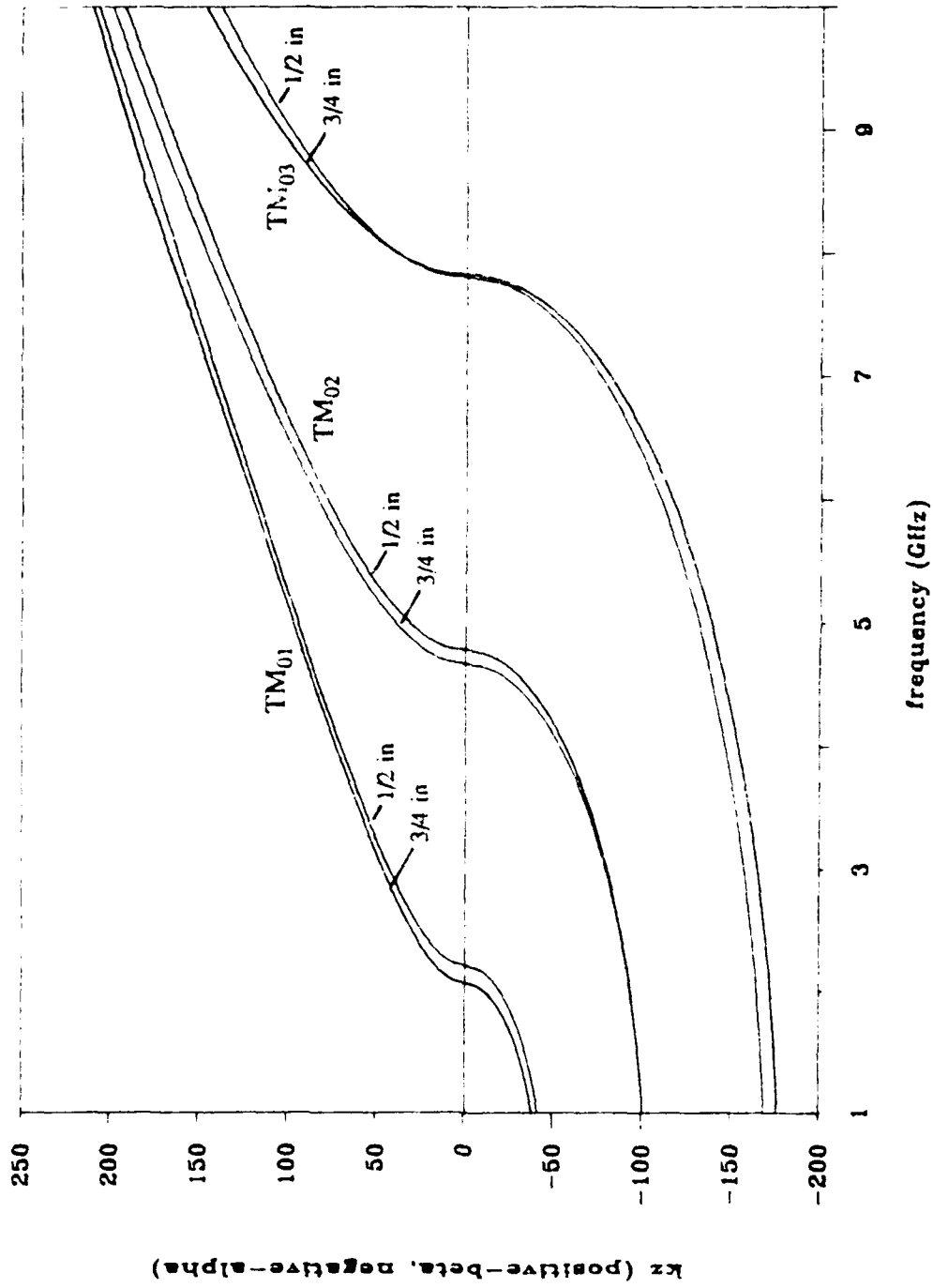


Figure 5.7. Traces of  $k_z$  versus frequency for the  $TM_{01}$ ,  $TM_{02}$  and  $TM_{03}$  modes in a cavity of dimensions given in Figure 5.1, containing either the 1/2 in or 3/4 in cpvc pipe filled with a material of  $\epsilon_r = 2.4$ .

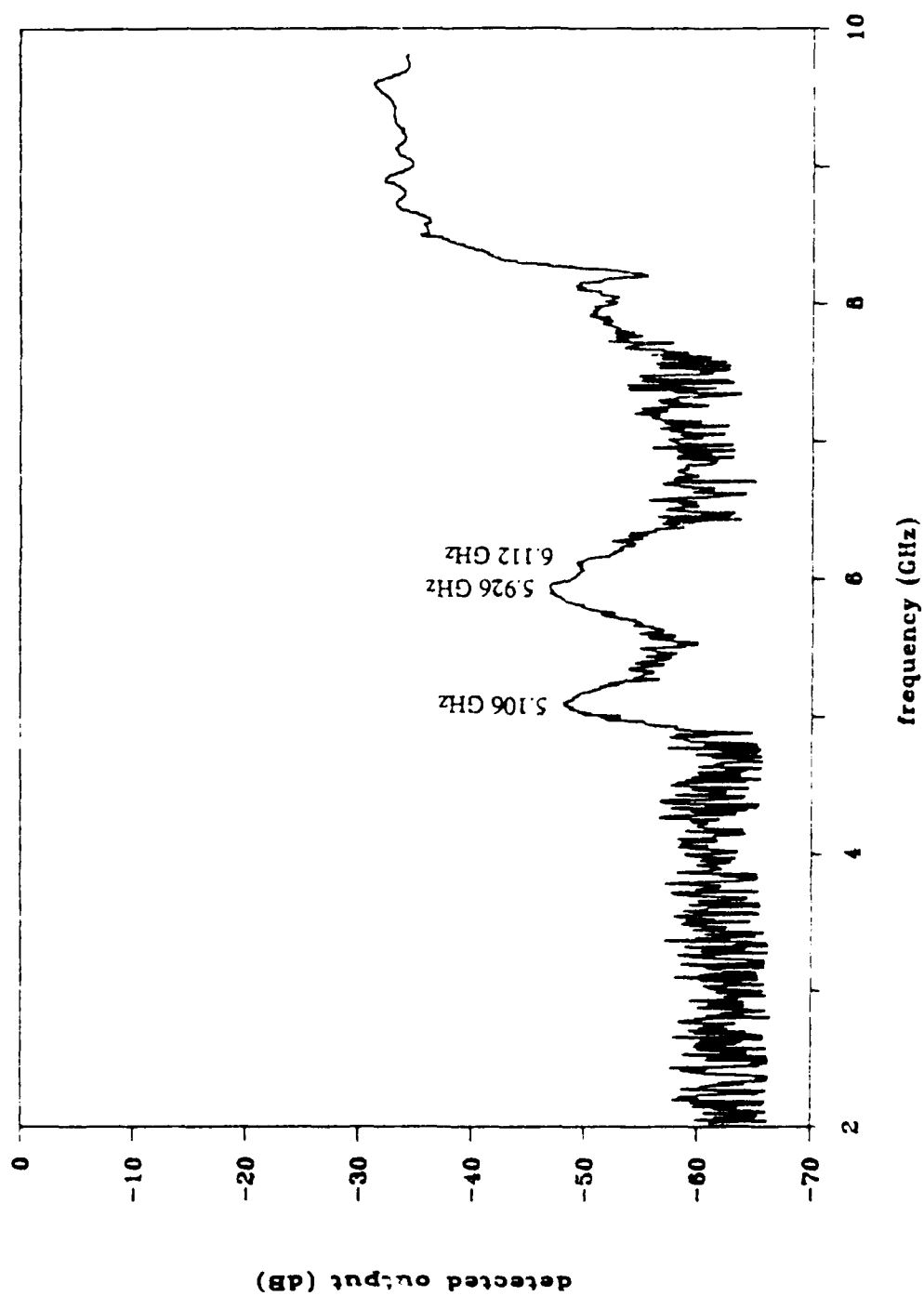


Figure 5.8. Measured output of the cavity having the 0.46 in inner diameter  
cpvc pipe of thickness 0.0825 in filled with methanol.



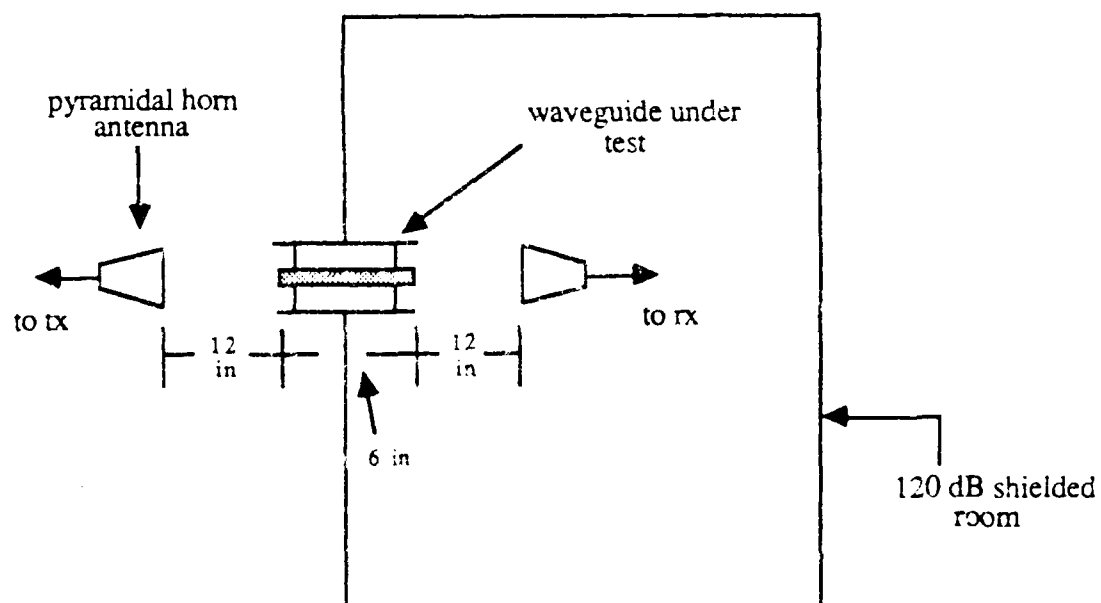


Figure 5.9. Experimental arrangement for the finite-length waveguide measurements on the hose-filled 6 in guide.

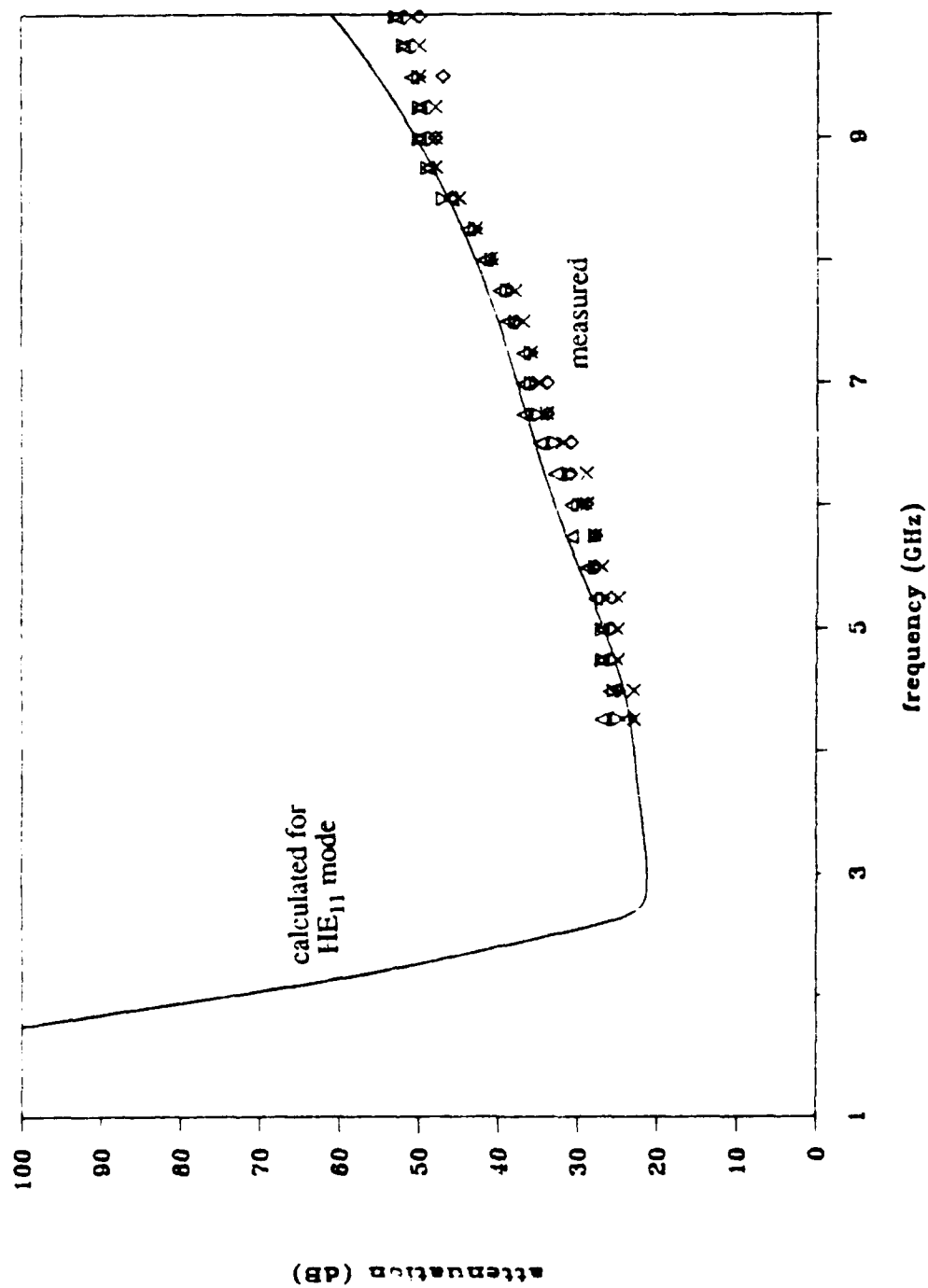


Figure 5.10. Comparison of the theoretical and measured attenuations in the three-dielectric guide of diameter 1.485 in containing a Teflon tube of radius 0.3733 in and thickness 0.1908 in filled with methanol.

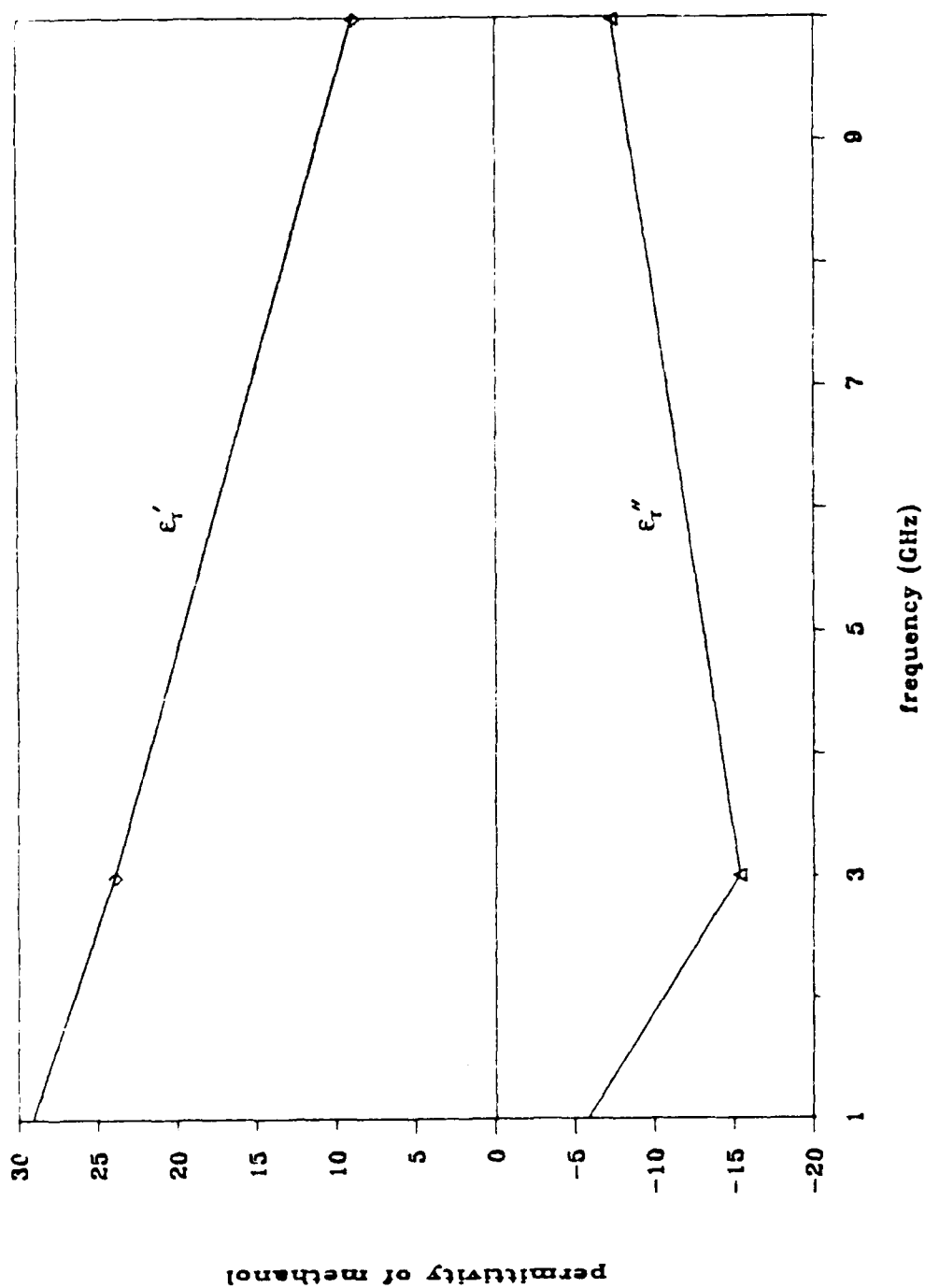


Figure 5.11. Linearly interpolated values for the permittivity of methanol using measured quantities from von Hippel [22].

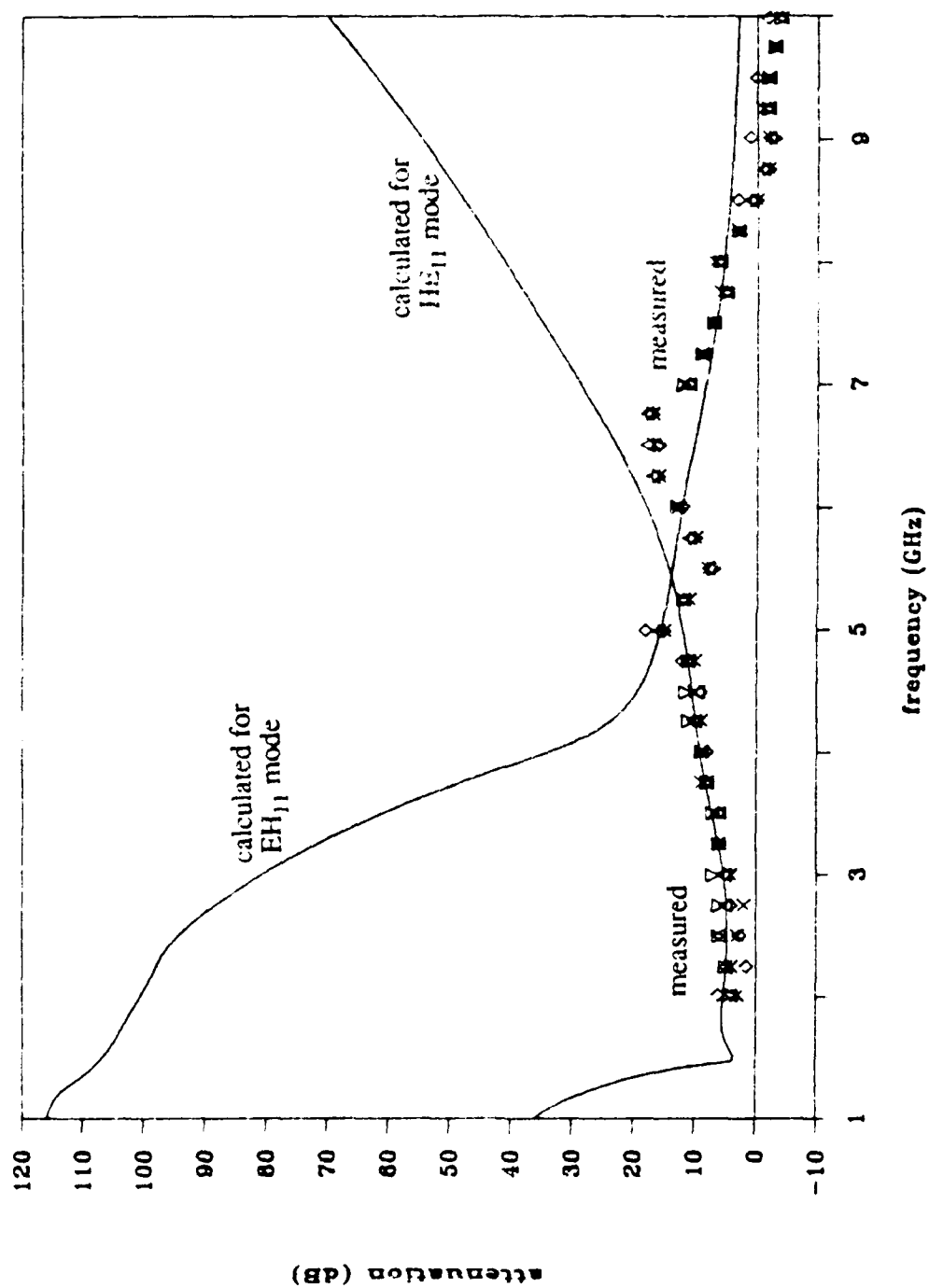


Figure 5.12. Comparison of the theoretical and measured attenuations in the three-dielectric guide of diameter 4.01 in containing a Teflon tube of radius 0.5008 in and thickness 0.1908 in filled with methanol.

## CHAPTER 6

### CONCLUSIONS AND SUGGESTIONS FOR FURTHER STUDY

In this thesis, solutions to the radially inhomogeneous infinite circular waveguide have been obtained numerically from an exact theoretical development beginning with first principles. These inhomogeneous waveguides are layered with circular, concentric annuli having, perhaps, complex constitutive parameters. The modes that were found to exist in these waveguides are hybrid, meaning that they have both axial E- and H-fields. In general, no TE and TM modes are possible in the inhomogeneous guide except for modes with  $n=0$  and all modes for which  $k_z=0$ . The modal designation scheme and modal nomenclature for these hybrid modes have not yet been standardized in the literature. The modal designation technique used in this work takes the homogeneous guide as a limiting case such that as the constitutive parameters of the loading dielectrics approach those of free space or the dielectric radii are increased or decreased until the guide becomes homogeneous, the hybrid modes approach those of the homogeneous guide as

$$HE_{nm} \rightarrow TE_{nm}, \quad EH_{nm} \rightarrow TM_{nm}.$$

By Waldron's Correspondence Idea [19], these hybrid modes have a 1:1 correlation with those of the homogeneous pec guide. Using Waldron's method in conjunction with Snitzer's scheme of modal nomenclature (the sign of  $C_{11}/C_{13}$ ), a unique method of defining the proper modal designation is obtained which is both useful and necessary in the tracing process for  $k_z$ . This tracing process can be complicated by such occurrences as mode traces intersecting other mode traces of similar azimuthal variation and by the development of backward-wave regions in the traces when the permittivities become

sufficiently large in the loading dielectrics relative to the radius of the dielectrics and the waveguide wall.

It was discovered by applying this method of modal designation and nomenclature that a new scheme of naming the backward-wave modes was needed since older methods led to nonphysical results such as unboundedness in the waves and net power flow directed toward the source instead of away in the backward-wave regions, as examples. This new scheme becomes further justified after a small amount of loss is introduced into the loading dielectrics. When this is done, the complex modes are found to be coupled forward and backward waves, as expected from the conservation of energy arguments. After increasing  $a/b$  (or some other physical parameter) to a sufficiently large value, these complex modes decouple into forward and backward waves. As to whether either of the forward and/or backward waves propagate, additional factors must be considered, such as the relative sizes of the  $\epsilon_{r1}$  values and relative dielectric radii. This idea of introducing a small amount of loss to separate the roots is a very useful tool. Here, however, it complicates matters considerably since the complex determinant of a matrix filled with Bessel functions of complex arguments must be computed.

In addition to using dielectric losses as tools for separating roots, these complex constitutive parameters also provide attenuation of the wave which is especially important in shielding applications. In this study, only the attenuation provided by dielectric losses was examined since this was anticipated to be the major source of attenuation in the inhomogeneous guide above cutoff. There was a heavy concentration on the attenuation provided by the lossy three-dielectric guide since this is a good model for the hose through the waveguide-below-cutoff penetration. The results of this investigation showed that contrary to homogeneous guides, there are no simple rules-of-thumb for computing the amount of attenuation the wave suffers in relation to either the amount of dielectric losses or the relative sizes of the dielectric radii. It was concluded that each case must be analyzed separately by tracing out the axial wavenumber as a function of relative dielectric radius or

frequency, as examples. It was also shown that the redistribution of power flow in the dielectrics can vary the attenuation in counterintuitive ways. For example, in one case, even though the losses were increased considerably in the inner region of a three-region waveguide, the attenuation was shown to decrease appreciably.

As a verification of the theoretical formulation and the numerical solutions, two types of experimental measurements were performed. These measurements were separated into those for near lossless dielectrics where a resonant cavity technique was employed and those for lossy materials where the finite guide arrangement for the waveguide-below-cutoff penetration was used. Both gave excellent agreement with the theoretically predicted values. In the finite guide arrangement, a number of speculative assumptions were made concerning the reference measurement subtraction from the complete, loaded waveguide arrangement so that only the losses from the loading material would be observed. This was necessary, since in this study, only the characteristic properties of the waveguide itself were scrutinized and the source properties were not considered.

For future study into this inhomogeneous waveguide topic, an important characteristic of this penetration which deserves considerable attention is this source coupling to the waveguide. By considering the particular source of EM excitation along with the waveguide geometry, the total penetration arrangement could be analyzed such that a determination of the actual wave attenuation, including diffraction and reflection effects, could be calculated in a deterministic fashion rather than identifying excited modes and the corresponding attenuations which have occurred. This would allow for a predictive tool in the analysis of the shielding effectiveness for waveguide penetrations.

As additional study into this phenomenon, actual measured values for the permittivities of the loading dielectrics could be obtained, and using these new values as input to the tracing programs, more accurate comparisons could be performed with the measured field quantities. The additional boundary condition of matching many resonant frequencies applied in this study is logically consistent; however, using actual measured

permittivity values is more appealing since the losses present in the loading dielectrics will have some effect on the resonant frequencies. In addition, materials with dispersive constitutive parameters could be used in both measurement arrangements with a higher degree of accuracy.

Finally, a new precision resonant cavity fabricated from brass, rather than aluminum, would allow for more accurate resonant frequency measurements in addition to repeatable, accurate  $Q$  measurements. From the  $Q$ , another measure of the dielectric losses could be correlated with the theoretical calculations.



## APPENDIX

## MDCW COMPUTER PROGRAM LISTING

The program MDCW is a user interactive computer program for finding the  $k_z$  roots, the resulting field coefficient vector and the transverse fields for a circular waveguide filled with  $q$  concentric, layered dielectrics. Once all the data for each annulus has been entered and three guesses near a root given, the program fills the matrix  $[A]$  in subroutine MTRXVAL. Here, by virtue of Equations (2.20) through (2.23), values are added row-wise to the matrix. These equations contain the  $J_n$  and  $N_n$  Bessel functions which are not trivial to compute, especially for complex arguments. Recursion schemes to calculate these Bessel functions suffer from excessive error corruption if upward recursion is used for more than a few orders. Fortunately, Donald Amos recently published a package of higher transcendental function subroutines which give incredibly accurate and fast results without recursion [39]. Instead, it uses a number of series approximations, in appropriate ranges of the argument, with system hardware dependent coefficients to maximize the available precision. This package will compute  $J_n$  and  $N_n$  for positive  $n$  and complex arguments in addition to other special functions.

The computation of these Bessel functions and their derivatives is carried out in subroutine TOTBES. Evaluation of the determinant of the filled matrix is the last operation performed in subroutine MTRXVAL. Here, as discussed earlier in Chapter 3, LU decomposition is used through subroutines DET1 and LUDCMP. It is the value of the determinant which is returned to the main program. Once the determinant becomes small enough, as directed by the root finder, signalling the location of a root, the last section of the main body of MDCW computes the transverse fields and the scalar potentials as a function of the waveguide diameter for this  $k_z$  root.

program mdcw10

```

*
*
*
*****
*
* Program -- Multiple Dielectric Circular Waveguide (mdcw)
*
* Written by Keith W. Whites
*
* This version 10 dated March 16, 1988
*
* This program will calculate the axial wavenumber for a circular waveguide
* containing q concentric dielectrics having complex constitutive parameters.
* Data needed by the program for these calculations are frequency, number of
* dielectrics, number of azimuthal variations, and the constitutive
* parameters of the dielectrics and their dimensions. The numerical root
* finding technique used is Muller's method which configures three points for
* a quadratic fit and uses a root of that quadratic fit to move towards
* the zero of the expression to be evaluated - in this case the det[A].
*
*
* Output Files: fldmag.wvd - transverse E and H fields (magnitudes, phases,
*                      real and imaginary parts) as a function of
*                      the guide radius.
*                      psie(m).wvd - scalar electric and magnetic potentials as a
*                      function of guide radius.
*                      pwrin.wvd - input file for "pwrflw3" code which calculates
*                      the total transverse, % distribution of real,
*                      and 3-D plot of power flow.
*                      zkHztra.wvd - trace of kz (axial wavenumber) in complex
*                      plane as the root finder searches for the
*                      correct root.
*
*
* Variables:  arg - argument of the Bessel functions
*             besj1 - Bessel function of the first kind (J) of the
*                   inner dielectric of the two under evaluation
*             besj2 - J of the outer dielectric
*             besn1 - Bessel function of the second kind (N) of the
*                   inner dielectric of the two under evaluation
*             besn2 - N of the outer dielectric
*             bes**p1 - Bessel function of order plus one
*             coeff - coefficients [C] for the field expansions
*             dbes** - derivative of the Bessel function '**'
*             dc - array of matrix elements for which kz is to be
*                 determined from
*             freq - radian frequency
*             ipart - number of divisions the radius is divided into for
*                   the field and scalar wave functions plots
*             ix1 - matrix row pointer
*             ix2 - matrix column pointer
*             nord - order of mode, number of azimuthal variations
*             numdi - number of dielectrics

```

```

*      psie(m) - scalar electric and magnetic potential functions
*      radii - radius of dielectrics and the conductor (m)
*      sacc - accuracy sought for kz value
*      ump1,ump2,ump3 - determinant values for three guesses
*                      to be used with Muller's method
*      uma,umb,umc - updating information for Muller's method
*      zeps - permittivity
*      zkro - radial wavenumber
*      zkz - axial wavenumber
*      zmu - permeability
*
* Subroutines:  det1 - calculates the determinant of a double precision
*                complex matrix using lu decomposition
*                lubksb - called by det1 to perform the backsubstitution
*                       after the LU decomposition in order to calculate
*                       the coefficients [C]
*                mtrxval - calculates the elements of the matrix from
*                       the boundary conditions for the multiple
*                       concentric dielectric circular waveguide
*                totbes - calculates the Bessel functions and their
*                       derivatives for both dielectrics bordering
*                       an interface
*                zbesj(y) - called by totbes to calculate the Bessel
*                       functions of the first and second kinds with
*                       complex arguments
*
*****
*
*
*      implicit complex*16(a-h,o-r,t-z)
*      implicit real*8(s)
*      parameter (pi=(3.14159265359d0,0.0d0),maxdie=5,maxcon=maxdie*4-2)
*      parameter (zeps0=(8.854d-12,0.0d0),zmu0=(12.56637062d-7,0.0d0))
*      parameter (ipart=100,ibesnum=maxdie)
*      complex*16 zkro(maxdie),radii(maxdie),zmu(maxdie),
+      zeps(maxdie),dc(maxcon,maxcon),coeff(maxcon),
+      efra(ipart),efphi(ipart),hfra(ipart),hfphi(ipart),
+      psie(ipart),psieder(ipart),psim(ipart),psimder(ipart)
*      complex*16 worksp(maxcon),indx(maxcon)
*      real*8 sjunk1(ibesnum),sjunk2(ibesnum)
*      real*8 sbjr(ibesnum),sbji(ibesnum),sbyr(ibesnum),sbyi(ibesnum)
*      integer*4 ipivot(maxcon)
*      common/combes/nord,zkro,radii
*      common/mtrx/freq,zmu,zeps,numdi,sacc,dc
*
*      open(unit=11,file='a:zkztra.wvd',status='unknown')
*      open(unit=23,file='a:fldmag.wvd',status='unknown')
*      open(unit=26,file='a:pwrin.wvd',status='unknown')
*      open(unit=29,file='a:psie.wvd',status='unknown')
*      open(unit=31,file='a:psim.wvd',status='unknown')

```

:set up  
:output files

```

itcont=0
mstp=0
iflagd=1
sguinc=0.0d0
write(*,*) 'enter frequency(Hz) and the number of dielectrics'
read(*,*) sfreq,numdi
freq=dcmplx(sfreq)*(2.0d0,0.0d0)*pi
write(*,*) 'enter order'
read(*,*) nord
write(*,*) 'enter 3 kz guesses'
write(*,*) ' (middle guess,largest,smallest:recommended)'
read(*,*) zkz1
szkzre=dreal(zkz1)
szkzim=dimag(zkz1)
write(11,12) szkzre,szkzim
read(*,*) zkz2
szkzre=dreal(zkz2)
szkzim=dimag(zkz2)
write(11,12) szkzre,szkzim
read(*,*) zkz3
szkzre=dreal(zkz3)
szkzim=dimag(zkz3)
write(11,12) szkzre,szkzim
write(*,*) 'desired accuracy?'
read(*,*) sacc
*
do 10 i=1,numdi
  write(*,*) 'enter radius, mu, and epsilon'
  read(*,*) sradii,zmu(i),zeps(i)
  radii(i)=dcmplx(sradii)
  zmu(i)=zmu(i)*zmu0
  zeps(i)=zeps(i)*zeps0
10 continue
*
write(*,*) 'Calculate Field Magnitudes? (1/0)'
read(*,*) magcal
*
* with 3 kz guesses, call subroutine mtrxval to calculate matrix elements
* and the value of the resulting determinant
*
call mtrxval(zkz1,det,iflagd)
ump1=det
call mtrxval(zkz2,det,iflagd)
ump2=det
call mtrxval(zkz3,det,iflagd)
ump3=det
*
* the 100 goto loop utilizes Muller's method to determine the kz value
*
100 itcont=itcont+1
umq=(zkz1-zkz2)/(zkz2-zkz3)
uma=umq*ump1-umq*((1.0d0,0.0d0)+umq)*ump2+umq*umq*ump3
umb=((2.0d0,0.0d0)*umq+(1.0d0,0.0d0))*ump1-((1.0d0,0.0d0)+umq)
+ *((1.0d0,0.0d0)+umq)*ump2+umq*umq*ump3

```

```

    umc=((1.0d0,0.0d0)+umq)*ump1
*
    uradi=sqrt(umb*umb-(4.0d0,0.0d0)*uma*umc)
*
    if (abs(umb+uradi).gt.abs(umb-uradi)) then
        uradi=umb+uradi
    else
        uradi=umb-uradi
    endif
*
    ump3=ump2
    ump2=ump1
    zkz3=zkz2
    zkz2=zkz1
*
* calculate a new point and update last two points for quadratic fit
*
    zkz1=zkz2-(zkz2-zkz3)*(2.0d0,0.0d0)*umc/uradi
    szkzre=dreal(zkz1)
    szkzim=dimag(zkz1)
    write(11,12) szkzre, szkzim
    call mtrxval(zkz1,det,iflagd)
    ump1=det
*
* if kz varies less than the specified value, then end
*
    if ((cdabs(zkz1-zkz2).lt.sacc)) then
*
        write(*,*) 'finished'
        write(*,*) 'kz=',zkz1
        write(*,*) 'total number of iterations = ',itcont
        write(*,*) 'determinant of matrix = ',det
*
        do 200 i=1,numdi
            if(abs(zkro(i)).lt.1.0d0) then
                write(*,*) 'potential error : zkro small'
                write(*,*) 'zkro('i,')=',zkro(i)
            endif
            write(*,*) 'zkro('i,')=',zkro(i)
200    continue
*
        write(*,*) 'finished'
        mstp=1
    endif
*
    if(mstp)100,100,300
*
300    continue
*
    if(magcal)999,999,305
*
305    continue
*
    maxnum=4*numdi-2

```

```

      call mtrxval(zkz1,det,0)
*
      do 310 i=1,(maxnum-1)
        coeff(i)=-dc(i+1,1)
310    continue
*
      do 315 i=1,maxnum
        do 317 j=1,maxnum
          dc(i,j)=dc(i+1,j+1)
317    continue
315  continue
*
* calculate field expansion coefficients
*
      call ludcmp(dc,maxnum-1,maxcon,indx,d)
      call lubksb(dc,maxnum-1,maxcon,indx,coeff)
      write(*,*) 'the coefficients are:'
*
      do 320 i=maxnum,2,-1
        coeff(i)=coeff(i-1)
        write(*,*) 'coeff(',i,')',coeff(i)
320  continue
*
      coeff(1)=(1.0d0,0.0d0)
      write(*,*) 'coeff(1)',coeff(1)
      guidsp=radii(numdi)/dcmplx(ipart)
*
* calculate transverse E and H fields knowing the kz and coefficients
*
      do 400 j=1,ipart
        sguinc=sguinc+dreal(guidsp)
*
        if(sguinc.lt.dreal(radii(1))) then
          arg=zkro(1)*dcmplx(sguinc)
*
          call zbesj(dreal(arg),dimag(arg),dble(nord),1,2,sbjr,sbji,
+            nz,ierr)
          if(ierr.ne.0) write(*,*) 'Bessel Routine error #',ierr
          call zbesy(dreal(arg),dimag(arg),dble(nord),1,2,sbyr,sbyi,
+            nz,sjunk1,sjunk2,ierr)
          if(ierr.ne.0) write(*,*) 'Bessel Routine error #',ierr
          bj=dcmplx(sbjr(1))+(0.0d0,1.0d0)*dcmplx(sbji(1))
          bjp1=dcmplx(sbjr(2))+(0.0d0,1.0d0)*dcmplx(sbji(2))
          dbj=dcmplx(nord)*bj/arg-bjp1
*
          efra(j)=-zkz1/(freq*zeps(1))*coeff(1)*zkro(1)*dbj
+            -dcmplx(nord)/dcmplx(sguinc)*coeff(2)*bj
          hfra(j)=-zkz1/(freq*zmu(1))*coeff(2)*zkro(1)*dbj
+            -dcmplx(nord)/dcmplx(sguinc)*coeff(1)*bj
          efphi(j)=zkz1*dcmplx(nord)/(freq*zeps(1)*
+            dcmplx(sguinc))*coeff(1)*bj+zkro(1)*coeff(2)*dbj
          hfphi(j)=-zkz1*dcmplx(nord)/(freq*zmu(1)*
+            dcmplx(sguinc))*coeff(2)*bj-zkro(1)*coeff(1)*dbj
*

```

:shift matrix up  
:and to the left  
:one element

:arbitrarily define

```

psim(j)=coeff(1)*bj
psimder(j)=coeff(1)*dbj
psie(j)=coeff(2)*bj
psieder(j)=coeff(2)*dbj

```

```

:calculate electric
:and magnetic
:scalar potentials

```

```

else

```

```

*
do 410 i=2,numdi
*
    if(sguinc.ge.dreal(radii(i-1)).and.sguinc.le.
+      dreal(radii(i))) then
        irng=i
    endif
*
410 continue
*
    arg=zkro(irng)*dcmplx(sguinc)
*
    call zbesj(dreal(arg),dimag(arg),db1e(nord),1,2,sbjr,sbji,
+      nz,ierr)
    if(ierr.ne.0) write(*,*) 'Bessel Routine error #',ierr
    call zbesy(dreal(arg),dimag(arg),db1e(nord),1,2,sbyr,sbyi,
+      nz,sjunk1,sjunk2,ierr)
    if(ierr.ne.0) write(*,*) 'Bessel Routine error #',ierr
    oj=dcmplx(sbjr(1))+(0.0d0,1.0d0)*dcmplx(sbji(1))
    by=dcmplx(sbyr(1))+(0.0d0,1.0d0)*dcmplx(sbyi(1))
    bjp1=dcmplx(sbjr(2))+(0.0d0,1.0d0)*dcmplx(sbji(2))
    byp1=dcmplx(sbyr(2))+(0.0d0,1.0d0)*dcmplx(sbyi(2))
    dbj=dcmplx(nord)*bj/arg-bjp1
    dby=dcmplx(nord)*by/arg-byp1
*
    ii=4*irng-5
    efra(j)=-zkz1/(freq*zeps(irng))*(coeff(ii)*
+      zkro(irng)*dbj+coeff(ii+1)*zkro(irng)*dby)
    efra(j)=efra(j)-dcmplx(nord)/dcmplx(sguinc)*(coeff(ii+2)*
+      bj+coeff(ii+3)*by)
    hfra(j)=-zkz1/(freq*zmu(irng))*(coeff(ii+2)*
+      zkro(irng)*dbj+coeff(ii+3)*zkro(irng)*dby)
    hfra(j)=hfra(j)-dcmplx(nord)/dcmplx(sguinc)*(coeff(ii)*
+      bj+coeff(ii+1)*by)
    efphi(j)=zkz1*dcmplx(nord)/(freq*zeps(irng)*
+      dcmplx(sguinc))*(coeff(ii)*bj+coeff(ii+1)*by)
    efphi(j)=efphi(j)+zkro(irng)*(coeff(ii+2)*dbj+
+      coeff(ii+3)*dby)
    hfphi(j)=-zkz1*dcmplx(nord)/(freq*zmu(irng)*
+      dcmplx(sguinc))*(coeff(ii+2)*bj+coeff(ii+3)*by)
    hfphi(j)=hfphi(j)-zkro(irng)*(coeff(ii)*dbj+
+      coeff(ii+1)*dby)
*
    psim(j)=coeff(ii)*bj+coeff(ii+1)*by
    psimder(j)=coeff(ii)*dbj+coeff(ii+1)*dby
    psie(j)=coeff(ii+2)*bj+coeff(ii+3)*by
    psieder(j)=coeff(ii+2)*dbj+coeff(ii+3)*dby
endif

```

```

*
400 continue
*
    sfdmax=0.0d0
*
* write out the E and H fields
*
    do 420 i=1,ipart
        sfdmax=max(abs(efra(i)),abs(hfra(i)),abs(efphi(i)),
+               abs(hfphi(i)),sfdmax)
420 continue
*
    sguinc=0.0d0
    write(23,*) ' radius      E ro (mag)    H ro (mag)    E phi
+ (mag)    H phi (mag)'
*
    do 430 i=1,ipart
        sguinc=sguinc+dreal(guidsp)
        write(23,24) sguinc,abs(efra(i))/sfdmax,abs(hfra(i))/sfdmax,
+               abs(efphi(i))/sfdmax,abs(hfphi(i))/sfdmax
430 continue
*
    sguinc=0.0d0
    write(23,*) ' radius      E rc (real)    H ro (real)    E phi
+ (real)    H phi(real)'
*
    do 431 i=1,ipart
        sguinc=sguinc+dreal(guidsp)
        write(23,24) sguinc,dreal(efra(i))/sfdmax,dreal(hfra(i))/
+               sfdmax,dreal(efphi(i))/sfdmax,dreal(hfphi(i))/
+               sfdmax
431 continue
*
    sguinc=0.0d0
    write(23,*) ' radius      E ro (imag)    H ro (imag)    E phi
+ (imag)    H phi(imag)'
*
    do 432 i=1,ipart
        sguinc=sguinc+dreal(guidsp)
        write(23,24) sguinc,dimag(efra(i))/sfdmax,dimag(hfra(i))/
+               sfdmax,dimag(efphi(i))/sfdmax,dimag(hfphi(i))/
+               sfdmax
432 continue
*
    write(26,27) dreal(zkz1),dimag(zkz1),sfreq,nord,numdi
*
    do 440 i=1,numdi
        write(26,28) dreal(zeps(i)/zeps0),dreal(zmu(i)/zmu0),
+               dreal(radii(i))
        write(26,28) dimag(zeps(i)/zeps0),dimag(zmu(i)/zmu0)
440 continue
*
    do 450 i=1,maxnum
        write(26,28) dreal(coeff(i)),dimag(coeff(i))

```



```

450  continue
*
*      sguinc=0.0d0
*
* write out the electric and magnetic scalar potentials
*
*      do 460 i=1,ipart
*
*          sguinc=sguinc+dreal(guidsp)
*          write(29,24) sguinc,dreal(psie(i)),dimag(psie(i)),
+              dreal(psieder(i)),dimag(psieder(i))
*          write(31,24) sguinc,dreal(psim(i)),dimag(psim(i)),
+              dreal(psimder(i)),dimag(psimder(i))
*
460  continue
*
12   format(e12.5,5x,e12.5)
24   format(e12.5,4x,e12.5,4x,e12.5,4x,e12.5,4x,e12.5)
27   format(e12.5,5x,e12.5,5x,e12.5,5x,i4,5x,i4)
28   format(e12.5,5x,e12.5,5x,e12.5)
999  close(31)
      close(29)
      close(26)
      close(23)
      close(11)
      end
*
*
*
*-----
*
* Subroutine mtrxval
*
* mtrxval calculates the matrix elements for the multiple dielectric
* circular waveguide main program.
*
* input: zkz - axial wavenumber guess
*        iflag - = 1 for determinant calculation
*               = 0 for no determinant
*
* output: det - determinant of matrix for kz guess
*
*-----
*
*
*
*      subroutine mtrxval(zkz,det,iflagd)
*      implicit complex*16(a-h,o-r,t-z)
*      implicit real*8(s)
*      parameter (spi=3.14159265359,maxdie=5,maxcon=maxdie*4-2)
*      parameter (zeps0=(8.854d-12,0.0d0),zmu0=(12.56637062d-7,0.0d0))
*      parameter (ibesnum=4)
*      complex*16 zkro(maxdie),radii(maxdie),zmu(maxdie),
+          zeps(maxdie),dc(maxcon,maxcon)

```

```

complex*16 worksp(maxcon)
real*8 sjunk1(ibesnum),sjunk2(ibesnum)
real*8 sbjr(ibesnum),sbji(ibesnum),sbyr(ibesnum),sbyi(ibesnum)
integer*4 ipivot(maxcon)
common/combes/nord,zkro,radii
common/mtrx/freq,zmu,zeps,numdi,sacc,dc
*
do 1020 i=1,maxcon
  do 1030 j=1,maxcon
    dc(i,j)=(0.0d0,0.0d0)
1030   continue
1020   continue
*
zkro(1)=sqrt(freq*freq*zmu(1)*zeps(1)-zkz*zkz)
ix1=1
ix2=1
*
do 1000 i=2,numdi
  zkro(i)=sqrt(freq*freq*zmu(i)*zeps(i)-zkz*zkz)           :principal value
  arg=zkro(i)*radii(i-1)
*
* for the given zkz, the Bessel's functions and their derivatives are found
*
  call totbes(i,arg,besj1,besj2,besn1,besn2,dbesj1,dbesj2,
+      dbesn1,dbesn2)
*
* calculate matrix elements. inner dielectric is a special case and is source
* of the if statements. ix1-row pointer, ix2-column pointer, i=outer dielectric
* of the two under observation.
*
  dc(ix1,ix2)=zkro(i-1)*zkro(i-1)*zeps(i)*besj1
*
  if(ix1.ne.1) then
    dc(ix1,ix2+1)=zkro(i-1)*zkro(i-1)*zeps(i)*besn1
    ix2=ix2+2
  endif
*
  dc(ix1,ix2+2)=-zkro(i)*zkro(i)*zeps(i-1)*besj2
  dc(ix1,ix2+3)=-zkro(i)*zkro(i)*zeps(i-1)*besn2
  ix1=ix1+1
*
  if(ix1.ne.2) then
    ix2=ix2-2
    dc(ix1,ix2+2)=zkro(i-1)*zkro(i-1)*zmu(i)*besj1
    dc(ix1,ix2+3)=zkro(i-1)*zkro(i-1)*zmu(i)*besn1
    dc(ix1,ix2+6)=-zkro(i)*zkro(i)*zmu(i-1)*besj2
    dc(ix1,ix2+7)=-zkro(i)*zkro(i)*zmu(i-1)*besn2
  else
    dc(ix1,ix2+1)=zkro(i-1)*zkro(i-1)*zmu(i)*besj1
    dc(ix1,ix2+4)=-zkro(i)*zkro(i)*zmu(i-1)*besj2
    dc(ix1,ix2+5)=-zkro(i)*zkro(i)*zmu(i-1)*besn2
  endif
*
  ix1=ix1+1

```

```

      +      dc(ix1,ix2)=zkz*dcmplx(nord)/(freq*zeps(i-1)*radii(i-1))*
      +      besj1
*
      if(ix1.eq.3) then
        ix2=ix2-1
      else
        +      dc(ix1,ix2+1)=zkz*dcmplx(nord)/(freq*zeps(i-1)
        +      *radii(i-1))*besn1
      endif
*
      dc(ix1,ix2+2)=zkro(i-1)*dbesj1
*
      if(ix1.eq.3) then
        ix2=ix2-1
      else
        dc(ix1,ix2+3)=zkro(i-1)*dbesn1
      endif
*
      dc(ix1,ix2+4)=-zkz*dcmplx(nord)/(freq*zeps(i)*radii(i-1))*
      +      besj2
      dc(ix1,ix2+5)=-zkz*dcmplx(nord)/(freq*zeps(i)*radii(i-1))*
      +      besn2
      dc(ix1,ix2+6)=-zkro(i)*dbesj2
      dc(ix1,ix2+7)=-zkro(i)*dbesn2
*
      if(ix1.eq.3) then
        ix2=ix2+2
      endif
*
      ix1=ix1+1
      dc(ix1,ix2)=zkro(i-1)*dbesj1
*
      if(ix1.eq.4) then
        ix2=ix2-1
      else
        dc(ix1,ix2+1)=zkro(i-1)*dbesn1
      endif
*
      dc(ix1,ix2+2)=zkz*dcmplx(nord)/(freq*zmu(i-1)*radii(i-1))*
      +      besj1
*
      if(ix1.eq.4) then
        ix2=ix2-1
      else
        dc(ix1,ix2+3)=zkz*dcmplx(nord)/(freq*zmu(i-1)
        +      *radii(i-1))*besn1
      endif
*
      dc(ix1,ix2+4)=-zkro(i)*dbesj2
      dc(ix1,ix2+5)=-zkro(i)*dbesn2
      dc(ix1,ix2+6)=-zkz*dcmplx(nord)/(freq*zmu(i)*radii(i-1))*
      +      besj2
      dc(ix1,ix2+7)=-zkz*dcmplx(nord)/(freq*zmu(i)*radii(i-1))*
      +      besn2

```

```

*
      if (ix1.eq.4) then
        ix2=ix2+2
      endif
*
      ix1=ix1+1
*
      if(ix1.eq.5) then
        ix2=ix2+2
      else
        ix2=ix2+4
      endif
*
1000  continue
*
      arg=zkro(numdi)*radii(numdi)
*
* for last two rows calculate elements. zbesj(y) is Bessel's routine with no
* derivatives. last two rows due to PEC guiding structure.
*
      call zbesj(dreal(arg),dimag(arg),dble(nord),1,2,sbjr,sbji,
+         nz,ierr)
      if(ierr.ne.0) write(*,*) 'Bessel Routine error #',ierr
      call zbesy(dreal(arg),dimag(arg),dble(nord),1,2,sbyr,sbyi,
+         nz,sjunk1,sjunk2,ierr)
      if(ierr.ne.0) write(*,*) 'Bessel Routine error #',ierr
      besj2=dcmplx(sbjr(1))+(0.0d0,1.0d0)*dcmplx(sbji(1))
      besn2=dcmplx(sbyr(1))+(0.0d0,1.0d0)*dcmplx(sbyi(1))
      besj2p1=dcmplx(sbjr(2))+(0.0d0,1.0d0)*dcmplx(sbji(2))
      besn2p1=dcmplx(sbyr(2))+(0.0d0,1.0d0)*dcmplx(sbyi(2))
      dbesj2=dcmplx(nord)*besj2/arg-besj2p1
      dbesn2=dcmplx(nord)*besn2/arg-besn2p1
      maxnum=numdi*4-2
      dc(ix1,maxnum-3)=besj2
      dc(ix1,maxnum-2)=besn2
      ix1=ix1+1
      dc(ix1,maxnum-1)=dbesj2
      dc(ix1,maxnum)=dbesn2
      nc=numdi*4-2
*
* with matrix calculated, now call determinant routine.
*
      if (iflagd) 2020,2020,2030
*
2030  continue
*
      call det1(dc,nc,det)
*
2020  continue
      return
      end

```

```

*
*
*
*-----
* Subroutine totbes
*
* totbes calculates the Bessel functions of the first and second kinds
* and the corresponding derivatives for complex arguments.
*
*
* input: i - loop counter (outer dielectric of the two under scrutiny)
*        arg - argument of Bessel functions
*
* output: besj1,besj2 - Bessel functions of the first kind
*           1-inner dielectric of the boundary
*           2-outer dielectric of the boundary
*        besn1,besn2 - Bessel functions of the second kind
*        dbesj1,dbesj2 - derivative of the Bessel function of the
*           first kind
*        dbesn1,dbesn2 - derivative of the Bessel function of the
*           second kind
*-----
*
*
*
*      subroutine totbes(i,arg,besj1,besj2,besn1,besn2,dbesj1,
+      dbesj2,dbesn1,dbesn2)
*
*      implicit complex*16(a-h,o-r,t-z)
*      implicit real*8(s)
*      parameter (pi=(3.14159265359d0,0.0d0),maxdie=5,maxcon=maxdie*4-2)
*      parameter (ibesnum=4)
*      complex*16 zkro(maxdie),radii(maxdie)
*      real*8 sjunk1(ibesnum),sjunk2(ibesnum)
*      real*8 sbjr(ibesnum),sbji(ibesnum),sbyr(ibesnum),sbyi(ibesnum)
*      common/combes/nord,zkro,radii
*
* with the argument and the order, call the Bessel function subroutine
*
*      call zbesj(dreal(arg),dimag(arg),dble(nord),1,2,sbjr,sbji,
+      nz,ierr)
*      if(ierr.ne.0) write(*,*) 'Bessel Routine error #',ierr
*      call zbesy(dreal(arg),dimag(arg),dble(nord),1,2,sbyr,sbyi,
+      nz,sjunk1,sjunk2,ierr)
*      if(ierr.ne.0) write(*,*) 'Bessel Routine error #',ierr
*      besj2=dcmplx(sbjr(1))+(0.0d0,1.0d0)*dcmplx(sbji(1))
*      besn2=dcmplx(sbyr(1))+(0.0d0,1.0d0)*dcmplx(sbyi(1))
*      besj2p1=dcmplx(sbjr(2))+(0.0d0,1.0d0)*dcmplx(sbji(2))
*      besn2p1=dcmplx(sbyr(2))+(0.0d0,1.0d0)*dcmplx(sbyi(2))
*      dbesj2=dcmplx(nord)*besj2/arg-besj2p1
*      dbesn2=dcmplx(nord)*besn2/arg-besn2p1

```

```

*
* calculate Bessel functions and derivatives for the inner dielectric
* of the boundary under consideration
*
    arg=zkro(i-1)*radii(i-1)
*
    call zbesj(dreal(arg),dimag(arg),dble(nord),1,2,sbjr,sbji,
+       nz,ierr)
    if(ierr.ne.0) write(*,*) 'Bessel Routine error #',ierr
    call zbesy(dreal(arg),dimag(arg),dble(nord),1,2,sbyr,sbyi,
+       nz,sjunk1,sjunk2,ierr)
    if(ierr.ne.0) write(*,*) 'Bessel Routine error #',ierr
    besj1=dcmplx(sbjr(1))+(0.0d0,1.0d0)*dcmplx(sbji(1))
    besn1=dcmplx(sbyr(1))+(0.0d0,1.0d0)*dcmplx(sbyi(1))
    besj1p1=dcmplx(sbjr(2))+(0.0d0,1.0d0)*dcmplx(sbji(2))
    besn1p1=dcmplx(sbyr(2))+(0.0d0,1.0d0)*dcmplx(sbyi(2))
    dbesj1=dcmplx(nord)*besj1/arg-besj1p1
    dbesn1=dcmplx(nord)*besn1/arg-besn1p1
*
    return
    end
*
*
*
* -----
*
* Subroutine det1
*
* det1 calculates the determinant of a double precision complex
* matrix using lu decomposition. reference "Numerical Recipes."
*
* input: a - square matrix under evaluation
*        n - size of square matrix
*
* output: d - determinant (complex, double precision)
*
* -----
*
*
*
* subroutine det1(a,n,d)
* implicit complex*16(a-h,o-z)
* parameter(maxdie=5,maxcon=maxdie*4-2,np=maxcon)
* complex*16 a(np,np),indx(np)
* call ludcmp(a,n,np,indx,d)
*
* do 11 i=1,n
*     d=d*a(i,i)
11 continue
*
* return
* end

```

```

*
*
*
*-----
*
* Subroutine ludcmp
*
* ludcmp performs the LU decomposition of the matrix [dc] to be used in
* conjunction with the root-finding routine in searching for kz, or
* in conjunction with lubksb to calculate coefficients [C].
* reference "Numerical Recipes."
*
*
* input: a - square matrix under evaluation
*        n - size of square matrix
*        np - dimension of matrix
*
* output: indx - row permutations for partial pivoting
*         d - even or odd number of row interchanges
*-----
*
*
*
*      subroutine ludcmp(a,n,np,indx,d)
*      implicit complex*16(a-h,o-z)
*      parameter(nmax=100)
*      complex*16 a(np,np),indx(np),vv(nmax)
*      tiny=(1.0d-40,1.0d-40)
*      d=(1.0d0,0.0d0)
*
*      do 12 i=1,n
*          aamax=(0.0d0,0.0d0)
*
*          do 11 j=1,n
*              if (cdabs(a(i,j)).gt.cdabs(aamax)) aamax=abs(a(i,j))
11          continue
*
*          if (aamax.eq.0.) pause 'singular matrix'
*          vv(i)=(1.0d0,0.0d0)/aamax
12      continue
*
*      do 19 j=1,n
*
*          do 14 i=1,j-1
*              sum=a(i,j)
*
*              do 13 k=1,j-1
*                  sum=sum-a(i,k)*a(k,j)
13          continue
*
*          a(i,j)=sum
14      continue
*

```

```

      aamax=(0.0d0,0.0d0)
*
      do 16 i=j,n
        sum=a(i,j)
*
        do 15 k=1,j-1
          sum=sum-a(i,k)*a(k,j)
15      continue
*
        a(i,j)=sum
        dum=vv(i)*abs(sum)
        if(cdabs(dum).ge.cdabs(aamax)) then
          imax=i
          aamax=dum
        endif
16      continue
*
        if (j.ne.imax) then
*
          do 17 k=1,n
            dum=a(imax,k)
            a(imax,k)=a(j,k)
            a(j,k)=dum
17      continue
*
            d=-d
            vv(imax)=vv(j)
          endif
          indx(j)=imax
          if(a(j,j).eq.0.) a(j,j)=tiny
          if(j.ne.n) then
            dum=(1.0d0,0.0d0)/a(j,j)
*
            do 18 i=j+1,n
              a(i,j)=a(i,j)*dum
18      continue
*
            endif
19      continue
*
          return
          end
*
*
*
* -----
* Subroutine lubksb
*
* lubksb calculates the backsubstitution in conjunction with ludcmp
* to calculate the coefficients [C]. reference "Numerical Recipes."
*
*

```



```

* input: a - square matrix under evaluation
*        n - size of square matrix
*        np - dimension of matrix
*
* output: indx - row permutations for partial pivoting
*         b - right-hand side of the matrix equation Ax=b

```

---

```

*
*      subroutine lubksb(a,n,np,indx,b)
*      implicit complex*16(a-h,o-z)
*      complex*16 a(np,np),indx(np),b(np)
*      ii=0
*
*      do 600 i=1,n
*          ll=indx(i)
*          sum=b(ll)
*          b(ll)=b(i)
*
*          if (ii.ne.0) then
*
*              do 610 j=ii,i-1
*                  sum=sum-a(i,j)*b(j)
*610             continue
*
*          else if (sum.ne.0.) then
*              ii=i
*          endif
*
*          b(i)=sum
*
*600     continue
*
*      do 620 i=n,1,-1
*          sum=b(i)
*          if (i.lt.n) then
*
*              do 630 j=i+1,n
*                  sum=sum-a(i,j)*b(j)
*630             continue
*
*          endif
*          b(i)=sum/a(i,i)
*
*620     continue
*
*      return
*      end

```

## REFERENCES

- [1] L. Pincherle, "Electromagnetic waves in metal tubes filled longitudinally with two dielectrics," *Phys. Rev.*, vol. 66, pp. 118-130, Sept. 1944.
- [2] P. J. B. Clarricoats, "Propagation along unbounded and bounded dielectric rods," Parts 1 and 2, *Proc. Inst. Elec. Eng.*, Mon. 409E and 410E, pp. 170-186, Oct. 1960.
- [3] K. A. Zaki and A. E. Atia, "Modes in dielectric-loaded waveguides and resonators," *IEEE Trans. Microwave Theory Tech.*, vol. MTT-31, pp. 1039-1045, Dec. 1983.
- [4] K. A. Zaki and C. Chen, "Intensity and distribution of hybrid-mode fields in dielectric-loaded waveguide," *IEEE Trans. Microwave Theory Tech.*, vol. MTT-33, pp. 1442-1447, Dec. 1985.
- [5] K. A. Zaki and C. Chen, "Coupling of non-axially symmetric hybrid modes in dielectric resonators," *IEEE Trans. Microwave Theory Tech.*, vol. MTT-35, pp. 1136-1142, Dec. 1987.
- [6] W. M. Bruno and W. B. Bridges, "Flexible dielectric waveguides with powder cores," *IEEE Trans. Microwave Theory Tech.*, vol. MTT-36, pp. 882-890, May 1988.
- [7] R. C. Chou and S. W. Lee, "Modal attenuation in multilayered coated waveguides," *IEEE Trans. Microwave Theory Tech.*, vol. MTT-36, pp. 1167-1176, July 1988.
- [8] P. J. B. Clarricoats and R. A. Waldron, "Non-periodic slow-wave and backward-wave structures," *J. Electron. Contr.*, vol. 8, pp. 455-458, June 1960.
- [9] P. J. B. Clarricoats, "Backward waves in waveguides containing dielectric," *Proc. Inst. Elec. Eng.*, Mon. 451E, vol. 108C, pp. 496-501, June 1961.
- [10] P. J. B. Clarricoats, "Circular-waveguide backward-wave structures," *Proc. Inst. Elec. Eng.*, vol. 110, pp. 261-270, Feb. 1963.
- [11] P. J. B. Clarricoats and A. B. Birtles, "Circular waveguide backward-wave experiments," *J. Electron. Contr.*, vol. 15, pp. 325-330, Oct. 1963.
- [12] P. J. B. Clarricoats and K. R. Slinn, "Experimental observation of travelling backward waves in dielectric-loaded circular waveguide," *Proc. Inst. Elec. Eng.*, vol. 111, pp. 1090-1092, June 1964.
- [13] R. A. Waldron, "Theory and potential applications of backward waves in nonperiodic inhomogeneous waveguides," *Proc. Inst. Elec. Eng.*, vol. 111, pp. 1659-1667, Oct. 1964.

- [14] P. J. B. Clarricoats and B. C. Taylor, "Evanescent and propagating modes of dielectric-loaded circular waveguide," *Proc. Inst. Elec. Eng.*, vol. 111, pp. 1951-1956, Dec. 1964.
- [15] P. Chorney, "Power and energy relations in bidirectional waveguides," Tech. Rep. 396, Research Lab. of Electronics, Mass. Inst. Tech., Cambridge, MA, Sept. 1961.
- [16] S. R. Laxpati and R. Mittra, "Energy considerations in open and closed waveguides," *IEEE Trans. Antennas Propagat.*, vol. AP-13, pp. 883-890, Nov. 1965.
- [17] V. A. Kalmyk, S. B. Rayevskiy and V. P. Ygryumov, "An experimental verification of existence of complex waves in a two-layer, circular, shielded waveguide," *Radio Eng. Electron. Phys.*, vol. 23, pp. 17-19, Apr. 1978.
- [18] E. Snitzer, "Cylindrical dielectric waveguide modes," *J. Opt. Soc. Amer.*, vol. 51, pp. 491-498, May 1961.
- [19] R. A. Waldron, *Theory of Wave Guides and Cavities*. London: Maclaren and Sons Ltd., 1967.
- [20] S. Ramo, J. R. Whinnery and T. Van Duzer, *Fields and Waves in Communication Electronics*. New York: Wiley, 1984.
- [21] R. F. Harrington, *Time-Harmonic Electromagnetic Fields*. New York: McGraw-Hill, 1961.
- [22] A. R. von Hippel, *Dielectric Materials and Applications*. New York: Wiley, 1958.
- [23] E. J. Rothwell and L. L. Frasc, "Propagation characteristics of dielectric-rod-loaded waveguides," *IEEE Trans. Microwave Theory Tech.*, vol. MTT-36, pp. 594-600, Mar. 1988.
- [24] R. E. Beam, M. M. Astrahan, W. C. Jakes, H. M. Wachowski and W. L. Firestone, "Dielectric tube waveguides," Tech. Rep. ATI 94929, ch. 5, Northwestern University, Evanston, IL, 1949.
- [25] R. A. Waldron, *Theory of Guided Electromagnetic Waves*. London: Van Nostrand Reinhold Company, 1969.
- [26] W. H. Press, B. P. Flannery, S. A. Teukolsky and W. T. Vetterling, *Numerical Recipes*. Cambridge: Cambridge University Press, 1986.
- [27] R. L. Burden and J. D. Faires, *Numerical Analysis*. Boston: Prindle, Weber and Schmidt, 3rd ed., 1985.
- [28] C. S. Lee, S. W. Lee and S. L. Chuang, "Normal modes in an overmoded circular waveguide coated with a lossy material," *IEEE Trans. Microwave Theory Tech.*, vol. MTT-34, pp. 773-785, July 1986.
- [29] P. J. B. Clarricoats and K. R. Slinn, "Complex modes of propagation in dielectric-loaded circular waveguide," *Electron. Lett.*, vol. 1, pp. 145-146, July 1965.

- [30] A. S. Omar and K. F. Schunemann, "Complex and backward-wave modes in inhomogeneously and anisotropically filled waveguides," *IEEE Trans. Microwave Theory Tech.*, vol. MTT-35, pp. 268-275, Mar. 1987.
- [31] R. A. Waldron, "Properties of ferrite-loaded cylindrical waveguides in the neighbourhood of cut-off," *Proc. Inst. Elec. Eng.*, vol. 109B, suppl. 21, pp. 90-94, Jan. 1962.
- [32] E. C. Jordan, ed., *Reference Data for Engineers*. Indianapolis, IN: Howard W. Sams and Company, Inc., 1985.
- [33] D. G. Fink and D. Christiansen, eds., *Electronic Engineers' Handbook*. New York: McGraw-Hill, 1982.
- [34] *Information About Silicone Elastomers: Dow Corning 732 Multi-Purpose Sealant*. Midland, MI: Dow Corning Corporation, 1986.
- [35] P. F. Williams, K. F. Heyen and R. G. McCormack, "Low cost electromagnetic shielding using drywall composites: results of RFI testing of shielding effectiveness," Tech. Rep. No. M-88/02, US Army Corps of Engineers Construction Engineering Research Laboratory, Champaign, IL, Oct. 1987.
- [36] J. A. Kong, *Electromagnetic Wave Theory*. New York: John Wiley and Sons, Inc., 1986.
- [37] J. D. Jackson, *Classical Electrodynamics*. New York: John Wiley and Sons, Inc., 1975.
- [38] J. T. Verdeyen, *Laser Electronics*. Englewood Cliffs, NJ: Prentice-Hall, 1981.
- [39] D. E. Amos, "A portable package for bessel functions of a complex argument and nonnegative order," *ACM Trans. Math. Software*, vol. 12, pp. 265-273, Sept. 1986.

**DISTRIBUTION**

**HQUSACE**

ATTN: CEEC-E (2)  
ATTN: CERD-L  
ATTN: CEIM-SL (2)

USAEHSC, ATTN: Library 22060  
ATTN: DET III 79906

US Army Engineer Districts  
ATTN: Library (41)

US Army Engineer Division  
ATTN: Library (14)  
Huntsville 35807  
ATTN: Chief, HNDED-SR

USA Natick, R&D Ctr 01760

Naval Air Systems Command  
ATTN: Library

Federal Emergency Mgmt Agency  
ATTN: EMP Program Mgr 20472

Hanson AFB, MA 01731  
ATTN: HQ AFSC  
ATTN: ESD/OCR-E

Naval Civil Engr Lab  
ATTN: Library

Harry Diamond Labs 20783  
ATTN: SLCHD-NW  
ATTN: SLCHD-NW-E  
ATTN: SLCHD-NW-EP (10)  
ATTN: SLCHD-NW-EH  
ATTN: SLCHD-NW-ES  
ATTN: SLCHD-CS

Defense Nuclear Agency 20305  
ATTN: DNA-RAAE

Defense Technical Info. Center 22314  
ATTN: DDA (2)

U.S. Gov't Printing Office 22304  
Receiving Sect/Depository (2)